

# Measurement of Cross Sections and Asymmetries in Semi-Inclusive Deep Inelastic Scattering

Diplomarbeit  
vorgelegt  
von  
Daniel Matthiä

Fakultät für Mathematik und Physik  
Albert-Ludwigs-Universität  
Freiburg im Breisgau

Mai 2005



# Contents

<b>1</b>	<b>Introduction</b>	<b>5</b>
<b>2</b>	<b>Theoretical Motivation</b>	<b>7</b>
2.1	Deep Inelastic Scattering . . . . .	7
2.1.1	Unpolarised Inelastic Scattering . . . . .	8
2.1.2	Polarised Inelastic Scattering and Cross Section Asymmetries	10
2.2	The Parton Model of the Nucleon . . . . .	12
2.2.1	Semi-Inclusive Scattering . . . . .	14
2.3	Nucleon Spin Structure . . . . .	15
2.3.1	Measurement of $\frac{\Delta G}{G}$ . . . . .	16
<b>3</b>	<b>The COMPASS Experiment</b>	<b>19</b>
3.1	General . . . . .	19
3.2	The Polarised Muon Beam . . . . .	21
3.3	The Polarised Target . . . . .	21
3.4	Spectrometer . . . . .	22
3.4.1	Spectrometer Magnets . . . . .	23
3.4.2	Tracking detectors . . . . .	23
3.4.3	Calorimetry . . . . .	24
3.4.4	RICH . . . . .	24
3.4.5	Muon filters . . . . .	25
3.5	Trigger System . . . . .	25
3.6	Data Acquisition System . . . . .	27
<b>4</b>	<b>Inclusive Cross Sections</b>	<b>29</b>
4.1	Experimental Determination of the Cross Section . . . . .	29
4.2	Event and Data Selection . . . . .	31
4.2.1	Data Selection . . . . .	32
4.2.2	Event Selection . . . . .	32
4.3	Monte Carlo . . . . .	36
4.3.1	The Monte Carlo Chain . . . . .	38

4.3.2	Real Data versus Monte Carlo . . . . .	39
4.3.3	Monte Carlo Cross Sections . . . . .	44
4.3.4	Efficiencies . . . . .	49
4.4	Measured Inclusive Cross Sections . . . . .	51
4.4.1	Beam Flux and Luminosity . . . . .	51
4.4.2	Results . . . . .	52
4.4.3	Trigger Dependent Analysis . . . . .	56
<b>5</b>	<b>Semi-Inclusive Single High-<math>p_t</math> Hadron Analysis</b>	<b>63</b>
5.1	Event and Data Selection . . . . .	63
5.1.1	Kinematic Cuts . . . . .	64
5.1.2	Hadron Selection . . . . .	65
5.1.3	Hadron Identification with the RICH . . . . .	68
5.2	Semi-Inclusive Monte Carlo . . . . .	71
5.3	Semi-Inclusive Cross Sections . . . . .	73
5.4	Asymmetries . . . . .	77
5.4.1	Determination of the Asymmetry . . . . .	77
5.4.2	Dilution factor . . . . .	83
5.4.3	Depolarisation Factor . . . . .	83
5.4.4	Target Polarisation . . . . .	85
5.4.5	Beam Polarisation . . . . .	85
5.4.6	Results . . . . .	87
<b>6</b>	<b>Summary</b>	<b>91</b>
	<b>List of Figures</b>	<b>92</b>
	<b>List of Tables</b>	<b>95</b>
<b>A</b>	<b>Inclusive Cross Section Additives</b>	<b>99</b>
A.1	Numerical Results for the Inclusive Cross Section . . . . .	99
A.2	Trigger Dependent Analysis . . . . .	106
<b>B</b>	<b>Semi-inclusive Cross Section Additives</b>	<b>115</b>
B.1	Data Monte Carlo Comparison for 2002 . . . . .	115
B.2	Numerical Results for the Semi-Inclusive Cross Section . . . . .	117
<b>C</b>	<b>Asymmetry Additives</b>	<b>121</b>
C.1	Asymmetries for the different Periods . . . . .	121
	<b>Bibliography</b>	<b>124</b>

# Chapter 1

## Introduction

The research presented in this thesis has been done at the COMPASS experiment located at CERN<sup>1</sup>. The COMPASS experiment has been set up in order to study the nucleon structure in deep inelastic muon nucleon scattering with a fixed target. Today, the polarised and unpolarised structure functions of the quarks in the nucleon are well known. In contrast, the gluon helicity distribution function  $\Delta G(x)$ , which may contribute to the nucleon spin as well remains largely unknown. The main goal of COMPASS is the first measurement of the polarised gluon distribution function with a good precision.

Up to now two different approaches have been followed at COMPASS to determine the gluon polarisation  $\Delta G(x)/G$  both being used to tag the photon-gluon-fusion process: The selection of events including including heavy mesons and pairs of hadrons with high transverse momentum (high- $p_t$ ) in the final state. In this thesis a third method is presented, where events with at least one high- $p_t$  hadron are used to select the underlying physical process.

The polarised gluon distribution function can be extracted from the double spin cross section asymmetries of the photon-gluon-fusion process. These asymmetries have been recently calculated in next-to-leading order for the single high- $p_t$  hadron production cross section. The comparison of the calculated cross sections and asymmetries with the experimental results can test theoretical models with different gluon polarisation. The determination of the cross section asymmetry for single high- $p_t$  hadron production using all 2002 and 2003 COMPASS data is shown in this thesis. As an additional test on the theoretical models a direct comparison of the cross sections for single high- $p_t$  hadron production is done.

A complete understanding of the experimental setup is fundamental to measure inclusive cross sections. They are well known and provide a good test for the results. First results for inclusive cross sections of deep inelastic muon nucleon scattering at

---

<sup>1</sup>Conseil Européen de la Recherche Nucleaire

COMPASS will be presented.

# Chapter 2

## Theoretical Motivation

### 2.1 Deep Inelastic Scattering

In order to learn something about the internal structure of nucleons, one can use deep inelastic scattering processes. In the deep inelastic lepton–nucleon scattering is in our case the scattering of anti-muons with four-momentum  $k^\mu$  off deuterons or protons with four-momentum  $P^\mu \stackrel{Lab}{=} (M_N, 0, 0, 0)$ . The lepton interacts with a quark inside the nucleon by exchanging a boson. A Feynman-like diagram of inelastic scattering is shown in Fig.2.1.

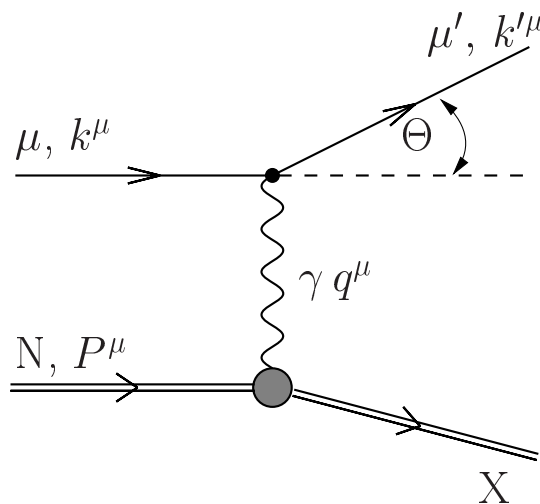


Figure 2.1: The Deep Inelastic Scattering(DIS) Graph

Table 2.1: Inclusive Variables in Deep Inelastic Scattering

Inclusive Variables	
Momentum of beam lepton	$k^\mu = (E, \vec{k})$
Momentum of scattered lepton	$k'^\mu = (E', \vec{k}')$
Momentum of target nucleon	$P^\mu = (E_P, \vec{P}) = (M_N, 0)$
Momentum transfer to the target	$q^\mu = (k^\mu - k'^\mu) = (\nu, \vec{q})$
neg. squared mom. transfer	$Q^2 = -q^2 = -q_\mu q^\mu \stackrel{Lab}{\approx} 4EE' \sin^2 \frac{\Theta}{2}$
Energy transfer to the target	$\nu = \frac{P_\mu q^\mu}{M} \stackrel{Lab}{=} E - E'$
Squared mass of final hadronic state	$W^2 = (P^\mu + q^\mu)^2 \stackrel{Lab.}{=} M^2 + 2M\nu - Q^2$
Bjorken Scaling Variables	
$x_{Bjorken}$	$x = \frac{Q^2}{2P_\mu q^\mu} \stackrel{Lab}{=} \frac{Q^2}{2M\nu}$
Fractional energy loss of the lepton	$y = \frac{P_\mu q^\mu}{P_\mu k^\mu} \stackrel{Lab}{=} \frac{\nu}{E}$

COMPASS has a polarised muon beam with a momentum of 160 GeV/c and a polarised fixed nucleon target. With the resulting centre-of-mass energy of 17.3 GeV one is well below the threshold for Z ( $m_Z = 92.6 \frac{GeV}{c^2}$ ) and W ( $m_{W^{+-}} = 81.8 \frac{GeV}{c^2}$ ) production and only electromagnetic interaction via a virtual photon  $\gamma$  with four-momentum  $q^\mu$  and energy  $\nu$  has to be considered.

By using the ‘‘Golden Rule’’ of scattering [3] one can calculate the cross section of the scattering process:

$$\frac{d\sigma}{dE'd\Omega} = \left(\frac{\alpha\hbar}{cq^2}\right)^2 \frac{E'}{E} L^{\mu\nu} W_{\mu\nu} \quad (2.1)$$

Here,  $\Omega$  is the solid angle of the lepton in the final state,  $\alpha$  is the fine structure constant and  $c$  the speed of light.

$L^{\mu\nu}$  describes the vertex of the photon emission by the lepton. In contrast to the hadron tensor, which depends on the internal structure of the nucleon, it can be calculated by quantum electrodynamic field theory for a point-like fermion. By making various assumptions for  $W^{\mu\nu}$  one can gain information about the nucleon structure.

### 2.1.1 Unpolarised Inelastic Scattering

In the inelastic scattering we have two independent scalars,  $Q^2 = -q^2$  and  $P^2$ . It is common not to use  $P^2$  as the independent variable, but the dimensionless and



lorentz-invariant  $x$ , introduced by J.D. Bjorken and therefore often called  $x_{Bjorken}$ .

$$x \equiv -\frac{q^\mu q_\mu}{2P^\mu q_\mu} \stackrel{Lab}{=} \frac{Q^2}{2M\nu} \quad (2.2)$$

Here,  $q^\mu$  is the momentum and  $\nu$  the energy transfer to the target.  $P^\mu$  is the momentum and  $M$  the mass of the target particle (see Tab. 2.1).

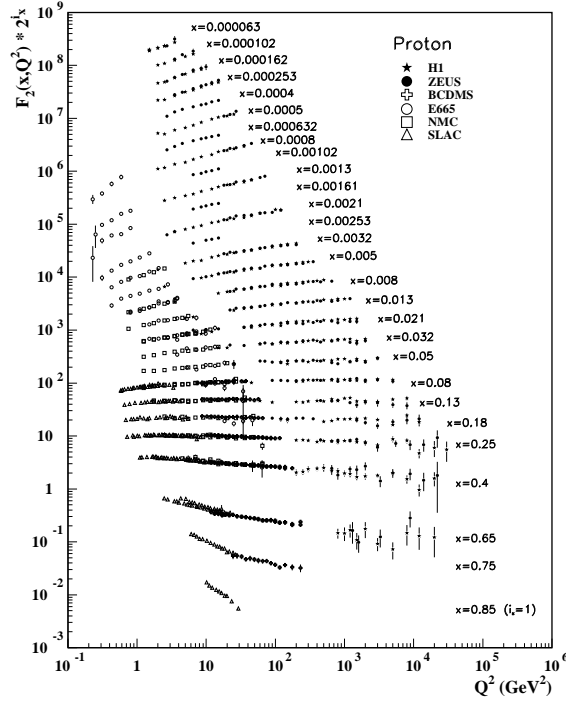


Figure 2.2:  $F_2(x, Q^2)$  of the proton from selected experiments from [6].  $F_2$  has been multiplied by  $2^{i_x}$ , where  $i_x$  is the number of the  $x$  bin, ranging from  $i_x = 1$  ( $x = 0.85$ ) to  $i_x = 28$  ( $x = 0.000063$ ).

The lepton tensor and the hadron tensor can be written as the sum of a symmetric and an antisymmetric part<sup>1</sup>.

$$L^{\mu\nu} = L_S^{\mu\nu} + iL_{AS}^{\mu\nu} \quad (2.3)$$

$$W^{\mu\nu} = W_S^{\mu\nu} + iW_{AS}^{\mu\nu} \quad (2.4)$$

The symmetric parts are independent of the lepton and nucleon spin. The asymmetric parts depend on the lepton or hadron spin respectively. By contracting the

<sup>1</sup>For the evaluation of the leptonic and hadronic tensors and the cross sections see [1]

tensors to  $L^{\mu\nu}W_{\mu\nu}$  and by calculating the sum of all outgoing states X, their momenta and spins and the average of the spins of the incoming particles, the unpolarised cross section can be calculated (see e.g. [4]). As  $E'$  is not a function of the incident lepton energy  $E$  and the scattering angle  $\theta$  as in elastic scattering, the cross section depends on  $E'$  and the solid angle  $\Omega$ . In the unpolarised case the hadron tensor  $W^{\mu\nu}$  can be reduced to two functions  $W_{1,2}$  which only depend on  $\nu$  and  $Q^2$ .

$$\frac{d\sigma}{dE'd\Omega} = \left( \frac{\alpha\hbar}{4ME\sin^2(\theta/2)} \right)^2 \frac{E'}{E} \left[ 2W_1(\nu, Q^2)\sin^2(\theta/2) + W_2(\nu, Q^2)\cos^2(\theta/2) \right] \quad (2.5)$$

Introducing the dimensionless magnitude  $x$ , and writing Eq. 2.5 in terms of  $x$  and  $Q^2$ , one obtains with the so-called nucleon structure functions  $F_{1,2}(x, Q^2)$ :

$$\frac{d\sigma}{dx dQ^2} = \frac{4\pi\alpha^2}{Q^4 x} \left[ xy^2 \left( 1 - \frac{2m^2}{Q^2} \right) F_1(x, Q^2) + \left( 1 - y - \frac{\gamma^2 y^2}{4} \right) F_2(x, Q^2) \right] \quad (2.6)$$

All unpolarised information about the nucleon structure is included in the structure functions  $F_{1,2}$ . They have been measured by various experiments and some results for  $F_2(x, Q^2)$  are shown in Fig. 2.2. In a medium range of  $x$ ,  $F_2(x, Q^2)$  obviously does not depend on  $Q^2$  anymore. This is called the Bjorken Scaling Behaviour and is an evidence of the point-like constituents of the nucleon, the quarks [8].

## 2.1.2 Polarised Inelastic Scattering and Cross Section Asymmetries

To investigate the spin-structure of the nucleon, which is the main goal of the COMPASS experiment, it is inevitable to study polarised scattering reactions.

As the antisymmetric part of  $W_{\mu\nu}$  does not vanish anymore, two polarised structure functions  $g_1(x, Q^2)$  and  $g_2(x, Q^2)$  have to be considered in the cross section. They complement the description of the internal nucleon structure.

The polarised cross section can be written as (see [1]):

$$\begin{aligned} \frac{d^2\sigma}{dx dy d\phi} &= \frac{e^4 ME}{4\pi Q^4} \left[ xy^2 F_1(x, Q^2) + (1 - y) F_2(x, Q^2) \right. \\ &\quad + y^2 g_1(x, Q^2) \left( 2x \frac{s_l \cdot s_h}{p \cdot q} + \frac{q \cdot s_l q \cdot s_h}{p \cdot q p \cdot q} \right) \\ &\quad \left. + 2xy^2 g_2(x, Q^2) \left( \frac{s_h \cdot s_l}{p \cdot q} - \frac{p \cdot s_l q \cdot s_h}{p \cdot q p \cdot q} \right) \right] \quad (2.7) \end{aligned}$$

where  $s_l$  and  $s_h$  are the spin vectors of the lepton and the hadron.

To gather information about the spin structure of the nucleon, i.e.  $g_1(x, Q^2)$  and

$g_2(x, Q^2)$ , one has to measure the double spin asymmetry  $A_{||}$ , which is defined as (see [9]):

$$A_{||} = \frac{d\sigma^{\uparrow\downarrow} - d\sigma^{\uparrow\uparrow}}{d\sigma^{\uparrow\downarrow} + d\sigma^{\uparrow\uparrow}} \quad (2.8)$$

$$= xy \frac{(2 - y - \frac{Mxy}{E})g_1(x, Q^2) - \frac{2Mx}{E}g_2(x, Q^2)}{(1 - y - \frac{Mxy}{2E})F_2(x, Q^2) + xy^2F_1(x, Q^2)} \quad (2.9)$$

Eq. 2.8 is the asymmetry for the case of longitudinally polarised lepton beam and longitudinally polarised target, where  $d\sigma^{\uparrow\uparrow}$  ( $d\sigma^{\uparrow\downarrow}$ ) is the scattering cross section with (anti-)parallel spin orientation of lepton and nucleon. The (de)nominator is given by

$$d\sigma^{\uparrow\downarrow} - d\sigma^{\uparrow\uparrow} = \frac{d^2\Delta\sigma}{dx dQ^2} \quad (2.10)$$

$$= \frac{4\pi\alpha^2}{ME x Q^2} \left[ \left( 2 - \frac{Q^2}{2ME x} - \frac{Q^2}{2E^2} \right) g_1(x, Q^2) - \frac{2Mx}{E} g_2(x, Q^2) \right]$$

$$d\sigma^{\uparrow\downarrow} + d\sigma^{\uparrow\uparrow} = \frac{d^2\sigma}{dx dQ^2} \quad (2.11)$$

$$= \frac{4\pi\alpha^2}{Q^4 x} \left[ \left( 1 - \frac{Q^2}{2ME x} - \frac{Q^2}{4E^2} \right) F_2(x, Q^2) + \frac{Q^4}{4M^2 E^2 x} F_1(x, Q^2) \right]$$

The DIS process can be divided into the emission of a virtual photon by the lepton and the consequent absorption by the nucleon.  $A_{||}$  can then be related to the virtual photon absorption cross sections  $A_1$  and  $A_2$  [9]:

$$A_1 = \frac{g_1 - \gamma^2 g_2}{F_1} \quad (2.12)$$

$$A_2 = \frac{\gamma(g_1 + g_2)}{F_1} \quad (2.13)$$

$$\Rightarrow \mathbf{A}_{||} = \mathbf{D}(\mathbf{A}_1 + \eta \mathbf{A}_2) \quad (2.14)$$

The kinematical factors  $\eta$  and  $\gamma$  are given by

$$\begin{aligned} \gamma &= \sqrt{\frac{2Mx}{Ey}} \\ \eta &= \frac{2\gamma(1 - y - \frac{1}{4}\gamma^2 y^2)}{(2 - y)(1 + \frac{1}{2}\gamma^2 y)} \end{aligned} \quad (2.15)$$

and  $D$  is the Depolarisation Factor, which expresses the spin transfer of the lepton to the virtual photon.

$$D = \frac{y(2-y)(1 + \frac{1}{2}\gamma^2 y)}{(1 + \gamma^2)[2(1-y - \frac{\gamma^2 y^2}{4})(\frac{1+R}{1+\gamma^2}) + y^2]} \quad (2.16)$$

$$R = \frac{\sigma_L}{\sigma_T} = \frac{1 + \gamma^2}{2xF_1(x, Q^2)} F_2(x, Q^2) - 1 \quad (2.17)$$

$R$  is the ratio of the longitudinal and the transversal cross section. In high energy scattering, where  $E \gg M$ ,  $\gamma$  becomes very small and hence the terms  $\propto \gamma^2$  can be neglected. One obtains

$$A_{\parallel} \approx D \cdot A_1 \approx D \cdot \frac{g_1}{F_1} \quad (2.18)$$

## 2.2 The Parton Model of the Nucleon

In the late sixties, Bjorken [8] suspected that in deep inelastic scattering the  $Q^2$  dependence of the structure functions would vanish and become only dependent on  $x$ :

$$\begin{aligned} F_1(x, Q^2) &\rightarrow F_1(x) \\ F_2(x, Q^2) &\rightarrow F_2(x) \end{aligned} \quad (2.19)$$

This is called the Bjorken scaling behaviour. This assumption was led by an earlier idea of Feynman who proposed a model of the nucleon in which the latter consists of smaller point-like particles called partons [7].

Furthermore, the structure functions  $F_1$  and  $F_2$  are not independent anymore. Callan and Gross found [10]:

$$F_1(x) = 2xF_2(x) \quad (2.20)$$

Actually, Eqs. 2.19 are a constitution of the fact that at high momentum transfers  $Q^2$ , the inelastic scattering on the nucleon becomes elastic scattering on the partons and the structure functions can be expressed as a sum of parton distribution functions (PDFs)  $f_i(x)$ .

$$F_2(x) = \frac{F_1(x)}{2x} = \sum_i e_i^2 x f_i(x) \quad (2.21)$$

The distribution functions  $f_i(x)$  can be interpreted as the probability to find a parton of type  $i$  with momentum fraction  $x$  of the parent nucleon and charge  $e_i$ . The sum

expands over all types of constituents.

In the same way, the polarised structure functions are composed by helicity parton distribution functions.

$$\begin{aligned} g_1(x) &= \frac{1}{2} \sum_i e_i^2 (f_i^+(x) - f_i^-(x)) = \frac{1}{2} \sum_i e_i^2 \Delta f(x) \\ g_2(x) &= 0 \end{aligned} \quad (2.22)$$

$f_i^+(x)(f_i^-(x))$  is the probability to find a parton of type  $i$  with momentum fraction  $x$  with the same (opposite) helicity as the parent nucleon. The unpolarised PDFs can be written as  $f_i(x) = f_i^+(x) + f_i^-(x)$ .

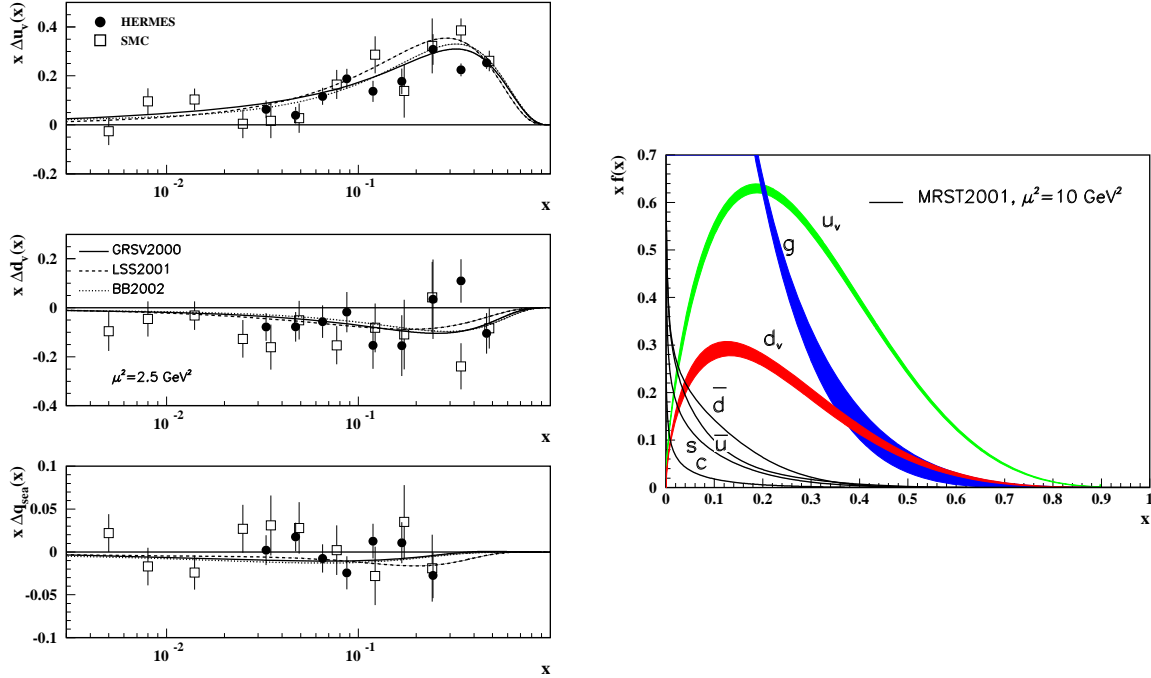


Figure 2.3: Polarised Parton Distribution Functions in different parametrisations (left) and Unpolarised Parton Distribution Functions in the MRST2001 parametrisations (right) from [6]

Currently the nucleon is pictured as consisting of the valence quarks, e.g. ( $u u d$ ) for the proton, the gluons ( $g$ ), which are continuously exchanged between the valence quarks, as they are the gauge bosons of the strong interaction, and the sea quarks ( $u(\bar{u})$ ,  $d(\bar{d})$ ,  $s(\bar{s})$ ) which evolve from pair creation of these gluons. To describe the structure of the nucleons all the polarised and unpolarised parton distribution

functions have to be known. Some experimental results are shown in Fig. 2.3 So far only charged particles contribute to the structure functions in Eq. 2.21 and 2.22, but experimental data reveals that only about 50% of the nucleons momentum is carried by the quarks and a QCD extension to the simple parton model had to be done.

Additionally for small values of  $x$ , the independence of the structure function of  $Q^2$  vanishes. This is called Scaling Violation. The virtual photon provides a higher resolution of the nucleon and shows additional content, namely the sea-quarks and the gluons.

### 2.2.1 Semi-Inclusive Scattering

In the deep inelastic scattering, the target nucleon typically breaks up and the struck quark and the target fragments into hadrons. New variables are necessary to describe the hadron kinematics (see Tab. 2.2). The Feynman scaling variable  $x_f$  and  $z$  can be used to distinguish between hadrons from the current fragmentation, i.e. hadrons which contain the struck parton, and from the target fragmentation, where the hadrons originate in the target remains. Particles in the current fragmentation typically have larger values of  $x_f$  and  $z$ .

Table 2.2: DIS Semi Inclusive Variables

Semi-inclusive Variables	
Longitudinal momentum of the hadron	$P_{  }^* = \vec{P}_h^* \cdot \frac{\vec{q}^*}{ q^* }$
Feynman scaling variable	$x_f = \frac{P_{  }^*}{ q^* } \approx \frac{2P_{  }^*}{W}$
Fraction of the $\gamma$ energy carried by h	$z = \frac{P_\mu P_h^\mu}{P_\mu q^\mu} \stackrel{Lab}{\approx} \frac{E_{had}}{\nu}$

The process of the fragmentation of the quarks to hadrons is described by the fragmentation functions  $D_q^h(z)$  and  $D_{\bar{q}}^h(z)$ . They are defined as the probability that a quark  $q$  or a anti-quark  $\bar{q}$  fragments into a hadron of type  $h$  with momentum fraction  $z$ . For the cross section of semi-inclusive hadron production one can write:

$$\frac{d^3\sigma_h}{dx dQ^2 dz} \propto \sum_q e_q^2 f(x, Q^2) D_q^h(z) \quad (2.23)$$

The longitudinal hadron production cross section asymmetry can then be defined as:

$$A_{||}^{lN \rightarrow hX} = \frac{d\sigma_h^{\uparrow\downarrow} - d\sigma_h^{\uparrow\uparrow}}{d\sigma_h^{\uparrow\downarrow} + d\sigma_h^{\uparrow\uparrow}} \quad (2.24)$$

Here,  $d\sigma_h^{\uparrow\uparrow}$  ( $d\sigma_h^{\uparrow\downarrow}$ ) are the cross sections for semi-inclusive hadron production, where the spin of the incident lepton is (anti-)aligned with the nucleon spin.

From Eq. 2.23 and Eq. 2.24 it is clear that knowledge about the semi-inclusive cross sections yields information about the cross section asymmetries and therefore about the internal spin of the nucleon.

Additionally, the comparison of measured cross sections with theoretical calculations can test our knowledge of the structure of the nucleon, i.e. the parton distribution functions and the fragmentation functions, which are crucial for an accurate description of deep inelastic scattering processes.

## 2.3 Nucleon Spin Structure

It is known that the spin of the nucleons is  $\frac{1}{2}$  in units of  $\hbar$ . To learn something about the composition of the nucleon spin, one can look at the first moment  $\Gamma_1$  of the spin structure function  $g_1(x)$ , which is defined as:

$$\Gamma_1 = \int_0^1 dx g_1(x) \quad (2.25)$$

The fraction of the nucleon spin, carried by the quarks of flavour  $i$ , is defined as the integral of the polarised parton distribution functions,

$$\Delta q_i = \int_0^1 dx [f_i^+(x) - f_i^-(x) + \bar{f}_i^+(x) - \bar{f}_i^-(x)] \quad (2.26)$$

one can calculate the first moment of  $g_1(x)$  with Eq. 2.22 for the proton and the neutron under the assumption that they contain u, d and s quarks.

$$\Gamma_1^p = \frac{1}{2} \left( \frac{4}{9} \Delta u + \frac{1}{9} \Delta d + \frac{1}{9} \Delta s \right) \quad (2.27)$$

$$\Gamma_1^n = \frac{1}{2} \left( \frac{1}{9} \Delta u + \frac{4}{9} \Delta d + \frac{1}{9} \Delta s \right) \quad (2.28)$$

The first moments can be expressed as functions of the  $\beta$  decay constant  $g_a$  and the  $SU(3)$  couplings  $\mathcal{F}$  and  $\mathcal{D}$ . The first moment of the proton is:

$$\Gamma_1^p = \frac{g_a}{12} \left( \frac{1}{3} \cdot \frac{3(\mathcal{F}/\mathcal{D}) - 1}{3(\mathcal{F}/\mathcal{D}) + 1} + 1 \right) + \frac{1}{9} \Sigma \quad (2.29)$$

$$(2.30)$$

with

$$\Sigma = \sum_{u,d,s} \Delta q_i = \Delta u + \Delta d + \Delta s \quad (2.31)$$

As  $g_a$ ,  $\mathcal{F}$  and  $\mathcal{D}$  are known from hyperon decays, with a measurement of  $\Gamma_1^p$  one can determine  $\Sigma$ . In the simple parton model, where the nucleon consists of u and d quarks one would expect that the nucleons spin of  $\frac{\hbar}{2}$  is carried by the quarks:

$$\frac{1}{2} = \frac{1}{2}\Sigma = \frac{1}{2} \sum_{u,d} \Delta q_i \quad (2.32)$$

But various measurements have revealed that  $\Sigma$  is actually much smaller, e.g.  $\Sigma = 0.30 \pm 0.04_{\text{stat.}} \pm 0.09_{\text{syst.}}$  measured at HERMES [11].

QCD calculations have shown that the polarisation of the gluons in the nucleon have to be included in the polarised structure function  $g_1(x, Q^2)$ . One can make a next to leading order QCD approach for  $g_1(x, Q^2)$ , which includes the spin dependent gluon distribution  $\Delta G(x, Q^2)$ .

A description of the nucleons spin structure can only be successful with the knowledge of  $\Delta G(x, Q^2)$ . The determination of  $\Delta G(x, Q^2)$  is one of the central goals of the COMPASS experiment.

### 2.3.1 Measurement of $\frac{\Delta G}{G}$

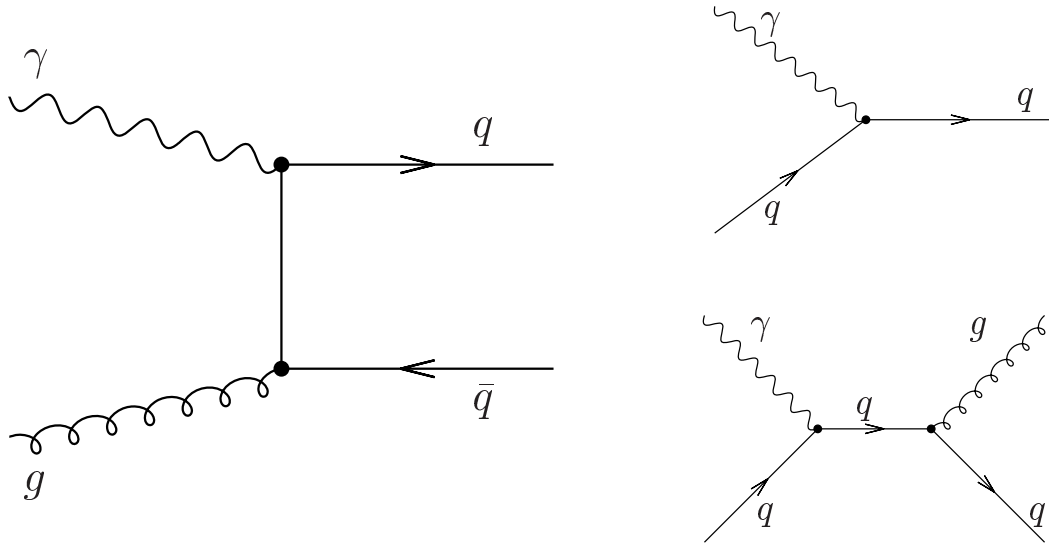


Figure 2.4: The Photon-Gluon-Fusion process (PGF) on the left and background processes on the right: DIS (top) and QCDC (bottom)

An experimental measurement of  $\frac{\Delta G}{G}$  can be done by means of the photon-gluon-fusion process (PGF), where the virtual photon couples to a gluon from the nucleon via the production of a quark anti-quark pair (Fig. 2.4). One can identify PGF processes using the fact that a charm anti-charm pair is produced, which fragments



into charmed hadrons, mainly D and D\*. Hadrons containing charm quarks that have their origin in the nucleon are improbable, as the charm content of the nucleon can be neglected.

Another possibility to identify PGF processes are events that include hadrons with a high transverse momentum with respect to the virtual photon. Their super-proportional occurrence expresses the fact that the quark-antiquark pair in the photon gluon centre-of-mass frame are produced back to back and transfer their momenta to the resulting hadrons.

After the successful tagging of the photon gluon events, one can calculate the longitudinal cross section asymmetry of the underlying process:

- charmed events:  $A_{\parallel}^{\mu N \rightarrow D/D^* X}$
- two high- $p_t$  hadrons:  $A_{\parallel}^{\mu N \rightarrow hh X}$
- one high- $p_t$  hadron:  $A_{\parallel}^{\mu N \rightarrow h X}$

The experimental technique to determine the asymmetries is presented in chapter 5.4.1.

Once, the asymmetry is calculated, it can be connected to the gluon polarisation  $\frac{\Delta G}{G}$  via:

$$\begin{aligned} A_{\parallel}^p &= R_{\text{PGF}} \langle \hat{a}_{ll} \rangle \cdot \frac{\Delta G}{G} + \text{Background} \\ \frac{A_{\parallel}^p}{D} &= R_{\text{PGF}} \langle \hat{a}_{ll}/D \rangle \cdot \frac{\Delta G}{G} + \text{Background} \end{aligned} \quad (2.33)$$

$R_{\text{PGF}}$  is the fraction of photon-gluon fusion events on all events and  $\hat{a}_{ll} = \frac{\Delta \sigma^{\gamma g}}{\sigma^{\gamma g}}$  is the analysing power.  $A_{\parallel}^p$  denotes the asymmetry for the process  $p$ , which is used to tag the PGF events, i.e. charmed or high- $p_t$  events. The background for the high- $p_t$  selected asymmetry consists mainly of QCD-Compton scattering processes leading order scattering asymmetries (see Fig. 2.4).



# Chapter 3

## The COMPASS Experiment

### 3.1 General

The **CO**mmun **MU**on and **PR**oton **AP**paratus for **S**tructure and **S**pectroscopy is situated at the CERN SPS<sup>1</sup> accelerator next to Geneva in Switzerland. It is a fixed target experiment with a high rate forward spectrometer, which performs measurements in two different configurations: the *Muon Setup* and the *Hadron Setup*.

In the Hadron Setup a beam of hadrons is used to study charmed hadron decays, light quark systems, hybrids and glue-balls as well as the structure of unstable particles.

As the analysis in this thesis is based on muon-beam data exclusively, only the Muon Setup will be presented, whereas more information about the Hadron Setup can be found in [5]. One of the main goals of COMPASS is to measure the spin-dependent transverse structure functions  $h_1(x)$  of the nucleons, the transverse parton spin distribution functions  $\Delta_T q_p(x)$  and the longitudinal parton helicity distribution functions  $\Delta q_p(x)$  at very low  $x$ . The polarised gluon distribution function  $\Delta G(x)/G$  is of particular interest. In order to calculate  $\Delta G(x)/G$  it is necessary to measure the double spin asymmetry  $A_{LL}$ . Therefore it is crucial to have both a polarised beam and a polarised target. COMPASS uses a naturally polarised muon beam on a DNP polarised lithium deuteride (<sup>6</sup>LiD) target.

The spectrometer is about 60 m long and divided in the **L**arge **A**nge **S**pectrometer (LAS) and **S**mall **A**nge **S**pectrometer (SAS) part, each equipped with a complete set of tracking and particle identification detectors. A first validation of the principle of the detector was performed in 2001. Physics data taking started 2002, and it will continue at least until 2010 with a break in 2005 due to the shutdown of the SPS and PS in view of the preparation for the new LHC accelerator and experiments.

---

<sup>1</sup>Super Proton Synchrotron

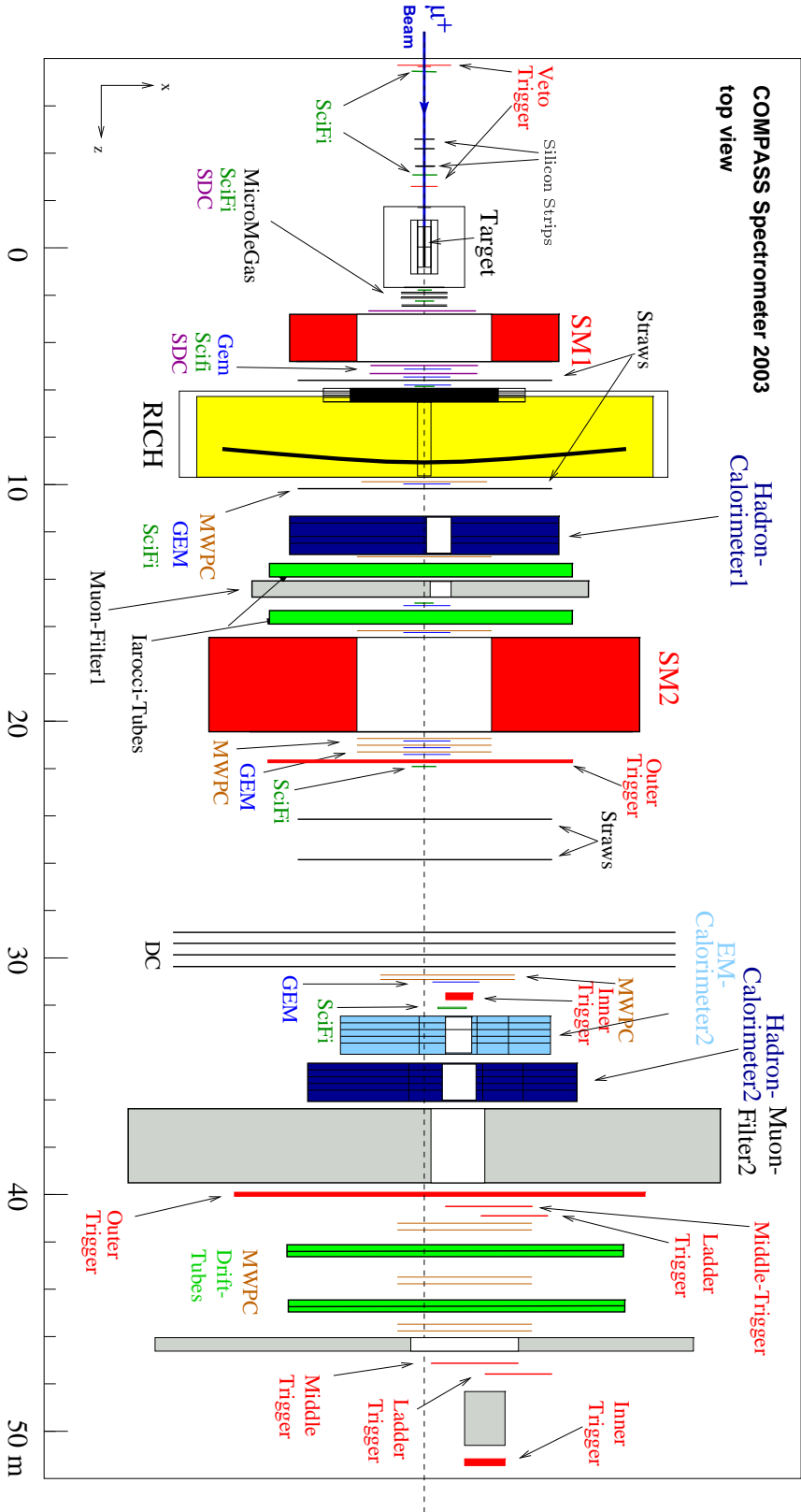


Figure 3.1: Top view of the COMPASS spectrometer of 2003;  
 Trigger System: Hodoscopes and Spectrometer Magnets (SM1 and SM2), Hadronic Calorimeters;  
 Particles Identification: RICH, Muon Filters and Hadronic Calorimeters;  
 Tracking: Silicon Strips, MicroMeGas, Scintillating Fibres (SciFi), GEMs, MWPCs, Straws, Drift Tubes;

## 3.2 The Polarised Muon Beam

The COMPASS experiment is set up at the M2 beam-line at the SPS and uses a beam of polarised  $\mu^+$  with a momentum of 160 GeV/ $c$  and an intensity of about  $2 \cdot 10^8$  particles per SPS spill. The M2 beam-line, formerly used by SMC (NA47), has been adapted to the COMPASS requirements: higher beam intensities, a smaller spot size and the possibility of a hadron beam [13].

In the 16.8 s cycle of the SPS, 400 GeV/ $c$  protons are extracted during a spill length of 4.8 s and directed at the T6 primary target, made of beryllium, where a secondary beam of pions and kaons is produced. The SPS proton intensity is between  $2 \cdot 10^{12}$  and  $1.2 \cdot 10^{13}$  per cycle and by varying the length of the T6 target, one can adjust the intensity of the secondary beam (see [14]).

Over a length of 600 m a fraction of the  $\pi$  and  $K$  decay to muons. The remaining hadrons are removed from the beam in a 9.9 m long beryllium hadron absorber. The muons are then directed towards the COMPASS experiment by means of a system of bending dipole and focusing quadrupole magnets. The spot size of the muon beam on the COMPASS target is about 8 mm with a divergence of about 0.9 mrad. Muons originating in the parity violating decay of  $\pi$  and  $K$  are naturally polarised with an average polarisation of about -0.75 with respect to the beam direction. The polarisation can be calculated from the momenta of the parent particles. The momentum of the incoming beam particle is measured by the beam momentum station (BMS), which is situated before and after the last bending magnet in front of the COMPASS polarised target and consists of four (five) hodoscopes in 2002 (2003) of scintillator counters<sup>2</sup>.

## 3.3 The Polarised Target

The COMPASS polarised target consists of the dilution refrigerator as cooling device, a superconducting magnet system, i.e. a dipole magnet (0.42 T) and a solenoid magnet (2.5 T), and a microwave cavity, in which the two cylindrical target cells, each 60 cm long and 3 cm in diameter, are situated. Between the two target cells, referred to as upstream and downstream cell is a gap of 10 cm. For hadrons originating at the beginning of the upstream target cell the maximum angular acceptance is 70 mrad. A new solenoid magnet with an acceptance of 180 mrad is planned to increase the statistics of particles at larger angles.

The target consists of two cells, which are oppositely polarised to eliminate beam flux dependencies (see Fig. 3.2). For the physics analysis described in this work the two target cells have been polarised along the beam direction. A polarisation perpendicular to the beam direction is possible for the measurement of transverse

---

<sup>2</sup>for more information about BMS, see [2] and references therein

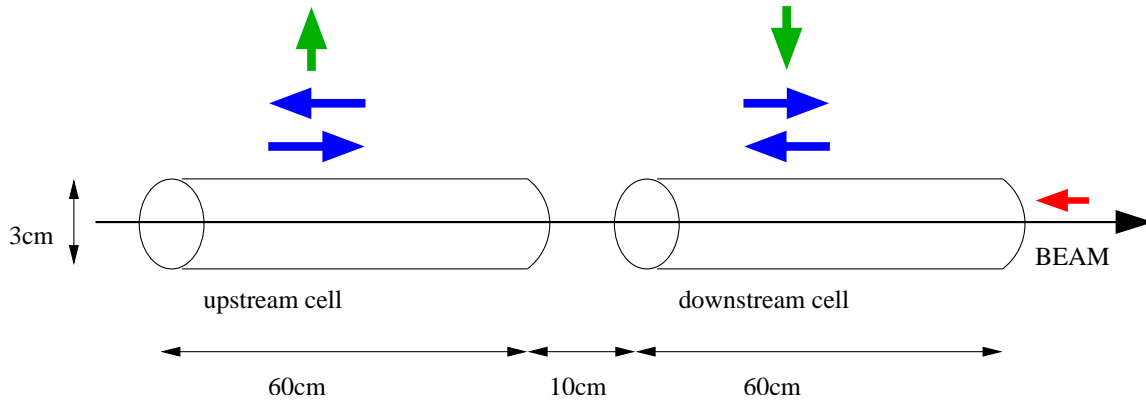


Figure 3.2: The different spin setups for the target. The two longitudinal polarisation setups (lower arrows), transversal polarisation (upper arrows) and beam polarisation. Beam direction is indicated by the black arrow.

spin distributions. To suppress systematic effects from the target acceptance the polarisation of the two target cells is flipped every eight hours by reversing the field of the solenoid magnet adiabatically.

The target material currently used, consists of frozen  ${}^6\text{LiD}$  pellets as a deuteron target, which are stored at a temperature below 65 mK. The  ${}^6\text{LiD}$  target has a thickness of about  $\rho = 59 \text{ g/cm}^2$ . The target material is polarised by dynamic nuclear polarisation (DNP). At low temperatures the relaxation time of the polarisation is about 15000 h for a magnetic field of 2.5 T (longitudinal polarisation) and 1400 h for 0.42 T (transversal polarisation)[16].

The polarisation is measured by 5 NMR coils in each target cell, which surround the target material. In 2003 maximal polarisations of +57%(-54%) for the upstream cell and +54%(-49%) for the downstream cell were reached [15].

## 3.4 Spectrometer

The two parts of the COMPASS spectrometer, the SAS for detection of particles with angles smaller than 30 mrad and the LAS for angles up to  $\sim 200$  mrad, are each equipped with tracking detectors for the reconstruction of tracks, a spectrometer magnet to measure the momentum of the reconstructed particles, hadronic and electromagnetic calorimeters and a RICH<sup>3</sup> and muon filters for particle identification. The RICH for the second and the electromagnetic calorimeter for the first

---

<sup>3</sup>Ring Imaging Čerenkov Detector

stage are not yet installed.

### 3.4.1 Spectrometer Magnets

Each spectrometer stage is equipped with a magnet(SM1 and SM2) for a measurement of the momentum and the charge of the passing particles. Charged particles are deflected in a magnetic field by the Lorentz force  $\vec{F}_L = q(\vec{v} \times \vec{B})$ . By measuring the track before and after the magnets one can calculate the momentum of a particle and determine its charge.

The bending power ( $\int \vec{B} d\vec{l}$ ) in SM1 is 1.0 Tm and 4.4 Tm in SM2 [27].

### 3.4.2 Tracking detectors

There are several different types of detectors designed for different rate capability and used to reconstruct the tracks of particles in the COMPASS spectrometers.

Only a small region around the beam is covered by the **Very Small Area Trackers**. Their purpose is to do the tracking very near or inside the beam and therefore have to endure very high beam intensities. They need an excellent time resolution to separate individual particles. There are three detectors of this type.

- **Beam Momentum Stations**(BMS) are situated upstream of the target and are used to measure the beam momentum with a resolution better than 0.7%.
- Two **Silicon Strip Detector** stations are installed upstream the target to measure the beam direction. They consist of 5 cm  $\times$  7 cm silicon wafers, with a time resolution of about 3ns and a spacial resolution better then 16  $\mu\text{m}$  [21].
- There are eight stations of **Scintillating Fibre Hodoscopes** in the detector. Each station consists of multiple layers of scintillating fibres with photomultipliers connected to the back. The time resolution is about 400 ps and the rate capability is about 1 MHz [22].

Two types of **Small Area Trackers** are utilised to obtain track information near the beam but with the centre region of highest intensities excluded.

- The three stations of **Micro Mesh Gas Detectors** (MicroMegas) with 4 planes each, are located between the target and the SM1. To increase the time resolution and rate capacity, the gaseous volume is divided into a conversion and a amplification gap [24]. This results in a time resolution of 9 ns and the spacial resolution is 70  $\mu\text{m}$ .
- Ten **Gas Electron Multipliers**(GEM) stations are distributed along the spectrometer, each equipped with two detectors. An ionising particle causes

a few free electrons by primary ionisation, which are amplified within three layers of GEM foils. The readout via a mesh provides a two-dimensional hit projection. The GEMs have a size of  $31 \times 31 \text{ mm}^2$ , a spatial resolution of  $70 \mu\text{m}$  and a time resolution of  $12 \text{ ns}$  [23].

The tracking detectors are completed by the **Large Area Trackers** which cover a region of several  $\text{m}^2$  around the beam.

- Three **Drift Chambers**(DC) stations in the region of SM1 and two large area drift chambers named **W4-5** behind SM2 are used.
- The **Straw** tracking system uses five modules each consisting of three planes. A plane is composed of two layers of kapton straw drift tubes with a diameter of 6 and 10 mm. They provide a spacial resolution of about  $270 \mu\text{m}$  and cover a region of about  $2.3 \times 1.6 \text{ m}^2$  [26].
- There are eleven stations of **Multi Wire Proportional Chambers**(MWPC).

### 3.4.3 Calorimetry

The spectrometer is equipped with two hadronic calorimeters and an electromagnetic calorimeter. HCAL1 is situated in the LAS and covers angles of  $50\text{-}150 \text{ mrad}$ , while HCAL2 and ECAL2 are in the SAS. The angular acceptance of HCAL2 is  $5\text{-}50 \text{ mrad}$ [18]. ECAL2 is currently not used in the analysis. A second electromagnetic calorimeter ECAL1 is planned and is foreseen to be placed in front of the HCAL1. The hadron calorimeters serve two aims. By measuring the energy of crossing particles, they can decrease the number of muons and electrons in the hadron data sample on the one hand and on the other hand can be used to increase the number of events with hadrons in the final state by including them in the trigger system(see 3.5). Both hadron calorimeters are iron-scintillator sandwich calorimeters and are shielded from electromagnetic background either by ECAL2 or a lead wall.

### 3.4.4 RICH

So far only the RICH in the LAS is installed and is used to identify  $\text{K}^+$ ,  $\pi^+$  and protons and their charge conjugated anti-particles (Fig. 3.4.4). It is filled with  $\text{C}_4\text{F}_{10}$ , which has a refractive index of  $n \approx 1.00153$  [12]. Particles with a velocity  $\beta c$  above the threshold  $\beta = 1/n$  emit Čerenkov light at an angle  $\theta = \arccos(1/n\beta)$ . This yields a limit for the identification of particles with momenta bigger then  $p_{\pi,K,p} \approx 2.5, 8.9, 17.0 \text{ GeV}/c$ .

The emitted photons are reflected by the mirrors at the rear side of the RICH and detected in the MWPC photon detectors, placed above and below the acceptance



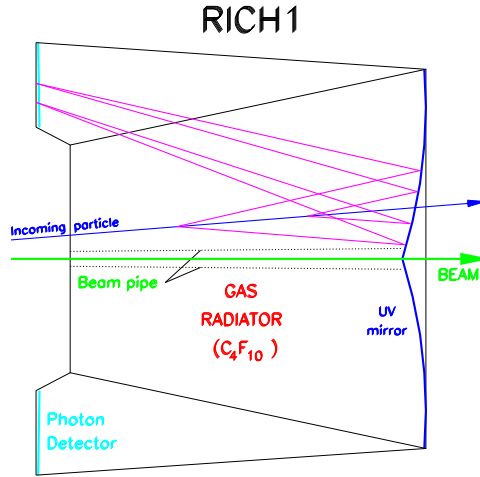


Figure 3.3: The COMPASS RICH 1

region.

By reconstructing the rings of the emitted photons one can measure the velocity  $\beta$  of particles crossing the RICH. It is therefore possible to calculate probabilities for particle types.

### 3.4.5 Muon filters

To identify muons the spectrometer is equipped with two muon detectors, MW1 and MW2, which contain passive absorbers and tracking devices and two additional muon filters with passive absorbers and hodoscopes. MW1 consists of a 60 cm iron absorber, surrounded by Plastic Iarocci Tubes. MW2 is a 2.4 m concrete wall with drift tube detectors [25].

## 3.5 Trigger System

One of the main features of the COMPASS experiment is its ability to measure  $\Delta G/G$  over a wide range in  $Q^2$ , especially at very low  $Q^2$ . This requires a trigger system which is sensible down to very low scattering angles  $\Theta$ . In this kinematical region it is important to select events where the energy  $\nu$  of the quasi-real photon suffices to produce a  $c\bar{c}$  pair for the Open-Charm analysis of the photon-gluon-fusion. Furthermore, a minimal  $\nu$  leads to a minimal  $y$ , which is desired because the polarisation of the photon is related to the polarisation of the muon via the

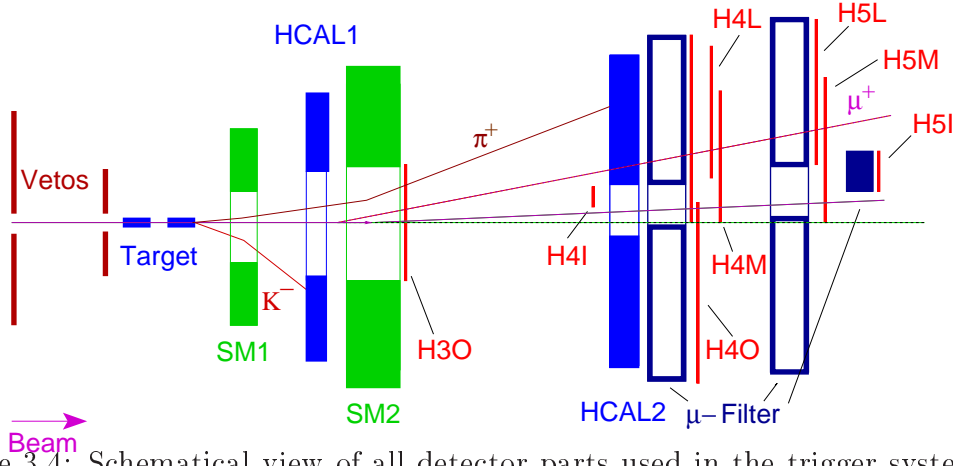


Figure 3.4: Schematical view of all detector parts used in the trigger system from [18]: trigger hodoscopes (red), hadronic calorimeters (blue) and veto hodoscopes (dark red)

depolarisation factor  $D(y)$ , which is approximately proportional to  $y$ .  $\nu_{min} = 45$  GeV and therefore  $y_{min} \approx 0.3$  was chosen [18].

To fulfil these demands the spectrometer is equipped with different scintillator strip hodoscopes. The signals are combined to form the triggers for different kinematic ranges (Fig. 3.4). The Inner Trigger (HI04/05) and the Ladder Trigger (HL04/05) are used for  $Q^2 < 0.5$  GeV<sup>2</sup>/c<sup>2</sup>. For the intermediate range of  $0.5$  GeV<sup>2</sup>/c<sup>2</sup>  $< Q^2 < 1.0$  GeV<sup>2</sup>/c<sup>2</sup> the Middle Trigger (HM04/05) and for larger values of  $Q^2$  the Outer Trigger (HO03/04/05) are available. The different hodoscope stations are combined in a coincidence matrix for target pointing, to make sure that the scattering took place inside the target.

As most of the analyses at COMPASS, e.g. the Open-Charm analysis and the High- $p_t$  analysis, include the detection of hadrons in the final state, the two hadron calorimeters (HCAL1/2) are also included in the trigger system. The Calorimeter Trigger requires an energy deposit in a cluster sum of  $4 \times 4$  modules in one of the calorimeters bigger than 5.4 GeV, which is three times the typical energy loss of a muon. The Calorimeter Trigger is combined with the Inner, Ladder and Middle Trigger. To reduce the rate of background events taken by the DAQ Beam Veto Counters are used. The veto system consists of hodoscopes situated upstream of the target, leaving the centred beam region uncovered. The veto is combined with the Ladder, Middle and Outer Trigger (see Tab. 3.1).

Table 3.1: Inclusion of the HCAL and the Vetos in the different trigger

Inner	Ladder	Middle	Outer	Calorimeter	Incl. Middle
IT	LT	MT	OT	CT	IMT
Calo	Calo $\wedge$ $\bar{V}'$	Calo $\wedge$ $\bar{V}_{\text{tot}}$	$\bar{V}_{\text{tot}}$	$\bar{V}_{\text{tot}}$	$\bar{V}_{\text{tot}}$

## 3.6 Data Acquisition System

Up to now, the information of the 190 k detector channels have been read and combined to events at a trigger rate of 5 kHz to 10 kHz by the COMPASS DAQ. With a event size of  $\sim 40$  kB this corresponds to a data rate of 200 MB/s during the 4.8 s effective spill time in a SPS cycle.

The detector information is for most of the cases digitised directly at the detector, e.g. if time information is required with an F1-TDC chip [19]. It is read out by 134 CATCH and GeSiCA interface boards and transferred via optical links to 16 Readout Buffer PCs (ROBs), where the transfer rate is reduced by using the cycle time without beam. Data belonging to the same trigger is marked by an unique event number. It is transported to 12 Event Builder PCs via a Gigabit Ethernet and combined to events. The data is grouped in runs of 100 or 200 spills. The event builders send the data to the CERN central tape recording. In the case of transfer problems the event builders provide disc space of 7.68 TB for buffering, which corresponds to two days of data taking. More on the DAQ system can be found in [20].



# Chapter 4

## Inclusive Cross Sections

As pointed out earlier, it is very important to be able to measure inclusive differential cross sections. It is the basis for the determination of the semi-inclusive cross section measurement, which will be presented in the Chapter 5. The inclusive cross section in deep inelastic scattering of muons and nucleons can be expressed in terms of  $F_2(x, Q^2)$ , which has been measured by various previous experiments in a wide range of  $x$  and  $Q^2$  and the cross section is reasonably well known. Thus, the measurement of the inclusive cross section can be a good test for the understanding of the detector and the Monte Carlo event reconstruction.

How the cross section is calculated, both with real and Monte Carlo data is the topic of this chapter. First results for the differential cross section will be shown and compared to Monte Carlo data and earlier measurements done at the NMC-Experiment.

### 4.1 Experimental Determination of the Cross Section

In this section the technique used to calculate the cross section for a specific process from experimental data is described. In section 2.1.1 it was already shown, how the inclusive differential cross section can be expressed in terms of  $F_{1,2}(x, Q^2)$  (Eq. 2.6). Together with the Callan-Gross relation (Eq. 2.20) one obtains:

$$\frac{d\sigma}{dx dQ^2} = \frac{4\pi\alpha^2}{Q^4 x} \cdot F_2(x, Q^2) \left[ 1 - y - \frac{Q^2}{4E^2} + \left( 1 - \frac{2m^2}{Q^2} \frac{y^2 + Q^2/E^2}{2(1 + R(x, Q^2))} \right) \right] \quad (4.1)$$

Experimentally it is obvious that the event rate for a given  $x$  and  $Q^2$  is proportional to the luminosity, which is the product of the beam flux  $\Phi$  times the number of

target particles  $N_t$ :

$$\frac{d}{dt} \frac{d^2 N(x, Q^2)}{dx dQ^2} \propto L = \Phi \cdot N_t \quad (4.2)$$

The proportionality constant between the event rate and the luminosity is the differential cross section  $d^2\sigma/dx dQ^2$ .

$$\frac{d}{dt} \frac{d^2 N(x, Q^2)}{dx dQ^2} = \frac{d^2\sigma}{dx dQ^2} \cdot L \quad (4.3)$$

Not the event rates are determined in the experiment but the number of events are counted for a certain amount of time. By integrating Eq.4.3 one obtains for the differential cross section:

$$\int \frac{d}{dt} \frac{d^2 N(x, Q^2)}{dx dQ^2} dt = \frac{d^2\sigma}{dx dQ^2} \cdot \int L dt \quad (4.4)$$

$$\Rightarrow \frac{d^2\sigma}{dx dQ^2} = \frac{\int \frac{d}{dt} \frac{d^2 N(x, Q^2)}{dx dQ^2} dt}{\int L dt} = \frac{1}{\mathcal{L}} \cdot \frac{d^2 N(x, Q^2)}{dx dQ^2} \quad (4.5)$$

Here,  $\mathcal{L}$  is the integrated luminosity.

$$\mathcal{L} = \int \Phi dt \cdot N_t = \frac{N_t}{A} \cdot N_b \quad (4.6)$$

$N_b$  is the number of beam particles crossing the target area  $A$ . To calculate the number of target particles per area, Avogadro's number  $N_A = 6.0221 \cdot 10^{23}$  1/Mol, the length of the target, the thickness  $\rho \cdot l$  and the Mol mass of the target particles is needed. For nucleons this is  $M_M = 1.00749$  g/Mol. For the number of target particles per area can be written:

$$\frac{N_t}{A} = \frac{N_A}{M_M} \cdot \frac{\rho V}{A} = \frac{N_A}{M_M} \cdot \rho \cdot l \quad (4.7)$$

The total weight of the target material was determined for 2002 and 2003 (see [28]). With  $M_T$  and  $r$  from [28], the thickness can then be calculated:

$$\rho \cdot l = \frac{M_T}{A} = \frac{M_T}{\pi r^2} \quad (4.8)$$

Here,  $M_T$  is the mass of the target material, and  $A$  is the area of the target in the beam direction. The unfilled height at the top of the target has to be considered for the calculation of  $A$ . It is about  $h \approx 0.1$  cm. The values for the target thickness and the number of beam particles per area can be seen in Tab. 4.1.

Table 4.1: Magnitudes to calculate the number of target particles per area;  $r$  and  $M_T$  from [28]

Year	$r$ [cm]	$A$ [cm <sup>2</sup> ]	$M_T$ [g]	$\rho \cdot l$ [g/cm <sup>2</sup> ]	$N_T/A$ [1/(cm <sup>2</sup> )]
2002	1.5	7.00	$346.9 \pm 3.4$	$49.6 \pm 0.7$	$(2.96 \pm 0.03) \cdot 10^{25}$
2003	1.5	7.00	$350.2 \pm 3.4$	$50.0 \pm 0.7$	$(2.99 \pm 0.03) \cdot 10^{25}$

The number of beam particles  $N_b$  is counted by the scintillating fibre station 2 and can be accessed via the `PHAST::TotalBeamFlux()` function (see Chapter 4.4.1). Another factor has to be introduced, as Eq. 4.5 is only valid for a perfect detector with 100% geometrical acceptance and detection efficiency. For a real detector one has consider the detector efficiency  $\epsilon$  defined as the number of detected events divided by the number of all events. In a given  $x$  and  $Q^2$  region, the efficiency is:

$$\epsilon(x, Q^2) = \frac{N_{\text{Events}}^{\text{Detected}}(x, Q^2)}{N_{\text{Events}}^{\text{All}}(x, Q^2)} \quad (4.9)$$

$\epsilon$  can be calculated with a Monte Carlo simulation. The correctness of the determination of the efficiency strongly depends on the accuracy of the detector model, which is included in the Monte Carlo. With the detector efficiency from Eq. 4.9, Eq. 4.5 becomes:

$$\frac{d^2\sigma}{dx dQ^2} = \frac{1}{\epsilon(x, Q^2)} \cdot \frac{1}{\mathcal{L}} \cdot \frac{d^2N(x, Q^2)}{dx dQ^2} \quad (4.10)$$

The first step to determine the differential cross section is to calculate the number of events. A careful selection of data and events is necessary, as a large part of the data cannot be used for several reasons explained in the next Chapter.

## 4.2 Event and Data Selection

After the event reconstruction, the experimental data is stored in so-called mDST files which can be analysed with PHAST. Only events containing a primary vertex are saved. For the inclusive analysis only mDST data for the period P1I-slot 3<sup>1</sup> from the year 2003 is used. A preselection of all produced COMPASS data is done and kinematical cuts are applied. The selection criteria which will be described, are applied in the real data analysis. But most of them are valid for the Monte Carlo analysis, too. If not, it will be pointed out later, when Monte Carlo data is studied.

---

<sup>1</sup>September 2004

### 4.2.1 Data Selection

In this analysis only longitudinal data is used, i.e. data taken with a longitudinally polarised target.

To exclude bad runs, the run list of the COMPASS stability page (see [32]) is used. All runs taken during the reversal of the solenoid field are removed from the data set.

One has to take into account that not every spill of the selected runs can be used. The data quality has been analysed on a spill by spill level for several conditions of detector stability and lists of bad spills are available (see [33]). Bad spills have been removed from the analysed data set.

### 4.2.2 Event Selection

#### Basic Event Quality

Having done this first rough data selection, the next step is to select events, which meet the physics requirements. To be sure that an interaction took place in the target we impose the requirement that

- the event contains **exactly one primary vertex**.

The rejection of events with more than one primary vertex is done to ensure the unique identification of the vertex. This cut reduces the sample size by roughly 15% (see Tab. 4.4). Three percent of these events are discarded, because more than one primary vertex exists. The rest contains no primary vertex because either the beam particle or the scattered muon could not be reconstructed.

The primary vertex has to lie inside the target. More precisely it has to be localised inside the target volume which is actually filled with target material. The vertex position in the beam direction, i.e. the  $z$  component, is constrained by the  $z$  position of the target cells:

- $z_{\text{Vertex}} \in \{z \mid -100\text{cm} < z < -40\text{cm} \vee -30\text{cm} < z < 30\text{cm}\}$

The limitations for the  $x$  and  $y$  positions of the primary vertex are given by the radius of the target and by the fact that the target is not completely filled with  ${}^6\text{LiD}$ . The empty upper region of the target is excluded by limiting the  $y$  position of the primary vertex. In addition, the target is slightly inclined with respect to the nominal  $z$ -axis. The location of the target upstream and downstream centre for 2002 and 2003 can be seen in Tab. 4.2.

For the coordinates of the primary vertex position with respect to this inclined target axis, the following cuts are applied:



- the distance to the target axis is smaller then 1.4 cm  

$$r = \sqrt{x_{Vertex}^2 + y_{Vertex}^2} < 1.4cm$$
- $y_{Vertex} < 1.0cm$

Table 4.2: Positions of the target centre at the upstream and downstream end of the target

Year	Upstream Centre			Downstream Centre		
	x/cm	y/cm	z/cm	x/cm	y/cm	z/cm
2002	-0.2	0.1	-100	-0.3	-0.15	30
2003	0.04	0.03	-100	-0.03	-0.2	30

These cuts are visualised in Fig. 4.1 and remove about 45% of the remaining events.

All distributions, shown in this Chapter, are divided by the bin width. For the raw distributions, which are shown for comparison, only a primary vertex and a scattered muon is requested. In all figures in this Chapter, the raw distributions are scaled by a factor  $f = \frac{N^{Final}}{N^{Raw}}$  to simplify a direct comparison to the final data sample.  $N^{Final}$  ( $N^{Raw}$ ) is the number of entries in the final (raw) data sample where only entries in the visible bin range are considered.

To provide information about the inclusive scattering the reconstructed event must contain a scattered muon attached to the primary vertex. Another requirement is to make sure that an event is triggered by a muon and not by a hadron. This is done by checking the last measured z-position of the track of the scattered muon. This z-position should be greater or equal to the last detector, which formed the trigger. This is checked for every trigger in the event (see Tab. 4.3).

Furthermore, the extrapolation of the track of the beam muon should cross the whole target. Again, the inclination of the target and the empty upper region has to be considered. To allow only events with beam muons which cross both target cells is necessary to guarantee the measurement of unpolarised scattering. Otherwise, the contributions of the oppositely polarised target cells would be different.

By the basic event selection criteria presented in this Section, about 65% of the data are rejected.

### Kinematic Cuts

Besides the beam muon and the target particle, only the scattered muon is considered in the inclusive analysis. Thus, if the target and projectile momenta are fixed, the

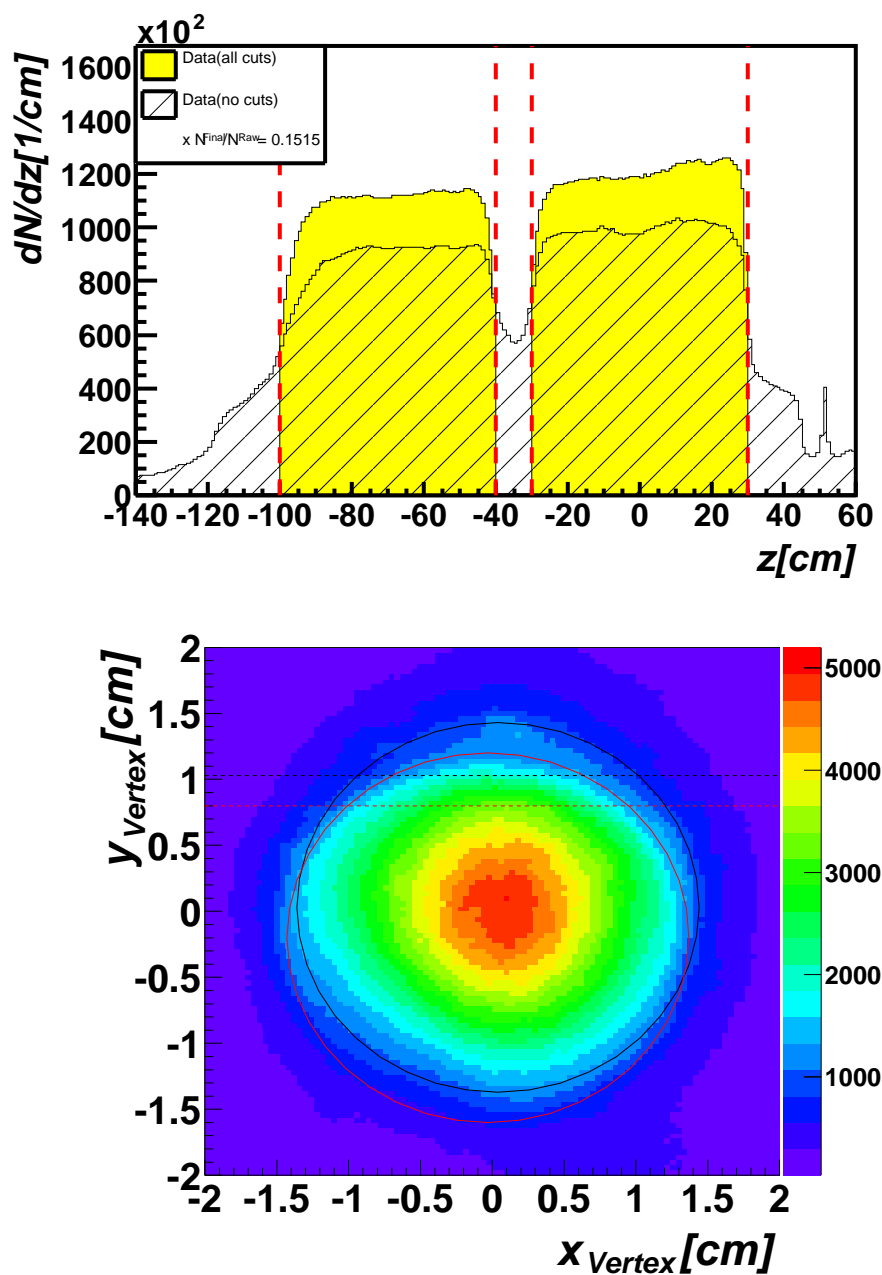


Figure 4.1:  $z$  distribution (top) and  $x$ - $y$  distribution (bottom) of the primary vertex in raw data and inclusive sample; the cuts are indicated by the red dashed lines; the black (red) lines in the  $x$ - $y$  distribution refer to the cuts at the beginning (end) of the upstream (downstream) cell; the raw data is scaled by a factor  $f = \frac{N^{Final}}{N^{Raw}}$

Table 4.3: Positions and bits of the trigger system

Trigger		Bit	z Positions/cm <sup>2</sup>	
Inner Trigger	IT	1	3172 (HI04)	5096 (HI05)
Middle Trigger	MT	2	4024 (HM04)	4776 (HM05)
Ladder Trigger	LT	4	4056 (HL04)	4808 (HL05)
Outer Trigger	OT	8	2100 (HO03)	4002 (HO04)
Calorimeter Trigger	CT	16	1267 (HCAL1)	3602 (HCAL2)
Inclusive Middle Trigger	iMT	256	4024 (HM04)	4776 (HM05)

event can be fully described by two variables. For example, one can chose  $x$  and  $Q^2$  or  $y$  and  $Q^2$ . The variables are connected via (see Tab. 2.1):

$$x = \frac{Q^2}{2M\nu} = \frac{Q^2}{2MEy} \quad (4.11)$$

Table 4.4: Event statistics after the applied cuts

Event Numbers in Inclusive Scattering		
Cut	Number of Events in P1I	% of data sample
All events	189565141	100
Primary vertex ex.	167938751	88.5
Only one p. vertex	161306085	85.0
P. vertex inside target	89308633	47.1
$\mu$ in p. vertex	68423852	36.0
Only one $\mu$ in p. vertex	68423852	36.0
Beam inside target	64142875	33.8
Scattered $\mu$ in trigger hod.	57052530	30.0
$Q^2 > 0.2 \text{ GeV}/c^2$	19925444	10.5
$0 < x < 1$	18893446	9.9
$0.1 < y < 0.9$	13616952	7.1

$M \approx 0.94 \text{ GeV}$  is the nucleon mass.  $E$  is the beam energy, which can safely be written as  $E = \sqrt{m^2c^2 + \vec{p}^2} \approx \vec{p}^2 = 160 \pm 5 \text{ GeV}$  (see Fig. 4.2). Due to the small muon mass ( $m = 0.105 \text{ GeV}/c^2$ ) in comparison to the beam momentum

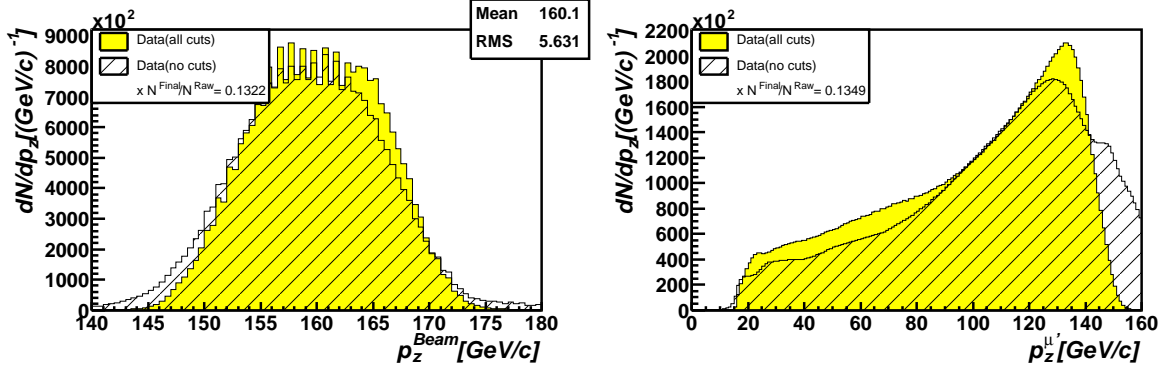


Figure 4.2: Momenta of the incoming (left) and the scattered (right) muons

$P \approx 160 \text{ GeV}/c$  the term  $m^2c^2$  can be neglected.

In this inclusive analysis cuts are applied on  $y$  and  $Q^2$ .

- $0.1 < y < 0.9$   
The small  $y$  region is excluded, as the scattering is merely elastic there. Events with very high  $y$  are rejected, due to high radiation corrections which are theoretically difficult.
- $Q^2 > 1.0 \text{ GeV}/c^2$  in the case LEPTO is used as Monte Carlo generator; LEPTO can only simulate events in this kinematical region.
- $Q^2 > 0.2 \text{ GeV}/c^2$  in the case PYTHIA the Monte Carlo generator is used.

The distribution of the kinematical variables with the cut on  $Q^2 > 0.2 \text{ GeV}/c^2$  can be seen in Fig. 4.3. Again, the raw distributions are normalised to the number of entries in the plots with all cuts.

### 4.3 Monte Carlo

The Monte Carlo studies serve two purposes in this analysis. By comparing kinematical variables the theoretical understanding of the simulated process can be tested. Different theoretical models are implemented in the Monte Carlo code.

In this analysis, the Monte Carlo generated data will also be used to determine the detector efficiencies, needed to calculate the differential cross section. The production of Monte Carlo data, the comparison to the real data and the determination of the detector efficiencies for inclusive events will be the topic of this Chapter.

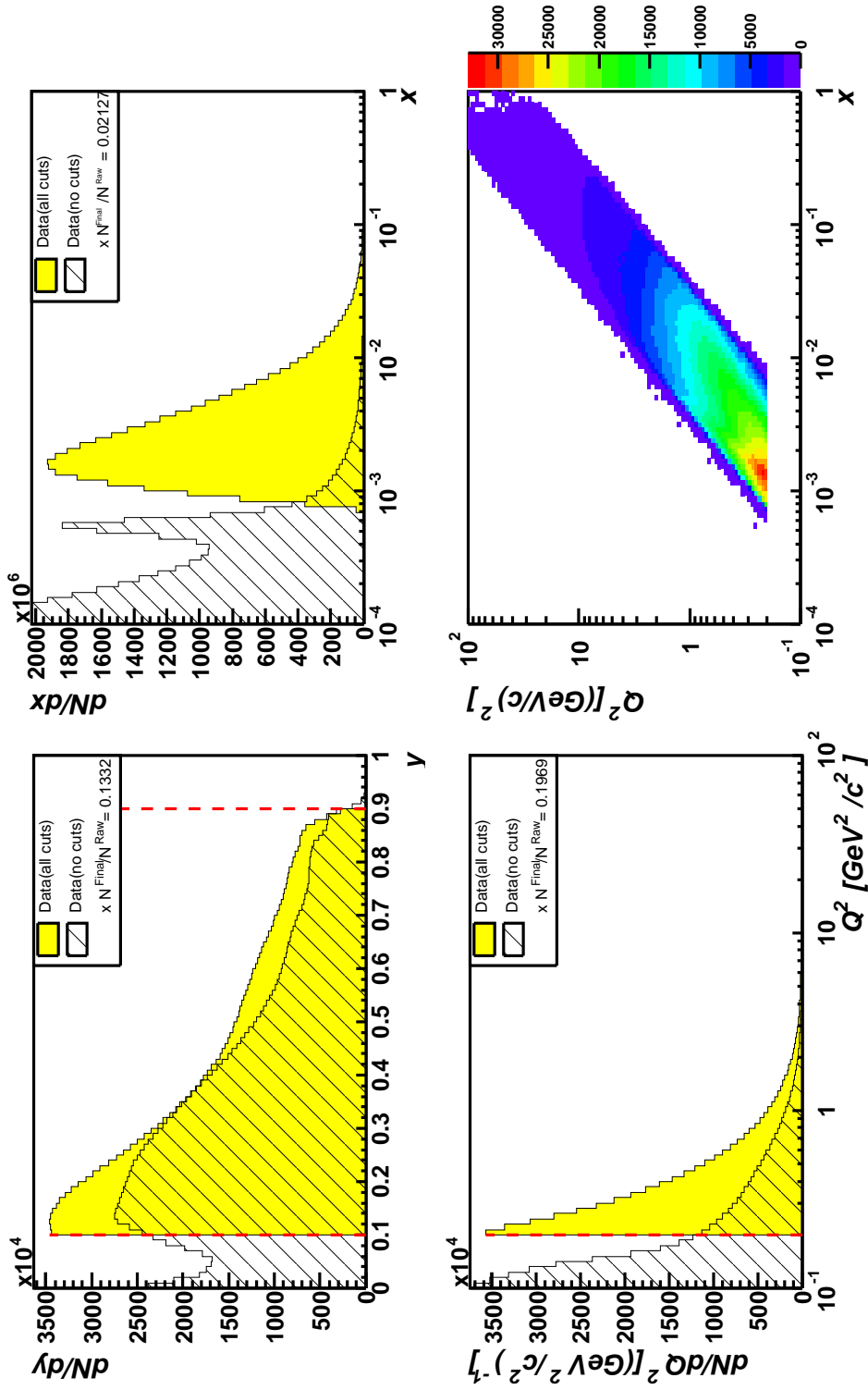


Figure 4.3: Kinematical distributions for inclusive scattering:  $y$  (top left),  $x$  (top right),  $Q^2$  (bottom left) and  $Q^2$  versus  $x$  (bottom right); only the final data sample is plotted for the  $Q^2$  versus  $x$  distribution; the peak in the  $x$  distribution of the raw data is caused by the elastic scattering of the muon off an electron

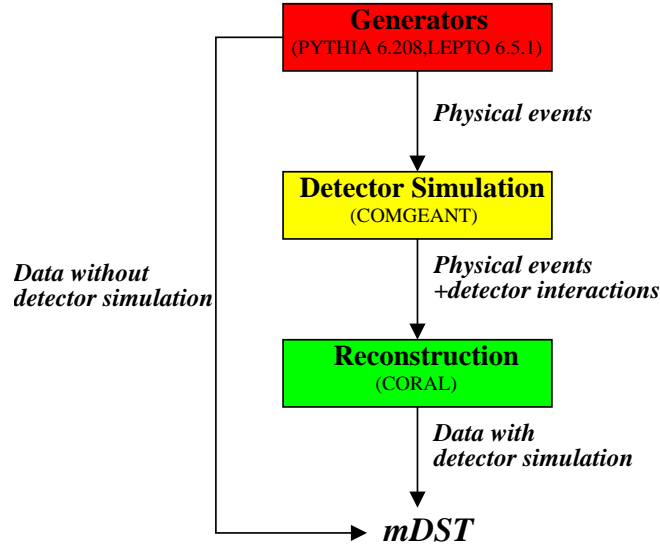


Figure 4.4: The Monte Carlo Chain

### 4.3.1 The Monte Carlo Chain

The goal of the Monte Carlo production is an output of randomly generated data reproducing the shape of the real data. To simplify the analysis, it is desirable that the storage format of the Monte Carlo is the same as for real data. This is provided by a concatenation of different programs (see Fig. 4.4).

The base of the Monte Carlo production is the generator. In this analysis PYTHIA 6.208 and LEPTO 6.5.1 are used. They can simulate physical events in a user given kinematical range. Whereas PYTHIA can produce a huge variety of processes over the whole  $Q^2$  range (see [29]), LEPTO [30] is restricted to QCD-Compton scattering, Photon-Gluon-Fusion and leading order DIS.

It is possible to store the simulated events without tracking or detector information in the same data format as for real data. This data can be used, if no detector information is needed. To take interactions of particles in the detector into account, the generated data can be passed to COMGEANT, which is a GEANT 3.21 based simulation of the COMPASS detector. Additional decays of the generated particles, deflections in the magnetic fields and interactions of the particles with detector components are simulated in COMGEANT. In this analysis COMGEANT 7.01 is used with an updated trigger simulation (“omgbatch\_ntrig4”).

The same reconstruction software as for real data (CORAL<sup>3</sup>) is used to produce the data output. Detector information such as triggers and RICH information is

<sup>3</sup>COMPASS Reconstruction ALgorithm

included. Additionally, all information about the generated event is still available, such as the process type or the initial kinematics. The values of the kinematical variables in the reconstructed data are smeared with respect to the generated values.

Therefore one has two levels of information, namely the generated information which evolves from the Monte Carlo generator and the reconstructed information, where all detector attributes enter.

Both generators, LEPTO and PYTHIA, are used in the analysis, and whenever it is possible, kinematical cuts were already included in the event generation. An a-priori restriction of the kinematics accelerates the production of the Monte Carlo data, as the data would otherwise be discarded afterwards.

### 4.3.2 Real Data versus Monte Carlo

After the complete production chain, the Monte Carlo data is available in the same format as the real data. The requirements for the reconstructed events used in the analysis are thus identical with the requirements for real data.

In contrast, the extraction of the generated data out of the mDSTs needs a little change in the analysis software. For the generated events one does not need to check the muon's detection after the last trigger hodoscope as the type of each particle is included in the generated information and the muon can therefore clearly be identified.

#### PYTHIA with default parameters

A comparison between PYTHIA generated Monte Carlo data and real data is shown in Fig. 4.5. Therefore,  $5 \cdot 10^5$  events were generated with the PYTHIA default parameters and reconstructed in the Monte Carlo chain. In PYTHIA, the CTEQ5L parametrisation of the parton distribution functions is used by default.

The applied kinematical cuts for the reconstructed events are  $0.1 < y < 0.9$  and  $Q^2 > 0.2 \text{ GeV}/c^2$ . It is important that the cuts used to generate the events are a bit wider as the cuts later applied in the analysis. This becomes necessary, due to the smearing of the kinematical variables in the reconstruction. Reconstructed events can slightly be shifted from their reconstructed kinematical values and will be cut away. If no events are generated outside the applied cuts this effect is not compensated by events that are shifted to values inside the chosen kinematical range. The cuts on the generator are  $0.05 < y < 0.95$  and  $Q^2 > 0.15 \text{ GeV}/c^2$ .

In the left column of Fig. 4.5, a direct comparison between the real (filled histograms) data, the generated Monte Carlo (blue lines) and the reconstructed Monte Carlo data (red lines) is shown. A normalisation factor for the Monte Carlo data of  $f = \frac{N^{\text{Data}}}{N^{\text{MC}}}$

Data compared to Monte-Carlo  
PYTHIA defaults (CTEQ5L)

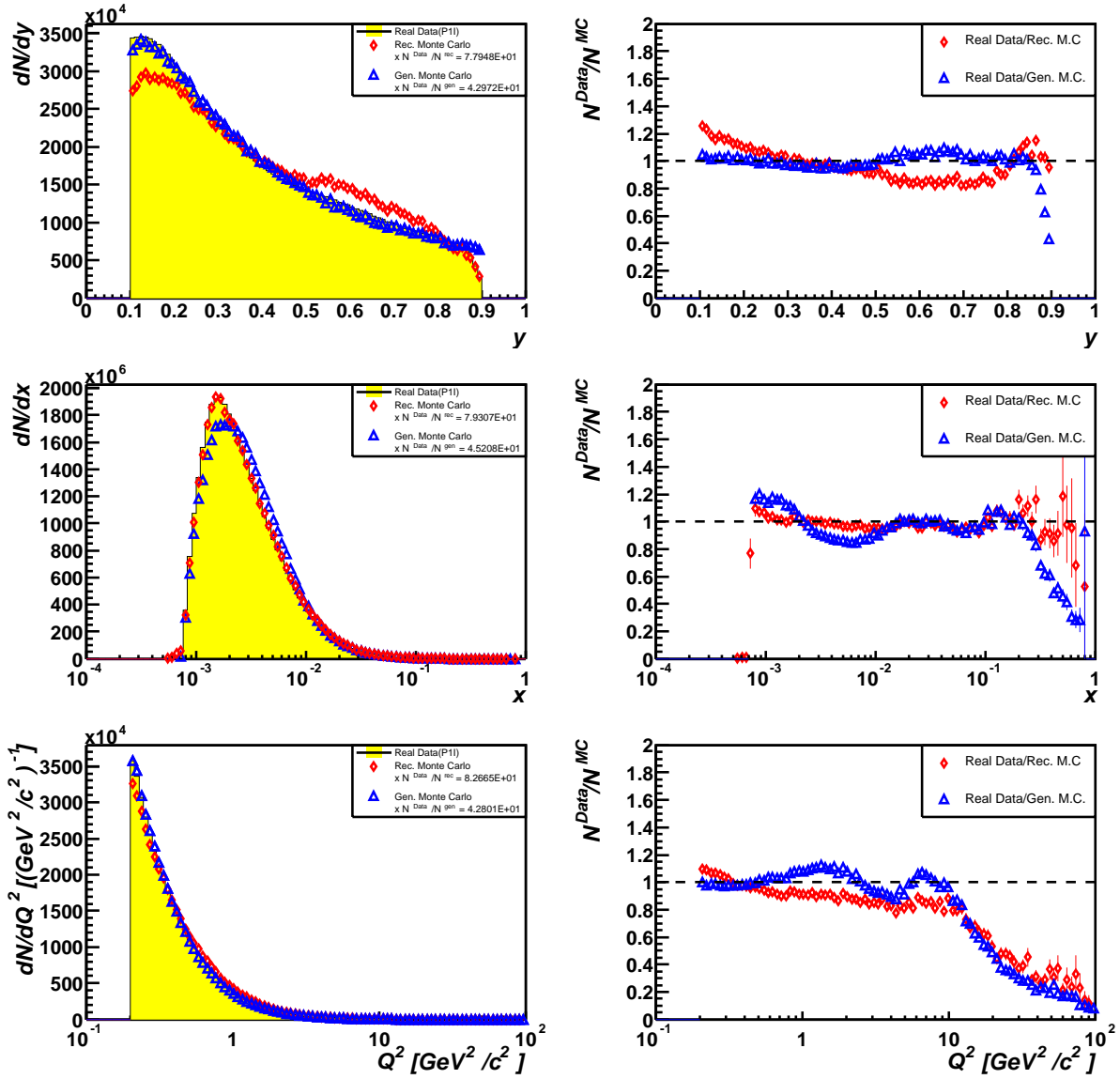


Figure 4.5: Comparison of kinematic distributions  $y$  (top),  $x$  (middle),  $Q^2$  (bottom) in real data with Monte Carlo for default parameters in PYTHIA; a direct comparison (left column) and the ratios of data and Monte Carlo (right column) are shown; Monte Carlo data is scaled with a factor  $f = \frac{N_{Data}}{N_{MC}}$



is applied.  $N$  is the number of all entries in the histograms. On the right side the ratios of the real data divided by the normalised Monte Carlo data are shown. Obviously, the  $y$  distribution is nicely reproduced, whereas the number of events for  $x > 0.3$  is overestimated by PYTHIA. For  $Q^2 > 10 \text{ GeV}/c^2$  there is also a strong overestimation of the number of events in the Monte Carlo. But looking at the left column it is clear that only a very small fraction of events is affected.

### **PYTHIA with GRV94M**

To improve the description of the inclusive kinematical variables, a second set of parameters for PYTHIA was tried.  $5 \cdot 10^5$  events were produced with the GRV94M next to leading order parton distribution functions. This corresponds to the PYTHIA option  $\text{MSTP}(51)=5$ .

Additionally the cross section for the deep inelastic scattering was changed to the quark-parton-model by setting  $\text{MSTP}(19)=0$ . The result can be seen in Fig. 4.6. The  $y$  distribution is equally good as for the PYTHIA default parameters, but the  $x$  and  $Q^2$  distributions seem even worse. With the default setting, PYTHIA generated too many events for  $x > 0.3$  and the number of events is now underestimated. The  $Q^2$  distribution looks equally bad. The cross section is underestimated for  $1 \text{ GeV}/c^2 < Q^2 < 10 \text{ GeV}/c^2$  and then overestimated.

### **LEPTO with default parameters**

LEPTO is a second generator for Monte Carlo data and it is interesting to look at the comparison of the output of this generator with the real data. The LEPTO data for the default settings, where the CTEQ2L parton distribution functions are used, is shown in Fig. 4.7.

For the real data, the  $Q^2$  cut is now  $Q^2 > 1 \text{ GeV}^2/c^2$  to match the Monte Carlo data. One can easily see that the data is not very well described by the standard settings of the LEPTO generator. While the  $y$  distributions for the range  $0.3 < y < 0.8$  and the  $Q^2$  distributions for  $Q^2 < 10 \text{ GeV}^2/c^2$  reasonably match, the Monte Carlo  $x$  distribution is shifted to larger values and is less wide than in the real data.

### **LEPTO with GRV98L**

As a second set of parton distribution functions in LEPTO, GRV98L was used (see Fig. 4.8). The description of the data is slightly improved with this new parameter set. The real data is now well described down to  $y \approx 0.2$  and for a small range around  $x \approx 0.01$ .

Data compared to Monte-Carlo  
 PYTHIA with GRV94

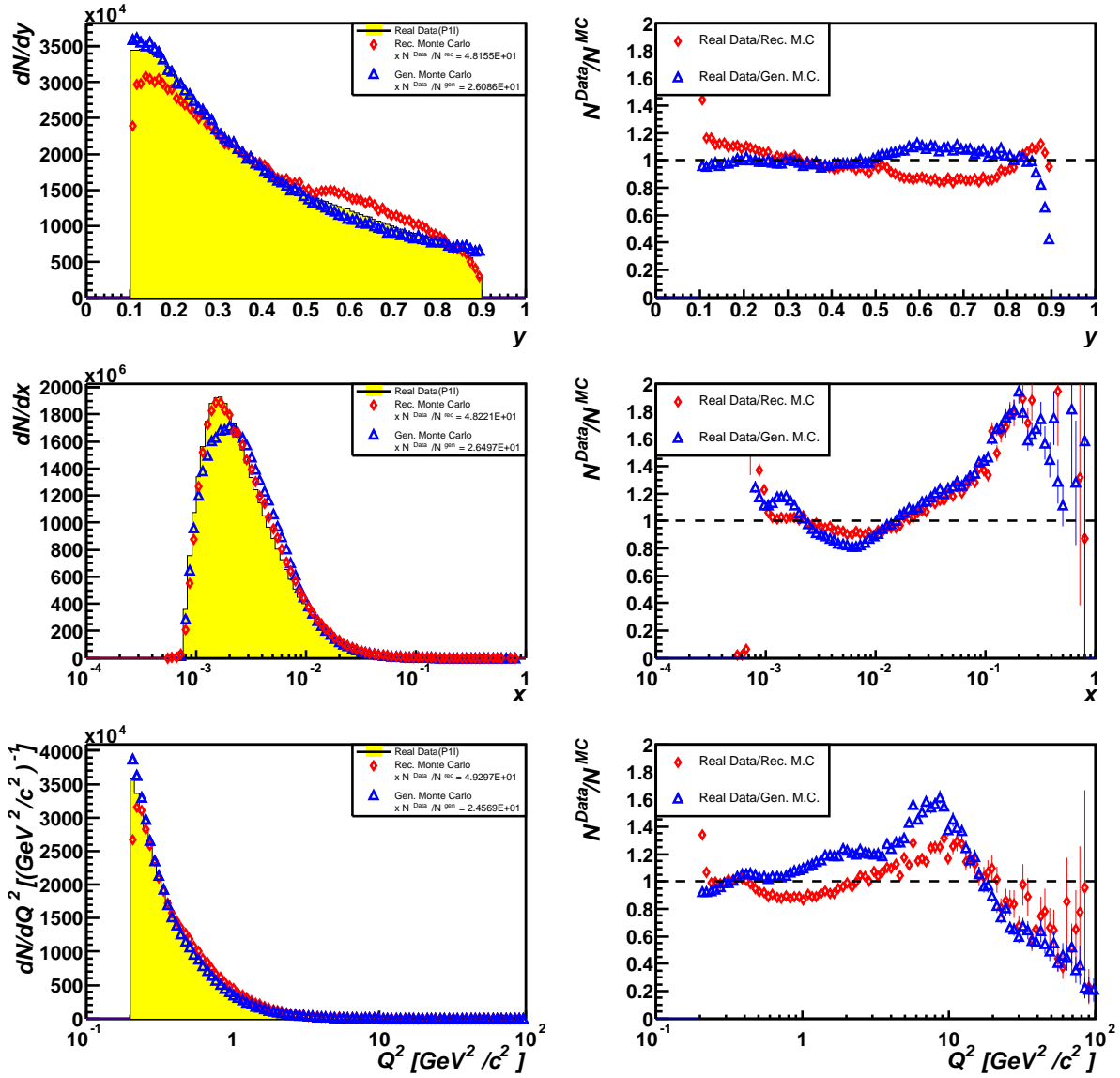


Figure 4.6: Comparison of kinematic distributions  $y$  (top),  $x$  (middle),  $Q^2$  (bottom) in real data and PYTHIA Monte Carlo with GRV94 parton distribution functions; a direct comparison (left column) and the ratios of data and Monte Carlo (right column) are shown; Monte Carlo data is scaled with a factor  $f = \frac{N_{Data}}{N_{MC}}$

Data compared to Monte-Carlo  
LEPTO defaults (CTEQ2L)

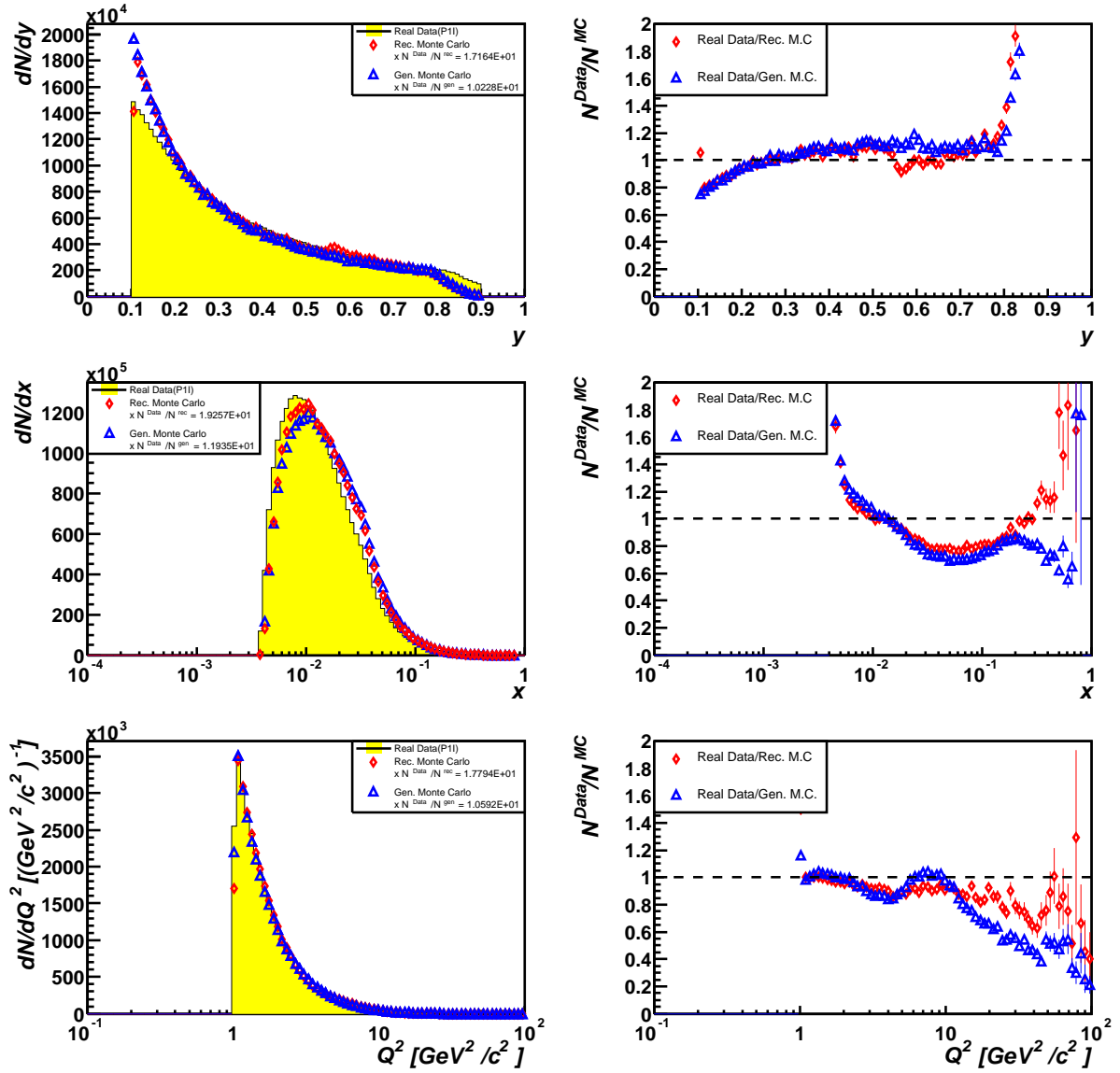


Figure 4.7: Comparison of kinematic distributions  $y$  (top),  $x$  (middle),  $Q^2$  (bottom) in real data and LEPTO Monte Carlo with CTEQ2L parton distribution functions; a direct comparison (left column) and the ratios of data and Monte Carlo (right column) are shown; Monte Carlo data is scaled with a factor  $f = \frac{N_{Data}}{N_{MC}}$

Looking at Fig. 4.5 to Fig. 4.8 one can conclude that the data sample is best described by the PYTHIA generator with the default settings, which means using the CTEQ5L parton distribution functions. The overestimation of the number of events for generated and reconstructed Monte Carlo data for all generator settings could be explained by an overestimation of the efficiency in this range.

### 4.3.3 Monte Carlo Cross Sections

Table 4.5: Total cross sections and generated Events for LEPTO and PYTHIA with different PDFs

	LEPTO		PYTHIA	
PDF	CTEQ2L	GRV98L	CTEQ5L	GRV94M
Parameter	Default	LST(15)=5012, LST(16)=2	Default	MSTP(51)=5, MSTP(19)=0
$\sigma_{\text{MC}}^{\text{tot}}/\mu\text{b}$	0.1939	0.1999	0.3527	0.6097
$N_{\text{gen}}^{\text{tot}}/1000$	500	500	500	500
$\frac{\sigma_{\text{MC}}^{\text{tot}}}{N_{\text{gen}}^{\text{tot}}}/\mu\text{b}$	$3.878 \cdot 10^{-7}$	$3.998 \cdot 10^{-7}$	$7.0537 \cdot 10^{-7}$	$1.2194 \cdot 10^{-6}$

Before the detector efficiencies are calculated, it is of interest to look at the accuracy of the cross sections included in the Monte Carlo generator and comparing it to experimental results of the NMC experiment. For the determination of the cross section only the generated data is needed.

To determine the luminosity for the generated Monte Carlo, the total cross section for the event generation  $\sigma_{\text{gen}}^{\text{tot}}$  is needed. The generator's total cross section depends on the chosen PDFs and the kinematical range of the generation. The value of  $\sigma_{\text{gen}}^{\text{tot}}$  is extracted from the generator's log files.

Furthermore the total number of generated events  $N_{\text{gen}}^{\text{tot}}$  is necessary. This number can differ from the number of events in the output files, because many events are discarded after the generation but are counted by the generator. The ratio of the total cross section with the number of generated events is the luminosity  $\mathcal{L}_{\text{MC}} = \frac{N_{\text{gen}}^{\text{tot}}}{\sigma_{\text{gen}}^{\text{tot}}}$  and is used to determine the  $x$  and  $Q^2$  dependent cross section. The luminosities for LEPTO and PYTHIA with the different parameter sets can be seen in Tab. 4.5. To calculate the differential cross section, the  $x$  and  $Q^2$  distribution of the event numbers is necessary. To obtain it, one has to normalise the histogram of  $N(x, Q^2)$  by dividing it by the bin width in  $x$  and  $Q^2$ .

The differential cross section is then given by:

Data compared to Monte-Carlo  
LEPTO with GRV98L

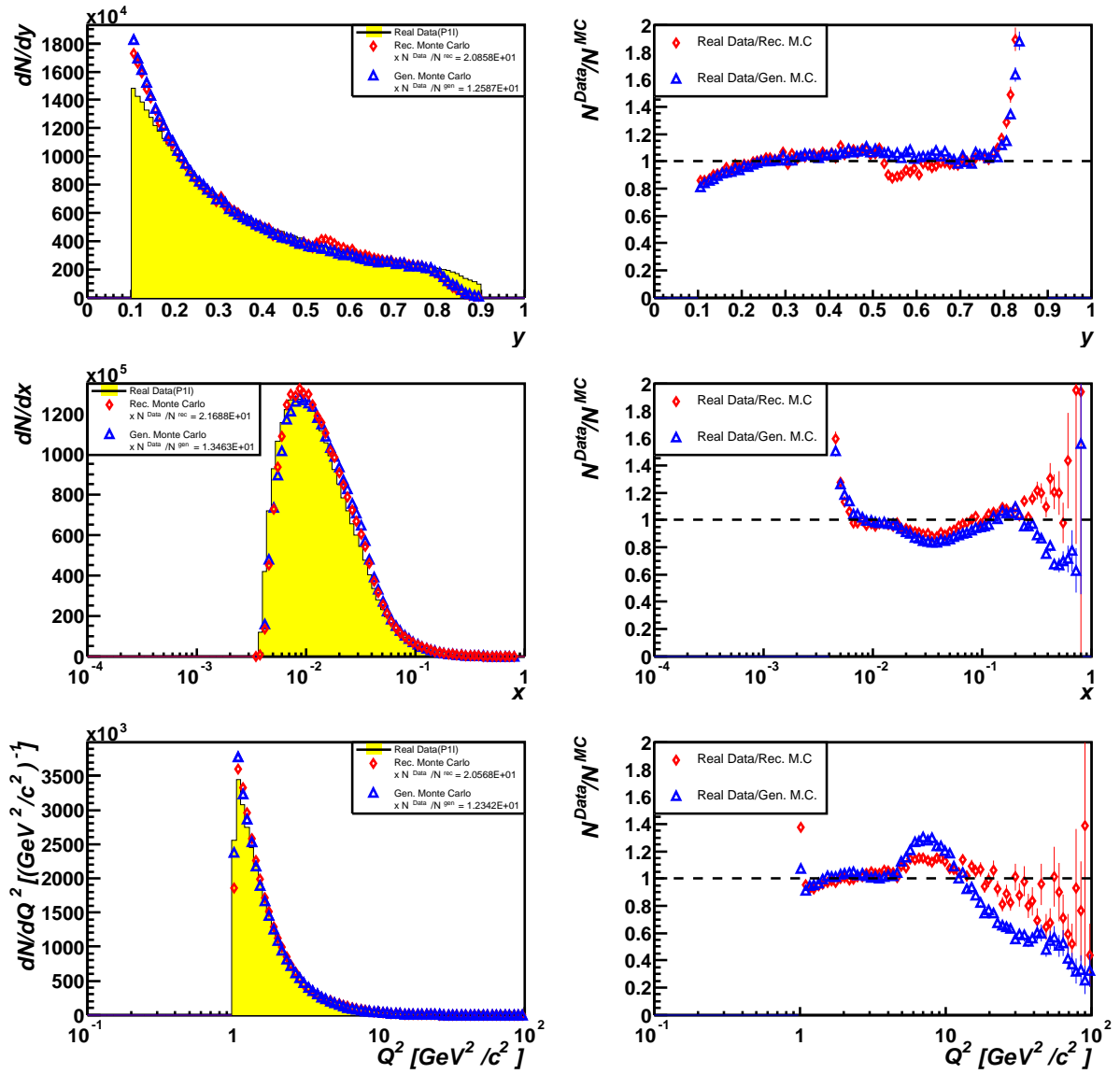


Figure 4.8: Comparison of kinematic distributions  $y$  (top),  $x$  (middle),  $Q^2$  (bottom) in real data and LEPTO Monte Carlo with GRV98L parton distribution functions; a direct comparison (left column) and the ratios of data and Monte Carlo (right column) are shown; Monte Carlo data is scaled with a factor  $f = \frac{N_{\text{Data}}}{N_{\text{MC}}}$

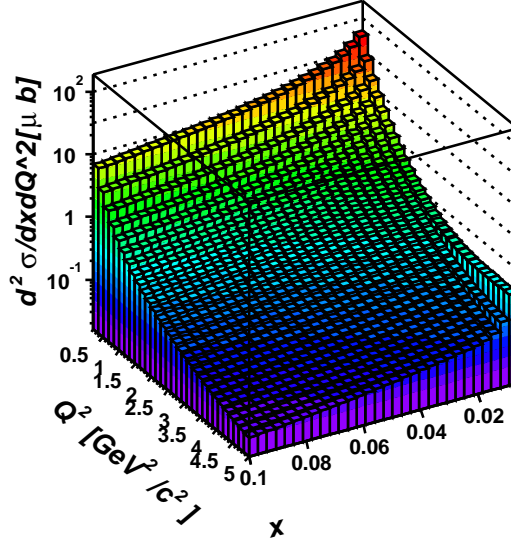


Figure 4.9: Differential cross section measured at NMC [34]

$$\frac{d^2\sigma(x, Q^2)}{dx dQ^2} = \frac{1}{b_x b_{Q^2}} \cdot \frac{1}{\mathcal{L}_{\text{MC}}} \cdot \frac{d^2 N_{\text{gen}}(x, Q^2)}{dx dQ^2} \quad (4.12)$$

$$= \frac{1}{b_x b_{Q^2}} \cdot \frac{\sigma_{\text{gen}}^{\text{tot}}}{N_{\text{gen}}^{\text{tot}}} \cdot \frac{d^2 N_{\text{gen}}(x, Q^2)}{dx dQ^2} \quad (4.13)$$

Here,  $b_x$  ( $b_{Q^2}$ ) is the bin width of the  $x$  ( $Q^2$ ) axis.

The cross section has been measured for example in the NMC experiment [34]. To extract a parametrisation for the differential cross section, Eq.2.6 can be rewritten in terms of  $F_2(x, Q^2)$ :

$$\frac{d^2\sigma}{dx dQ^2} = \frac{4\pi\alpha^2}{Q^4} \frac{F_2(x, Q^2)}{x} \left\{ 1 - y - \frac{Q^2}{4E^2} + \left( 1 - \frac{2m^2}{Q^2} \right) \frac{y^2 + Q^2/E^2}{2(1+R)} \right\} \quad (4.14)$$

$R = \frac{\sigma_L}{\sigma_T} \approx 0.2$  is the ratio of the longitudinally and transversely polarised virtual photon absorption cross section. With a parametrisation of  $F_2(x, Q^2)$  the cross section can be calculated and is shown in Fig.4.9.

The comparison of the cross sections obtained with PYTHIA for the two parameter sets and the cross section measured at NMC is shown in Fig 4.10. The plotted quantity is the ratio of the two values:

$$R = \frac{(d^2\sigma/dxdQ^2)^{\text{gen}}}{(d^2\sigma/dxdQ^2)^{\text{NMC}}} \quad (4.15)$$

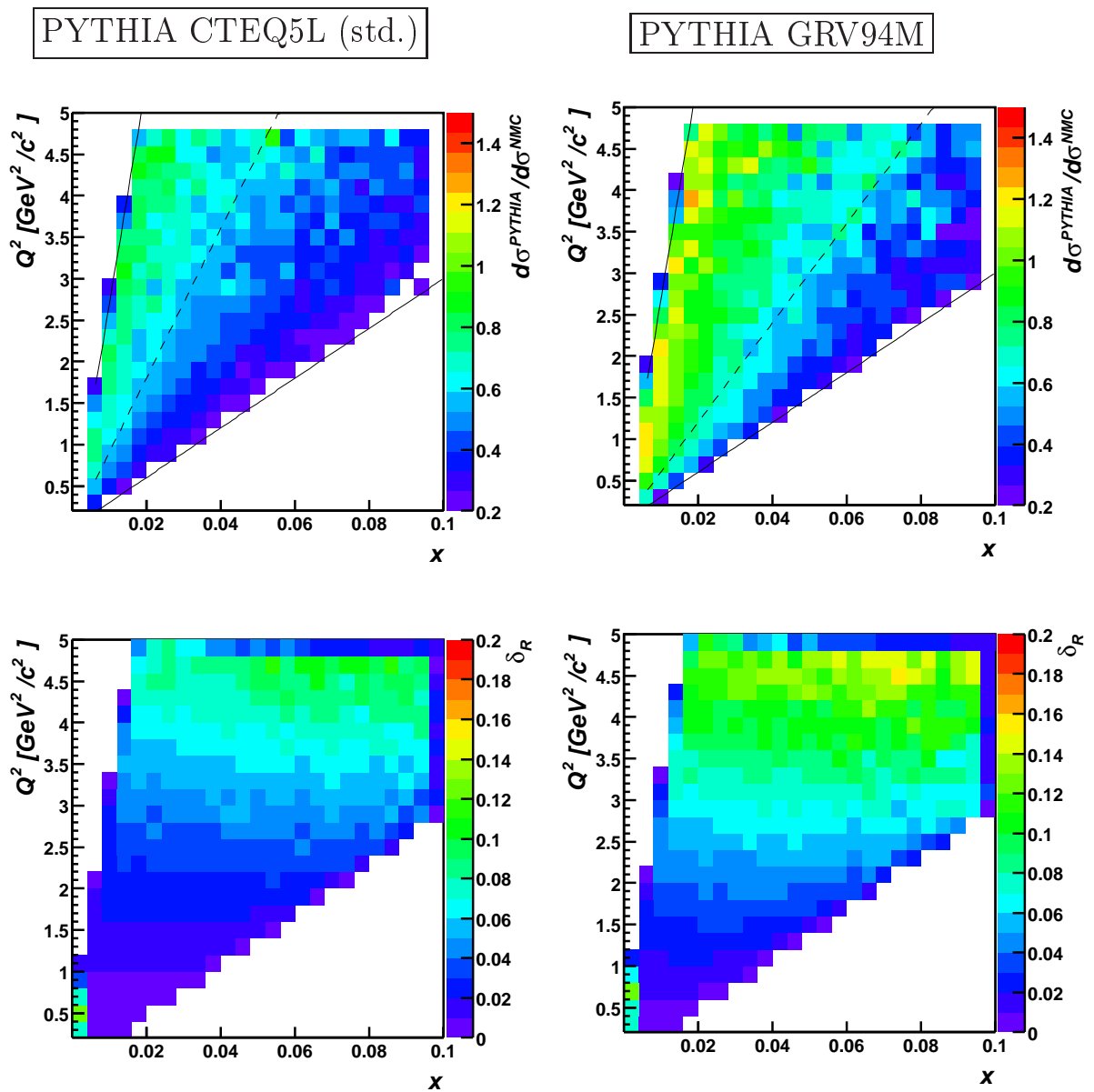


Figure 4.10: The upper row shows the ratios of the cross sections from PYTHIA and NMC for the default parameters (left) and the modified PDF GRV94 (right); the bottom row shows the statistical errors

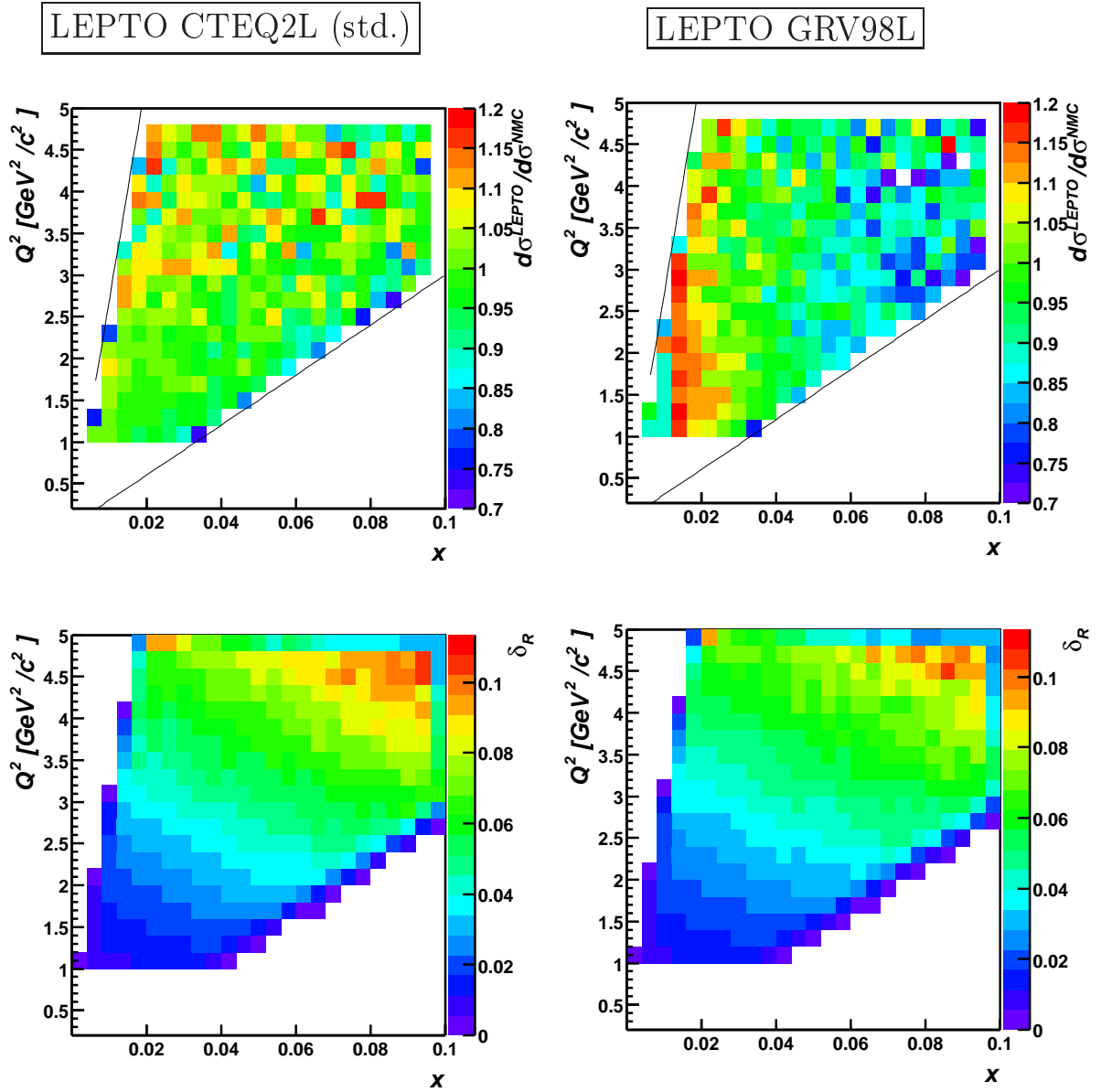


Figure 4.11: The upper row shows the ratios of the cross sections obtained from LEPTO and NMC for the default parameters (left) and the modified PDF GRV98L (right); the bottom row shows the statistical errors



The statistical error for the number of generated events is given by  $\delta_N(x, Q^2) = \sqrt{N(x, Q^2)}$ . The error of the ratio can then be calculated as:

$$\delta_R(x, Q^2) = \frac{1}{(d^2\sigma/dxdQ^2)_{\text{NMC}}} \cdot \frac{1}{b_x b_{Q^2}} \cdot \frac{\sigma_{\text{gen}}^{\text{tot}}}{N_{\text{gen}}^{\text{tot}}} \cdot \sqrt{\frac{d^2 N_{\text{gen}}(x, Q^2)}{dxdQ^2}} \quad (4.16)$$

Despite the fact that the PYTHIA generator together with the standard settings delivers the best description of the data, the NMC cross section can only be reproduced for  $y > 0.3$ . This region is indicated by the dashed line in the left plot in Fig. 4.10 with a deviation of about 20%. For the GRV94M PDFs this region extends to  $y > 0.2$ , indicated by the dashed line in the right plot. In this range the number of events are mainly overestimated by PYTHIA (see Fig 4.6).

Looking at the results for the LEPTO generator in Fig. 4.11, the agreement with the NMC data is very good, especially for the standard settings (about 5% deviation). One can summarise, that the chosen data sample is better described by the output of the PYTHIA generator, whereas the differential cross section is better implemented by LEPTO. This is in contradiction to the fact, that the kinematical distributions should be a direct derivation of the cross section. A possible explanation is, that the bad description in the LEPTO generator sum up to describe the cross section in a correct way.

#### 4.3.4 Efficiencies

To extract the differential cross section from the real data, the detector efficiency  $\epsilon$  is needed (see Eq. 4.10). If one assumes, that the detector is described correctly in the Monte Carlo, one can identify the number of detected events in the real data with the reconstructed events in the Monte Carlo data and the number of all events in the real data with the generated events in the Monte Carlo data. Thus, the efficiency can be calculated according to:

$$\epsilon(x, Q^2) = \frac{N_{\text{Events}}^{\text{Reconstructed}}(x, Q^2)}{N_{\text{Events}}^{\text{Generated}}(x, Q^2)} \quad (4.17)$$

$N_{\text{Events}}^{\text{Reconstructed}}$  and  $N_{\text{Events}}^{\text{Generated}}$  are both Gaussian distributed with an error of  $\delta_N = \sqrt{N}$  and with the Gaussian error propagation one obtains for the error of the efficiency, which follows the distribution of Poisson:

$$\delta_\epsilon(x, Q^2) = \sqrt{\frac{\epsilon(x, Q^2) \cdot (1 - \epsilon(x, Q^2))}{N_{\text{Events}}^{\text{Generated}}}} \quad (4.18)$$

In the Monte Carlo production, it is important, that the information about all generated events is used. To determine the number of reconstructed and generated

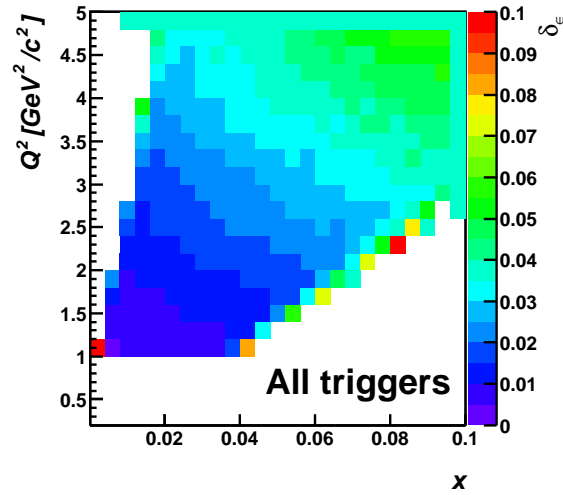
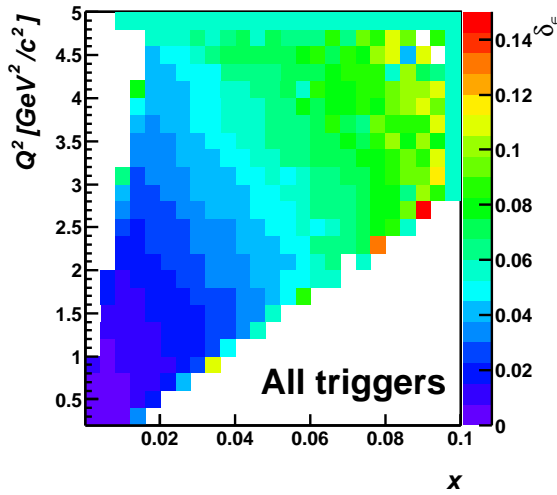
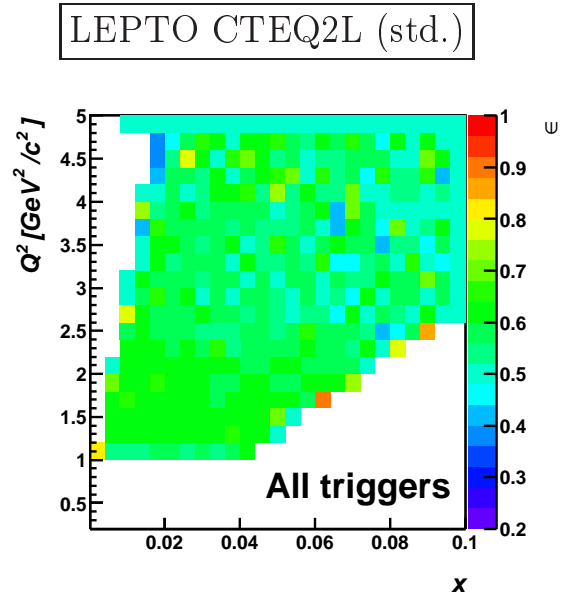
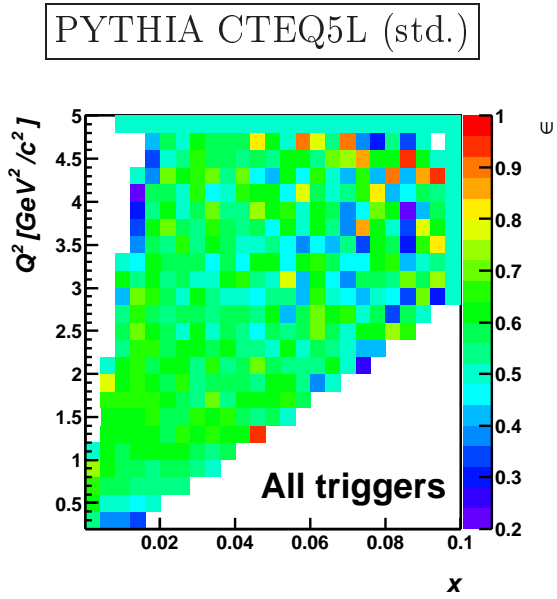


Figure 4.12: The detector efficiency calculated with PYTHIA generator (standard parameters) in the top row; statistical errors in the bottom row

Figure 4.13: The detector efficiency calculated with LEPTO generator (standard parameters) in the top row; statistical errors in the bottom row

events the same cuts as for the real data are used.

Now it is possible to calculate the efficiency with the Monte Carlo simulation by dividing the number of reconstructed events for each  $x$  and  $Q^2$  bin by the number of generated events. The efficiencies for the default parameters and their errors are shown in Fig. 4.12 and Fig. 4.13. The efficiency for both LEPTO and PYTHIA is  $\epsilon \approx 0.6$  over the whole analysed kinematical range.

The statistical errors, deduced from Eq. 4.18 are also shown in Fig. 4.12 and Fig. 4.13.

## 4.4 Measured Inclusive Cross Sections

For the determination of the inclusive cross sections with Eq. 4.10 and Eq. 4.6 the following values are calculated so far:

- The number of target particles per area  $\frac{N_T}{A}$  (see Tab. 4.1)
- The distribution of events  $\frac{d^2 N(x, Q^2)}{dx dQ^2}$  (see Fig. 4.3)
- The detector efficiency  $\epsilon(x, Q^2)$  (see Fig. 4.12 and Fig. 4.13)

The last missing quantity in order to calculate the luminosity is the number of beam particles.

### 4.4.1 Beam Flux and Luminosity

In order to calculate the integrated luminosity one must determine the flux of beam particles. Only the number of beam particles is needed, that hit the target in the time interval of data taking:  $\mathcal{L} = \frac{N_t}{A} \cdot N_b$  (see Eq. 4.6). As already mentioned, PHAST provides a function named TotalBeamFlux(), that returns the count of the scaler in the scintillating fibre station two (FI02) (see [35]). But this is not the number that is needed to calculate the integrated luminosity, because all muons that cause a hit in the station are counted. Here, only these beam particles crossing the target cells are of interest.

To get the correct number one has to multiply the number of counted muons by a factor  $r = \frac{R_{Tracks}}{R_{Scaler}}$ , where  $R_{Tracks}$  is the rate of reconstructed beam particles, that cross the target and  $R_{Scaler}$  is the rate of beam particles counted by FI02. The complete information about reconstructed beam particles is not available in PHAST, as only information about muons, that interacted with the target is saved. To calculate the true number of beam particles, an analysis with CORAL is necessary, which has been done in [35]:

$$r = \frac{R_{Tracks}}{R_{Scaler}} = 0.859 \pm 0.002_{\text{stat.}} \pm 0.025_{\text{sys.}}$$

$$\Rightarrow N_{\text{Beam}} = r \cdot N_{\text{Beam}}^{\text{Scaler}} \quad (4.19)$$

Now, this is still not accurate, as we have another effect, caused by the dead time of the DAQ. The event rate is evidently reduced by the dead time of the DAQ, as the detector remains insensitive after each event for a dead time period  $\tau$ . This reduces the number of relevant beam particles (see [31]):

$$N'_{\text{Beam}} = N_{\text{Beam}} \cdot e^{R_{\text{Event}}\tau} \quad (4.20)$$

$N_{\text{Beam}}$  is the corrected number of beam particles of Eq. 4.20 and  $R_{\text{Event}}$  is the event rate. Eq. 4.20 can be expanded to:

$$N'_{\text{Beam}} = N_{\text{Beam}} \cdot e^{R_{\text{Event}}\tau} \quad (4.21)$$

$$= N_{\text{Beam}} \left( 1 - R_{\text{Event}}\tau + \frac{(R_{\text{Event}}\tau)^2}{2} + \dots \right) \quad (4.22)$$

$$\approx N_{\text{Beam}} (1 - R_{\text{Events}}\tau) = N_{\text{Beam}} \left( 1 - \frac{N_{\text{Events}}}{t_0} \tau \right) \quad (4.23)$$

$$\approx N_{\text{Beam}} - N_{\text{Events}} \frac{N_{\text{Beam}}}{t_0} \tau \quad (4.24)$$

$$\approx r \cdot N_{\text{Beam}}^{\text{Scaler}} - N_{\text{Events}} \cdot r \cdot \Phi \quad (4.25)$$

$N_{\text{Events}}$  is the number of events, taken by the DAQ in the time interval  $t_0$  and  $\Phi$  is the flux of beam particles, counted by FI02. With a dead time of the DAQ of  $5 \cdot 10^{-6}$ s (see [35]) and a typical event rate of 10 kHz, the neglected terms of Eq. 4.22 can be estimated to be about 0.1%:

$$\Delta_N \leq \frac{\frac{(R_{\text{Event}}\tau)^2}{2}}{1 - R_{\text{Event}}\tau} \approx 0.001 \quad (4.26)$$

This can be neglected safely. The corrected number of beam particles for each run and the beam fluxes are shown in Fig. 4.14. The integrated luminosity is:

$$\mathcal{L} = \frac{N_A}{M_M} \cdot \rho \cdot l \cdot N'_{\text{Beam}} \quad (4.27)$$

The integrated luminosity for the period P1I-slot-3 is  $\mathcal{L} = 0.0969 \pm 0.0010 \text{ fb}^{-1}$

## 4.4.2 Results

All that is left to do now is to follow Eq. 4.10. To obtain the differential cross section, the number of events in each  $(x, Q^2)$  bin has to be divided by the integrated luminosity, calculated in Chapter 4.4.1, the detector efficiency and the bin width.

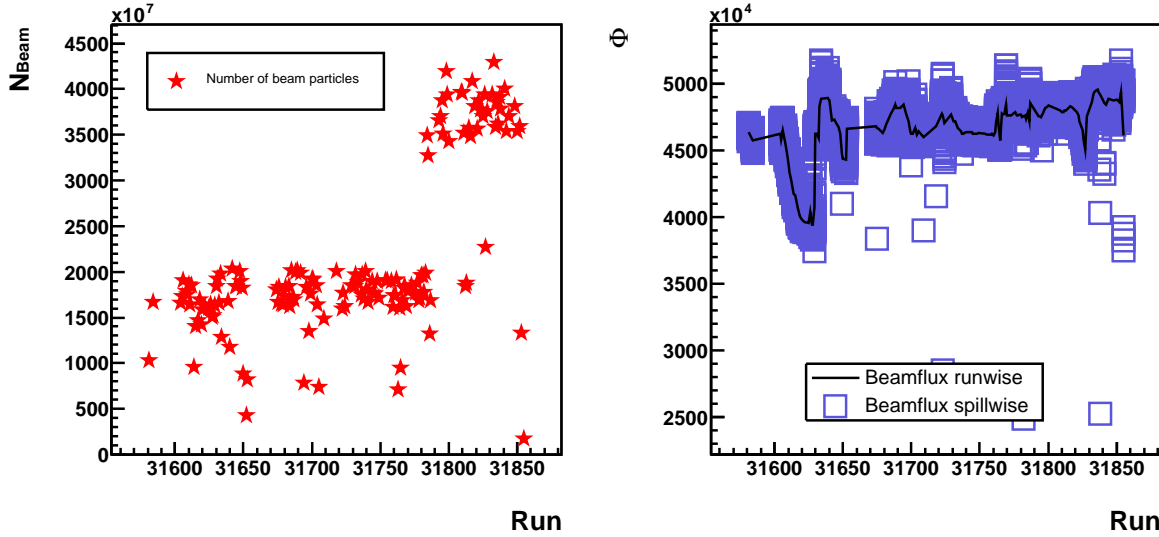


Figure 4.14: The total number of relevant beam particles (left) and the beam flux (right); for the beam flux, the values of each spill and the average for each run are plotted

The results for the  $x$  and  $Q^2$  dependent inclusive cross section at COMPASS, obtained with detector efficiencies of the PYTHIA generated Monte Carlo is shown in the top row of Fig. 4.15. In the left column, the standard settings for PYTHIA are used, i.e. the CTEQ5L parton distribution functions. In the left column the data is generated using GRV94M PDFs. Note that the graph is rotated around the z-axis by  $180^\circ$  to improve the illustration. Errors and values for the cross section are given in App. A.1.

The second row shows the ratio  $R$  of the measured cross section divided by the generator cross section, determined in Chapter 4.3.3.

In the third row, the ratio of the cross section with the value measured at the NMC experiment can be seen. The results obtained with the LEPTO generated Monte Carlo data is shown in Fig. 4.16. Again, the two columns correspond to the two generator settings.

Note, that the results for the LEPTO efficiencies have a cut off for values  $Q^2 < 1 \text{ GeV}^2/c^2$ . None of the results for the differential cross section in Fig. 4.15 and Fig. 4.16 show a satisfying agreement with the NMC experiment or the generator cross sections.

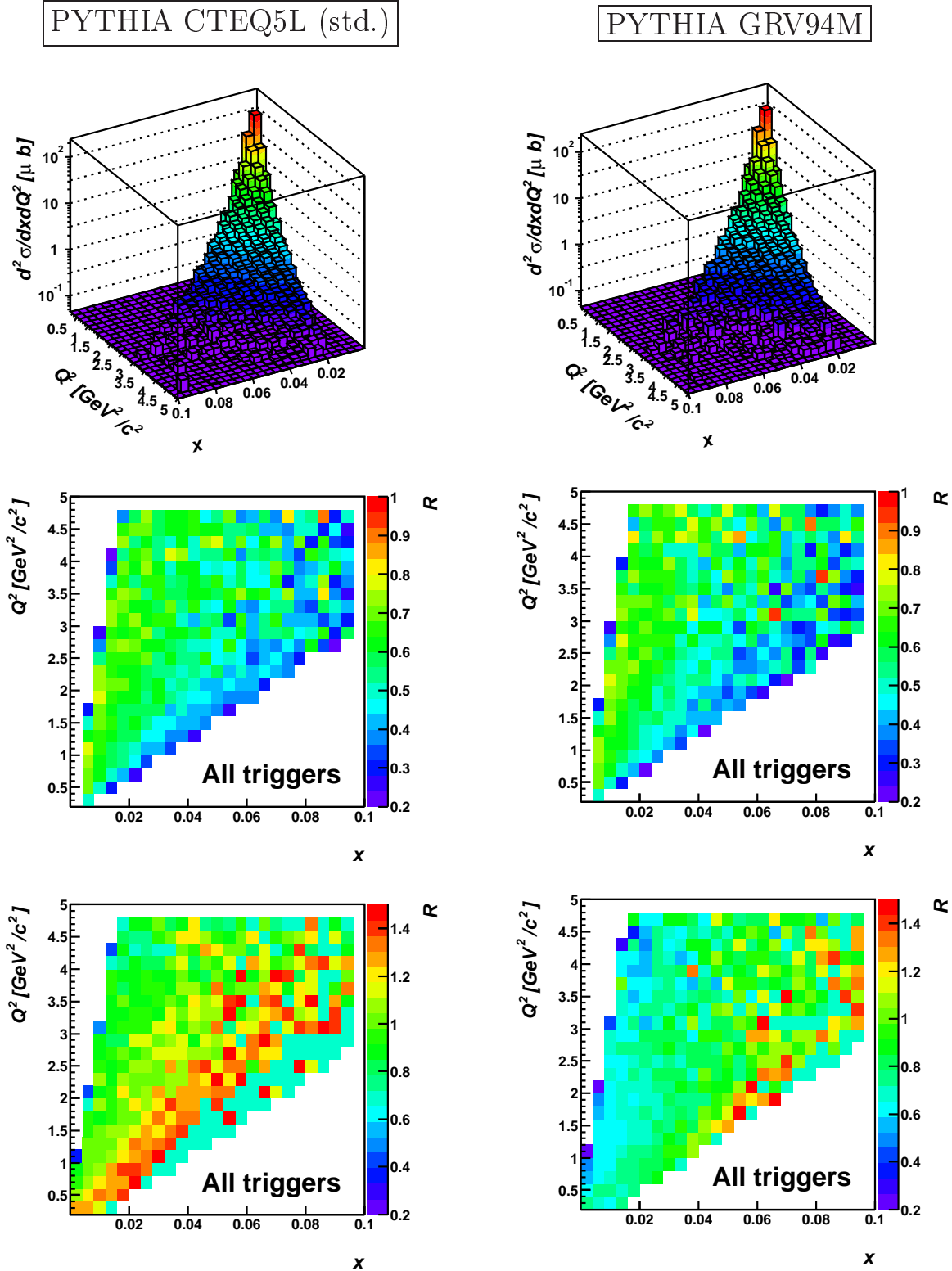


Figure 4.15: Differential cross sections (top), the ratio  $R$  of the measured cross section with the generator cross section (middle) and the ratio  $R$  of the measured cross section with the NMC measured cross section; efficiencies and cross section used from PYTHIA CTEQ5L (left) and PYTHIA GRV94M (right)

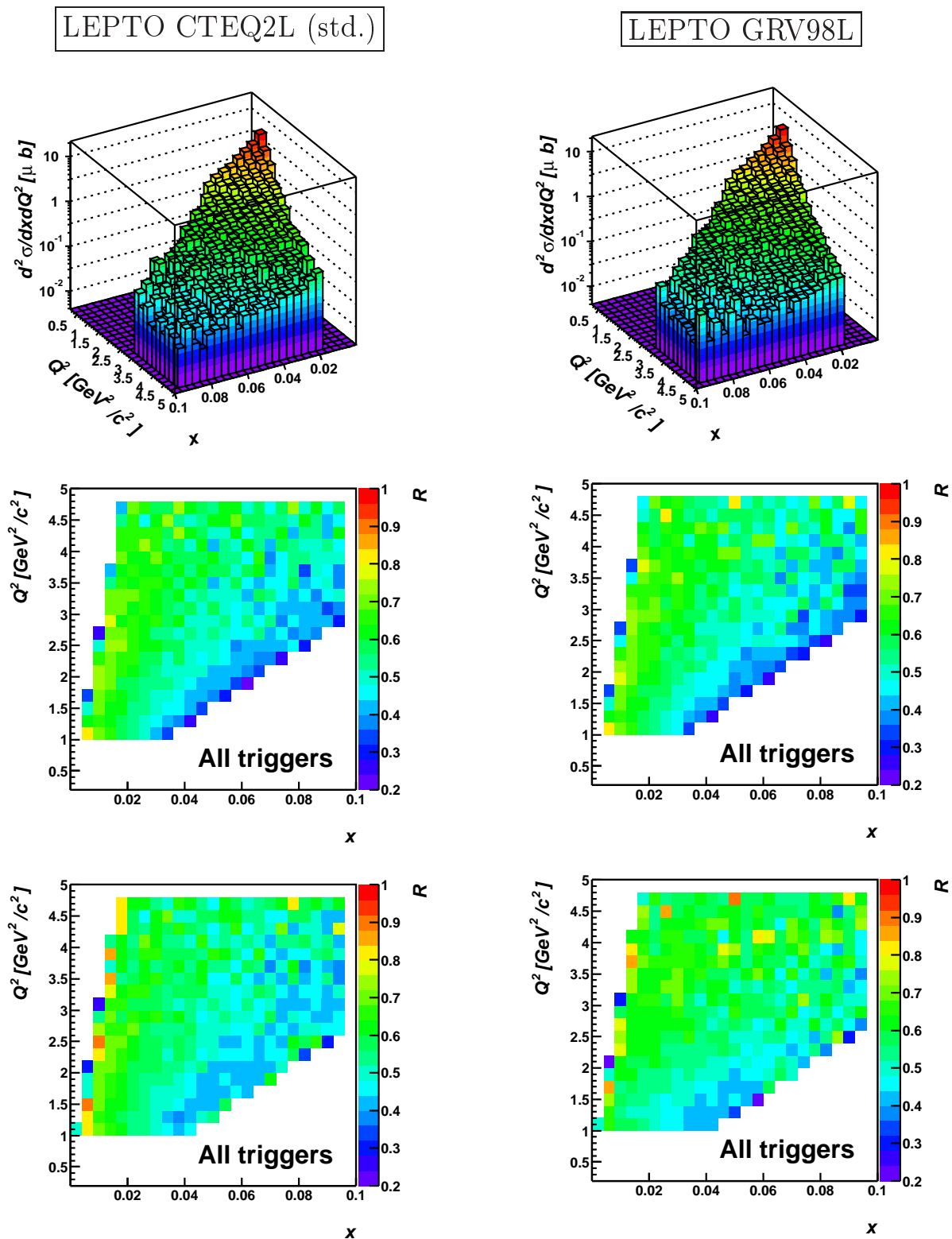


Figure 4.16: Differential cross sections (top), the ratio  $R$  of the measured cross section with the generator cross section (middle) and the ratio  $R$  of the measured cross section with the NMC measured cross section; efficiencies and cross section used from LEPTO CTEQ2L (left) and LEPTO GRV98L (right)

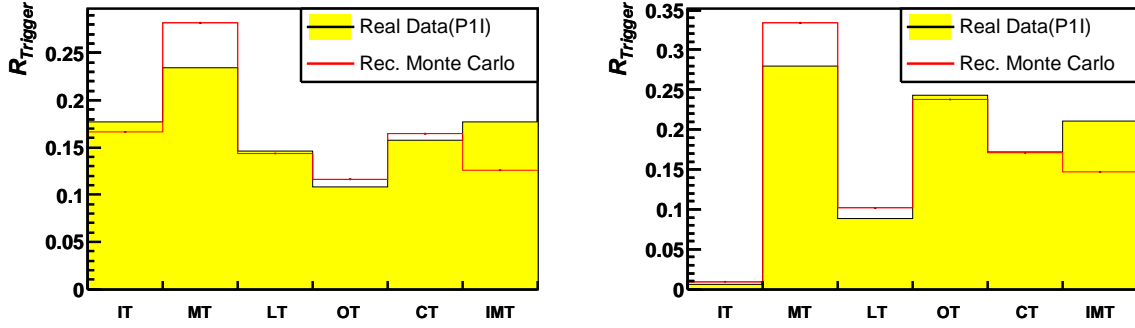


Figure 4.17: Fraction of events which contain different triggers in real data compared to PYTHIA (left) and LEPTO (right) with standard settings

### 4.4.3 Trigger Dependent Analysis

To find an answer to the question, why the measured cross section is smaller than the NMC cross section, one can look at the different triggers. It is known, that the triggers are not perfectly simulated in the Monte Carlo.

This is evident in Fig. 4.17, where the trigger distributions in the real data and the Monte Carlo data are compared. The ratio  $R^i$  of the number of events which include the trigger  $i$  divided by the number of all events is shown for all physics triggers:

$$R^i = \frac{N_{\text{Events}}^i}{N_{\text{Events}}^{\text{All}}} \quad (4.28)$$

$$i \in \{\text{InnerTrigger(IT), MiddleTrigger(MT),}$$

$$\text{LadderTrigger(LT), OuterTrigger(OT),}$$

$$\text{CalorimeterTrigger(CT), InclusiveMiddleTrigger(IMT)}\}$$

The comparison of the real data with the PYTHIA standard Monte Carlo is shown on the left and the LEPTO defaults are shown on the right. Certainly, the differences in the trigger distribution cannot be caused by the use of the different generators but are a result of the restriction to different kinematical regions. The first thing to notice is, that there are nearly no Inner Trigger events for the LEPTO Monte Carlo. This is no surprise, as the Inner Trigger is mainly sensitive to events with  $Q^2 < 0.5 \text{ GeV}^2/c^2$ . Real data and Monte Carlo data are cut on  $Q^2 > 1 \text{ GeV}^2/c^2$  in the LEPTO case.

The number of events including the Middle Trigger are obviously overestimated for both generators, whereas the number of inclusive Middle Trigger events is underestimated. That points to a bad description of the Calorimeter Trigger in the Monte Carlo, as the only difference between the Middle and the inclusive Middle Trigger is, that for the inclusive Middle Trigger no energy deposit in the calorimeter is needed.



The threshold for this energy is smaller than for the stand-alone Calorimeter Trigger (CT).

For PYTHIA we see indeed a slight overestimation of the stand-alone Calorimeter Trigger, whereas for LEPTO the Monte Carlo data shows a good agreement with the real data. One could assume that only the thresholds for the Calorimeter Trigger used by the the other triggers are not correctly set.

In principle, the overestimation of the number of events in the reconstructed data leads to a overestimation of the detector efficiency (see Eq. 4.17) and thus to a underestimation of the differential cross section. This means we would expect higher values for the cross section for events where the inclusive Middle Trigger fired. This effect would cause a lower cross section for the Middle Trigger with the additional calorimeter threshold.

The efficiencies for the Middle, Ladder, Outer and inclusive Middle Trigger, obtained with the LEPTO standard parameters, are shown in the Fig 4.18. As the NMC cross section is best described by this Monte Carlo data set, it will be solely used here. For the efficiencies of all other settings see App. A.2.

The efficiencies for the Middle Trigger are about 0.5 for  $Q^2 < 3 \text{ GeV}^2/c^2$ , whereas the Inclusive Middle Trigger only shows efficiencies of about 0.25 in the same region. As expected, the Outer Trigger shows higher efficiencies of about 0.5 for larger values of  $Q^2$ . The Ladder Trigger's efficiencies are about 0.05 to 0.15 as it is at the edge of it's acceptance region for  $Q^2 > 1 \text{ GeV}^2/c^2$ . The Inner Trigger is not sensitive for  $Q^2 > 1 \text{ GeV}^2/c^2$ , and it is left out here.

The ratios of the cross sections, calculated with the efficiencies in Fig. 4.18 and Eq. 4.10, divided by the internal generator cross section are shown in Fig 4.19. For the Inclusive Middle Trigger we have ratios up to one, whereas the cross section for Middle Trigger events is only 0.7 times the generator cross section and less. Looking at the efficiencies for the two triggers this is no surprise. Following this argumentation, one could say, that the true measured cross section is given by the Outer Trigger, because the ratio of Outer Trigger events is fairly good reproduced in the Monte Carlo (see Fig. 4.17). The differential cross section obtained with Outer Trigger events is a factor  $\approx 0.6$  smaller than the LEPTO generator cross section.

Another effect can be observed in Fig. 4.19. The cross section ratios obtained with events from the Outer and Inclusive Middle Trigger are flat. In contrast, they drop for the Ladder and Middle Trigger for the lower right part, i.e. for smaller values of  $y$ . Again this points to a problem with the Calorimeter Trigger, which is included in the Middle and Ladder but not in the Outer and Inclusive Middle Trigger.

One can avoid the problems with the calorimeter by selecting only events from a specific trigger where the calorimeter is not included, e.g. the Inclusive Middle Trigger. A comparison of the inclusive cross sections determined with COMPASS

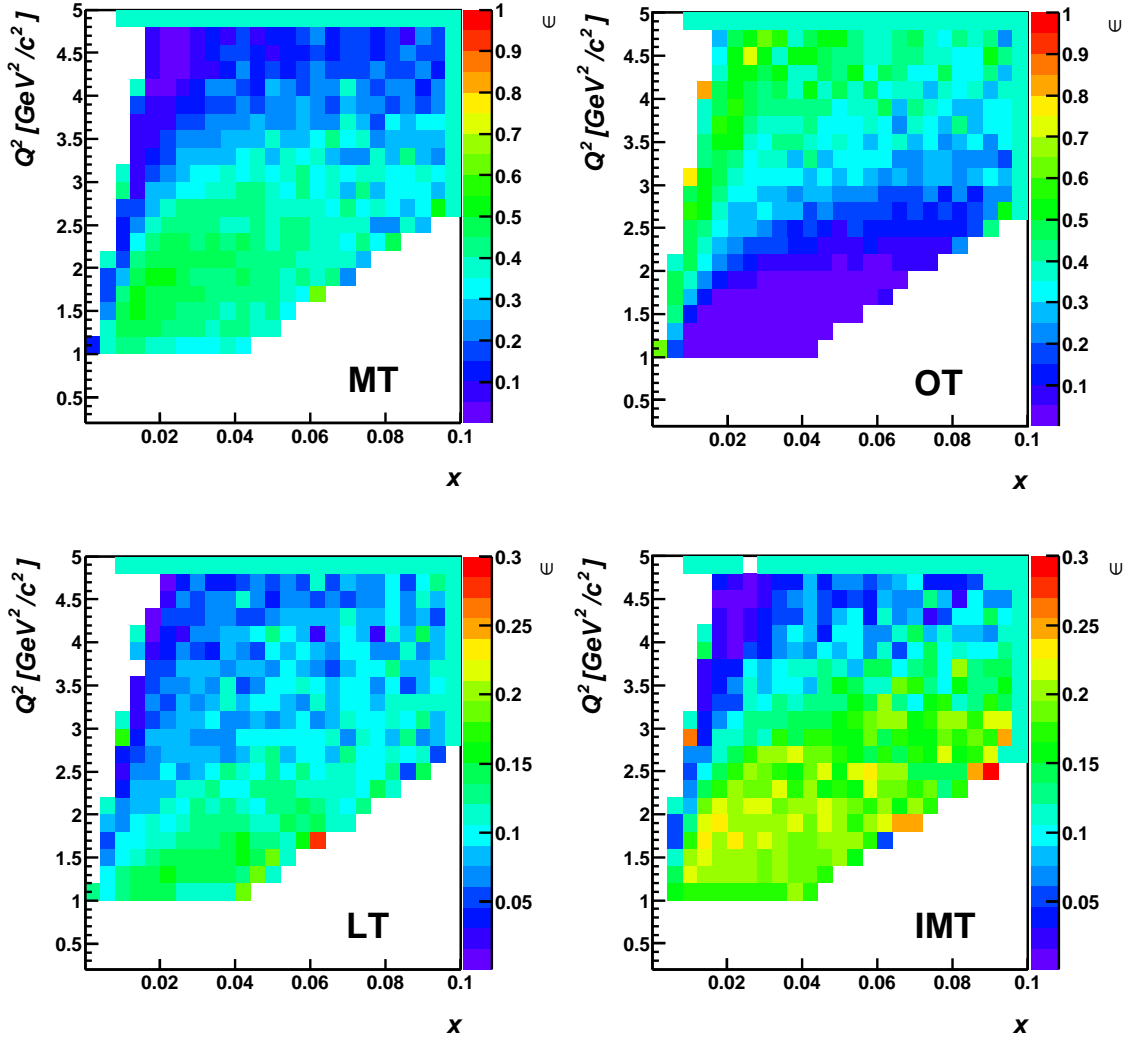


Figure 4.18: Efficiencies determined with LEPTO (std) for different triggers: Middle Trigger (top left), Ladder Trigger (bottom left), Outer Trigger (top right) and Inclusive Middle Trigger (bottom right)

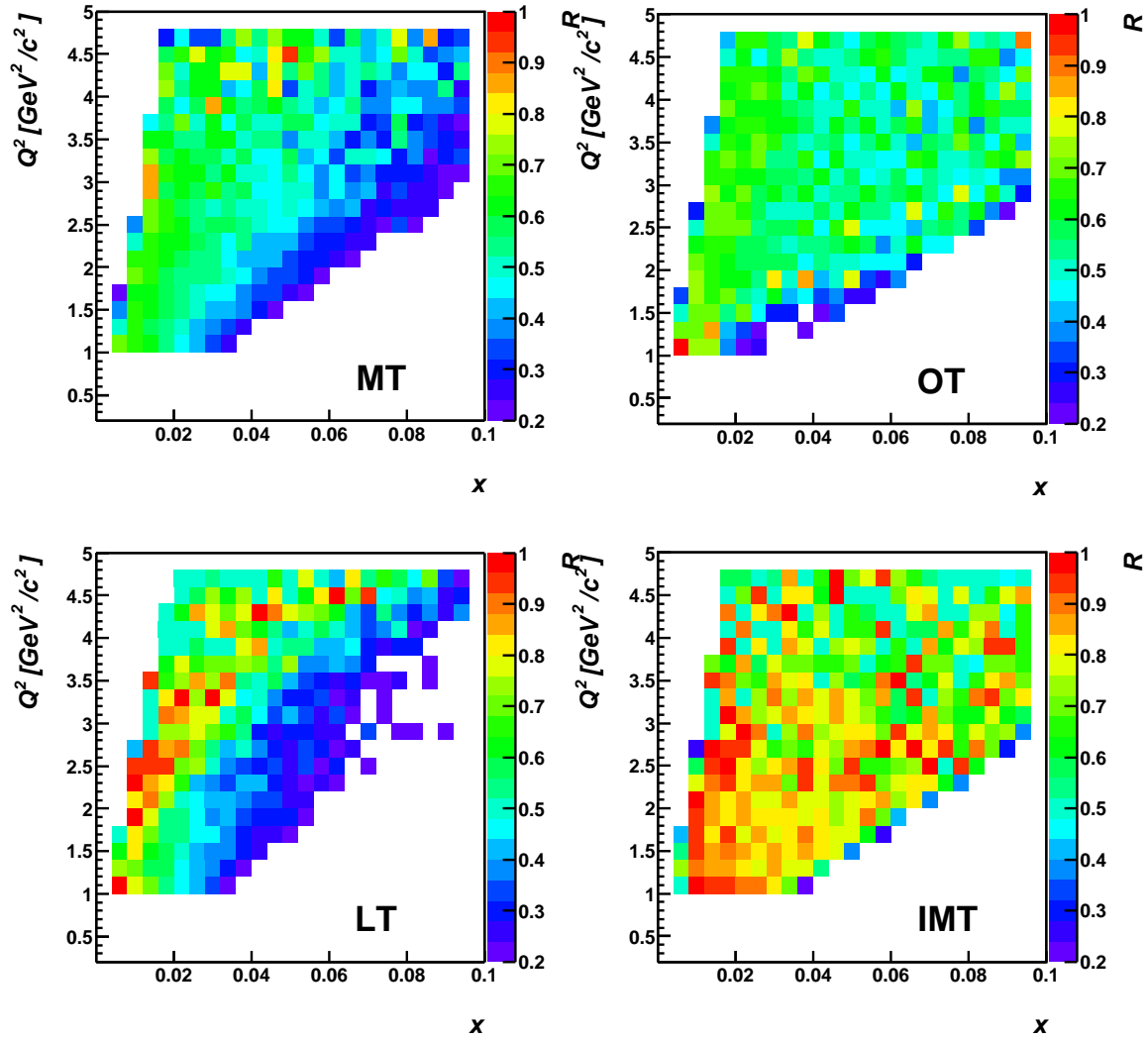


Figure 4.19: Ratios of the Cross Section determined with LEPTO (std) efficiencies divided by the NMC Cross Sections for different triggers: Middle Trigger (top left), Ladder Trigger (bottom left), Outer Trigger (top right) and Inclusive Middle Trigger (bottom right)

data and the NMC result is shown in Fig. 4.20<sup>4</sup>. Only events which are triggered by the Inclusive Middle Trigger are used. In the top row of Fig. 4.20 three bins in  $Q^2$  were chosen and integrated to calculate  $d\sigma/dx$ . The borders of the integration may depend on  $x$  due to the restrictions of  $0.1 < y < 0.9$  (see Eq. 4.11). Efficiencies from PYTHIA (std.) are used on the left side and LEPTO (std.) on the right side of Fig. 4.20. A good agreement is observed for  $Q^2 < 1.0 \text{ GeV}^2/c^2$  where  $x > 0.005$  and the intermediate range  $1.0 \text{ GeV}^2/c^2 < Q^2 < 3.5 \text{ GeV}^2/c^2$  for both generator settings. The values measured at COMPASS are larger than the NMC results for the highest  $Q^2$  bin.

Equally, three intervals of  $x$  were chosen to determine  $d\sigma/dQ^2$  (bottom row of Fig. 4.20). A good agreement is obtained with the PYTHIA Monte Carlo for a wide range in  $Q^2$  for the smallest and largest values of  $x$ . The cross section measured by COMPASS for the intermediate  $x$  region is smaller than the result of the NMC collaboration. This does not change if one uses the LEPTO generator. In addition a significant drop of the cross section for large values of  $Q^2$  can be observed in the lowest  $x$  bin using LEPTO generated data.

---

<sup>4</sup>The results for all triggers can be found in Fig. A.6 and Fig. A.7

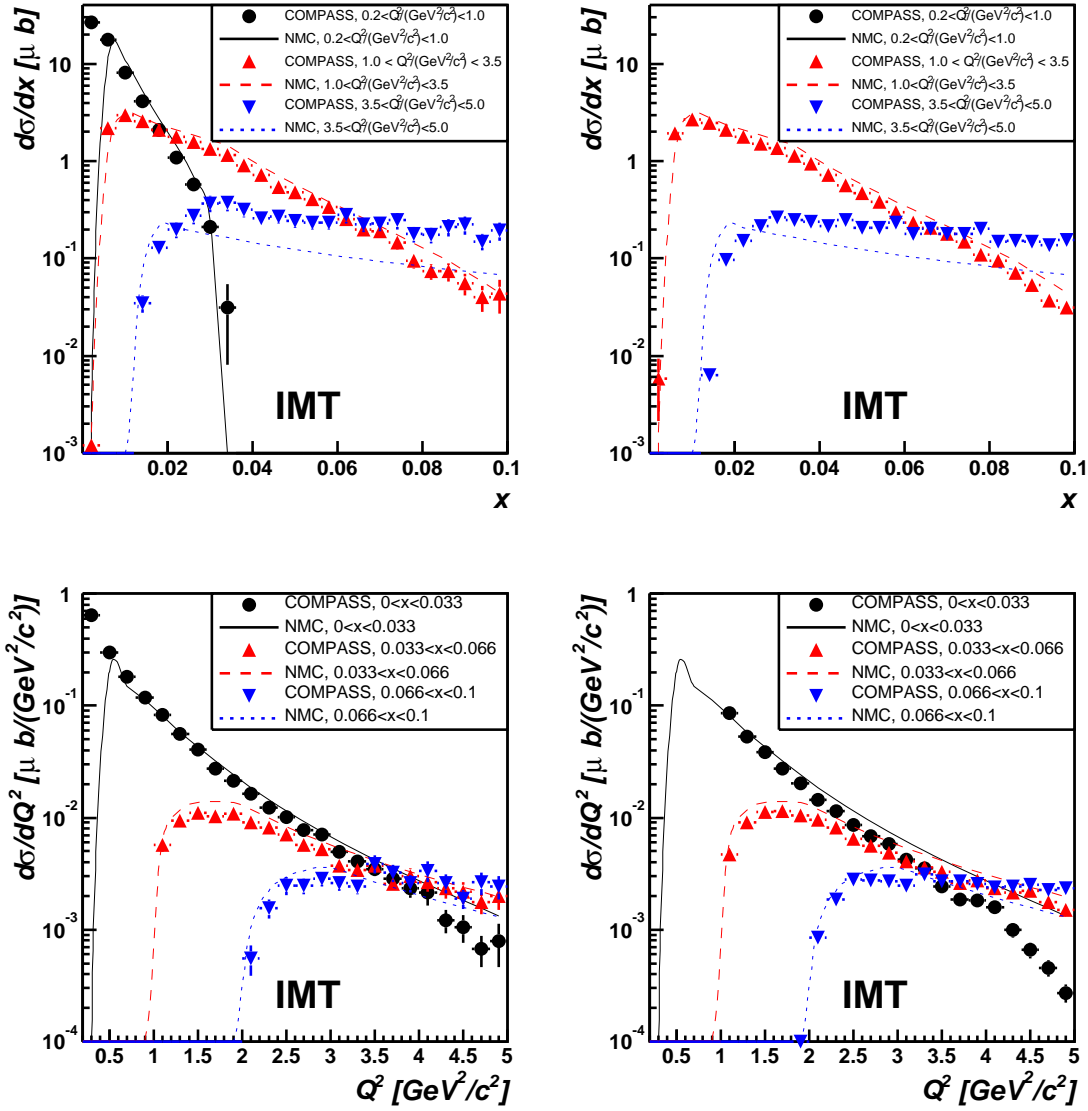


Figure 4.20: COMPASS results for  $\frac{d\sigma}{dx}$  (top) and  $\frac{d\sigma}{dQ^2}$  (bottom) obtained with efficiencies from PYTHIA (left) and LEPTO (right) in comparison to the NMC results; only Inclusive Middle Trigger events are considered; different bins in  $x$  and  $Q^2$  are shown; standard parameters in the Monte Carlo generation were used for the determination of the efficiencies



# Chapter 5

## Semi-Inclusive Single High- $p_t$ Hadron Analysis

The polarised gluon distribution of the nucleon can be studied by analysing photon-gluon-fusion (PGF) events. These are enhanced in the data sample by selecting events where a hadron with high transverse momentum high- $p_t$  with respect to the virtual photon is detected in the final state.

In this analysis events containing hadrons with a transverse momentum  $p_t > 1\text{GeV}/c^2$  are considered. A first step on the way of determining  $\frac{\Delta G}{G}$  is done here by calculating the double spin asymmetries in these single hadron high- $p_t$  events.

In addition to the calculation of these asymmetries, the differential cross section for the production of high- $p_t$  hadrons is determined and compared to theoretical calculations (see [36]).

### 5.1 Event and Data Selection

In chapter 4.2 the event selection criteria for the inclusive analysis have been shown. Additional cuts for the hadrons are applied in the semi-inclusive analysis. For the semi-inclusive analysis, all 2002 and 2003 data are used. Again, the runs are selected according to the run list of the data quality page [32] and reduced by the bad spill lists. For a good event we demand:

- one and only one primary vertex inside the inclined target
- one and only one scattered muon with an associated hit in the last trigger hodoscope
- the extrapolated beam track must cross the whole target

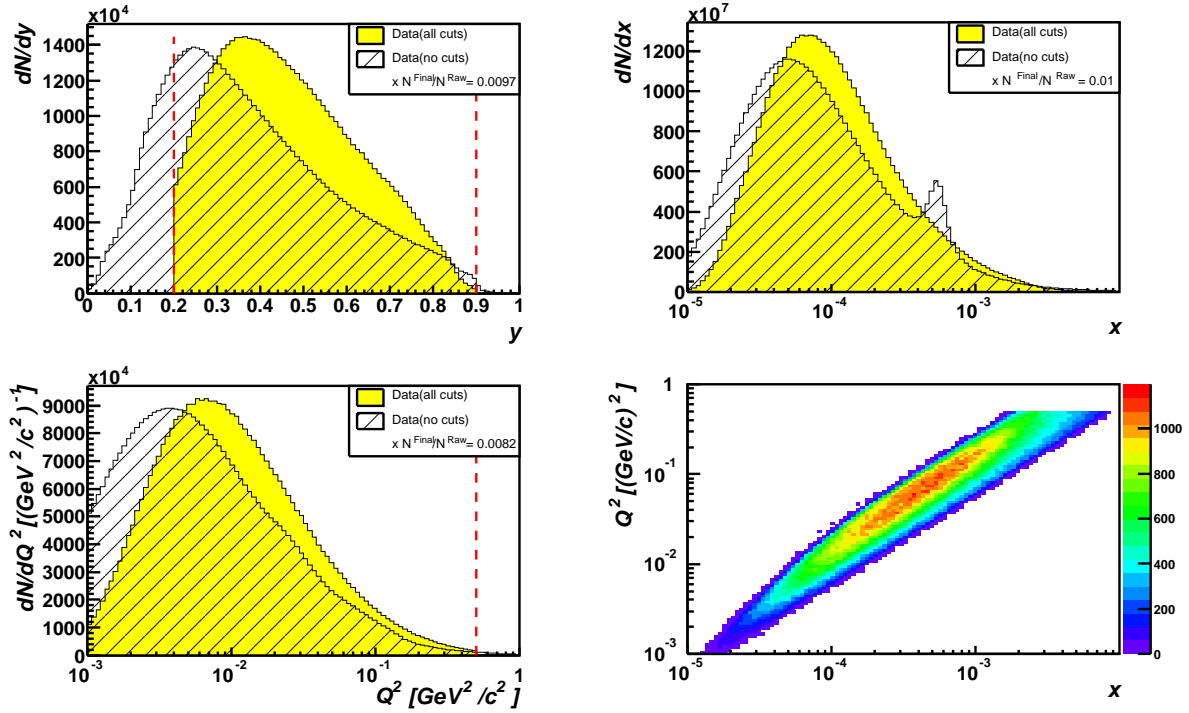


Figure 5.1: Distribution of the inclusive variables in semi-inclusive events; left column:  $y$  (top),  $Q^2$  (bottom); right column:  $x$  (top),  $Q^2$  versus  $x$  (bottom); again the peak of the elastic muon electron scattering can be seen in the raw distribution of  $x$ ; the raw data is scaled by a factor  $f = \frac{N^{\text{Final}}}{N^{\text{Raw}}}$

For the target cuts, positions and a more detailed description of the selection criteria see chapter 4.2.2.

In addition to this cut we demand **at least one reconstructed hadron in the final state**. The restrictions to the hadrons will be shown and explained in the chapter 5.1.2.

### 5.1.1 Kinematic Cuts

The cuts on the inclusive kinematical variables  $x$ ,  $y$  and  $Q^2$  are different from the cuts in the inclusive analysis. They have been adapted to the theoretical calculations in [36].

- no cut on  $x$
- $0.2 < y < 0.9$



- $Q^2 < 0.5 \text{ GeV}^2/c^2$

As the theoretical calculations are based on the Weizsäcker-Williams technique, it is crucial to restrict the events to photoproduction, i.e. we have a quasi-real photon with small  $Q^2$ .

The distributions of the inclusive kinematical variables can be seen in Fig. 5.1. At least one detected hadron is requested fulfilling the demands introduced in the next section.

Note that due to the cut on  $Q^2$ , the  $x$  range is shifted to much lower values with respect to the inclusive case. Only a second particle besides the scattered muon in the primary vertex is requested for the raw distributions. The raw distributions are scaled by a factor  $f = \frac{N^{\text{Final}}}{N^{\text{Raw}}}$  where only entries in the visible bin range are considered.

### 5.1.2 Hadron Selection

As we are now looking at semi-inclusive scattering events, it is inevitable to specify the requirements for the hadron sample. First of all, we can check if a proper tracking for the hadron was possible. Track reconstruction based only on information from detectors situated before the first spectrometer magnet is poor. Therefore, tracks with their last measured point in or in front of SM1 are rejected. Additionally, if the last measured point is located behind the second muon wall, there is a high probability for the particle to be a falsely identified muon. This means for the  $z$  component of the last measured point of each track:

- $400 \text{ cm} < z_{\text{last}} < 4000 \text{ cm}$

$z_{\text{last}}$  is the  $z$  position of the last detector hit of the hadron candidate.

Another possibility to reject muons that are identified as hadrons is to use the information of the hadronic calorimeters. For the energy of the crossing particles we have

$$\begin{aligned} p^\mu p_\mu &= \frac{E^2}{c^2} - \vec{p}^2 = m^2 c^2 \\ \Rightarrow \frac{E^2}{c^2} &= \vec{p}^2 + m^2 c^2 > \vec{p}^2 \end{aligned} \quad (5.1)$$

Muons do not deposit much energy in the hadronic calorimeter and can be removed by a cut on  $\frac{E_{\text{HCAL}}}{|\vec{p}_h|}$ . The cuts used for the two calorimeters are shown in Fig. 5.2.

- $\frac{E_{\text{HCAL1}}}{c} > 0.3 \cdot |\vec{p}_h| \vee \frac{E_{\text{HCAL2}}}{c} > 0.6 \cdot |\vec{p}_h|$
- Hadrons without energy measurement are discarded

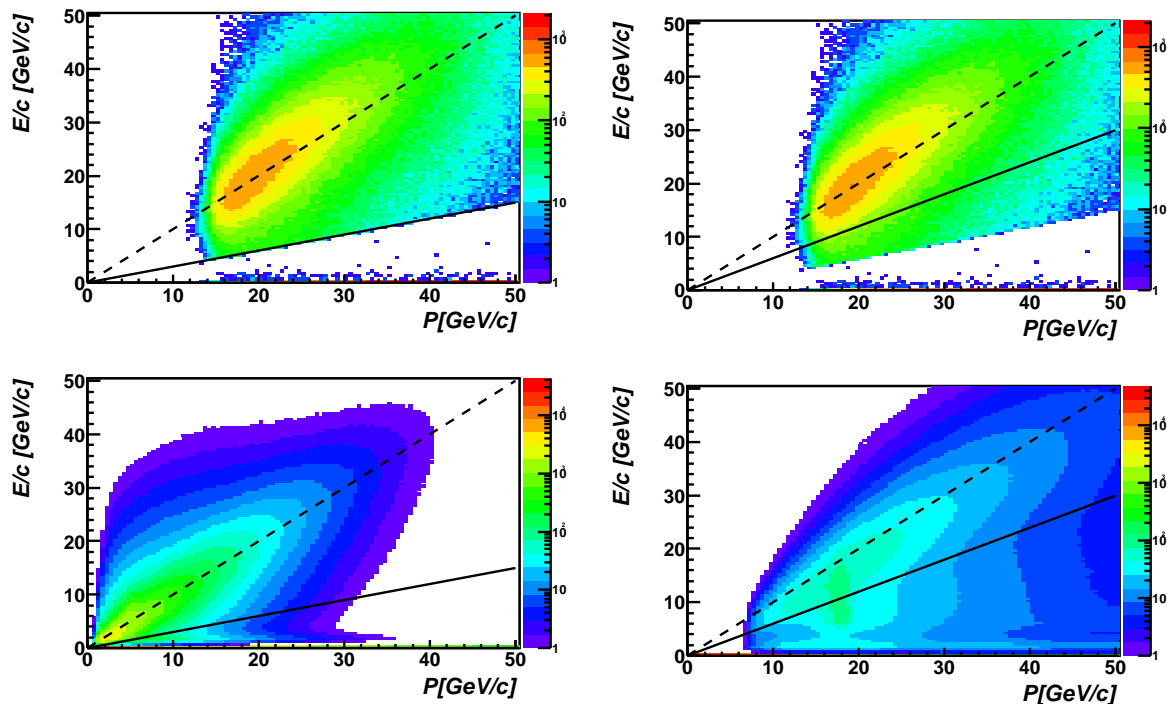


Figure 5.2: Energy versus momentum of hadron candidates in the HCAL1 (left) and the HCAL2 (right) with all cuts (upper row) and no cuts (lower row)

The different cuts arise from the accumulation of hadrons in the region  $|\vec{p}_h| \approx 18 \frac{\text{GeV}}{c}$ , whose origin is unknown and are therefore be cut away. The upper part vanishes with the application of the other cuts on the hadron. The lower part is eliminated by this cut.

The energy measurement of the hadronic calorimeter was corrected for the 2002 data, as they were not calibrated correctly. The values used in the analysis are:

- $E_{\text{HCAL1}} = \frac{E_{\text{HCAL1}}^0}{1.3}$
- $E_{\text{HCAL2}} = \frac{E_{\text{HCAL2}}^0}{1.24}$

Then we can look at the semi-inclusive variables<sup>1</sup>  $x_F$ , the longitudinal momentum fraction of the hadron with respect to the photon, and  $z$ , the fraction of the photon energy carried by the hadron. Both magnitudes are helpful to pick out hadrons from the current fragmentation region. Hadrons from the current fragmentation region, in contrast to the target fragmentation region, contain the struck parton or daughter particles of the latter. They carry a high momentum and energy fraction. As we are only interested in current fragmentation hadrons, a cut is applied on both quantities:

---

<sup>1</sup>see Tab. 2.2

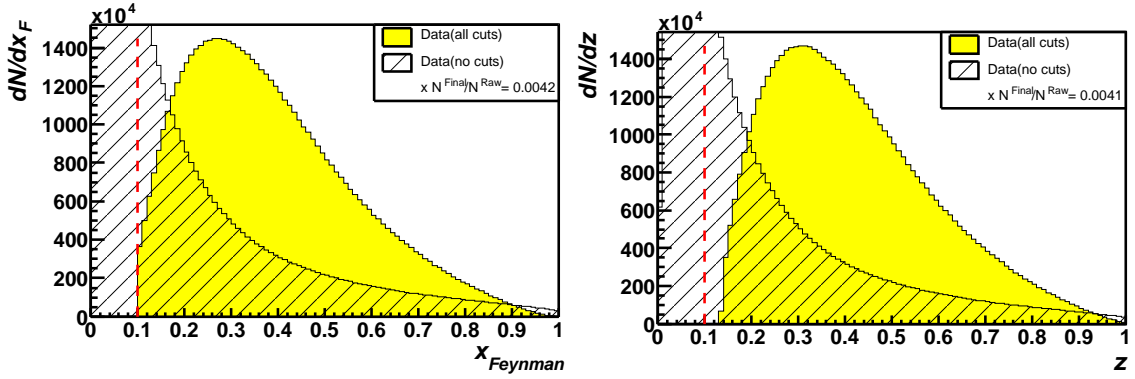


Figure 5.3:  $x_F$  (left) and  $z$  (right) distribution of the hadrons with all and without cuts; the raw data is scaled by a factor  $f = \frac{N^{\text{Final}}}{N^{\text{Raw}}}$

- $x_F > 0.1$
- $z > 0.1$

The corresponding distributions are shown in Fig. 5.3. Only a primary vertex, a scattered muon and at least one hadron is requested for the raw sample.

The opening of the target restricts the acceptance for the opening angle of hadrons originating at the beginning of the target to  $\Theta_h < 70$  mrad. All hadrons scattering to a larger angle are therefore discarded (see Fig. 5.4).

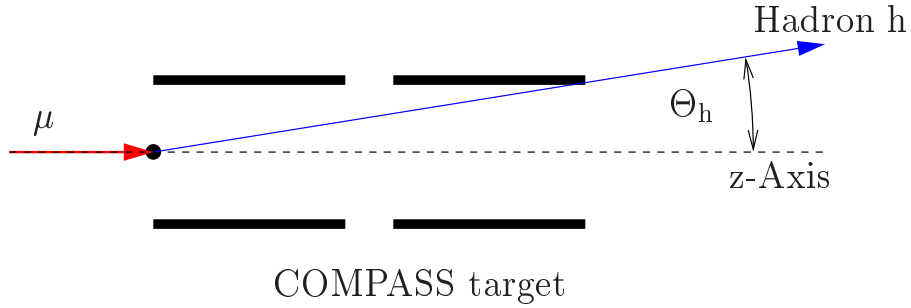


Figure 5.4: Angular acceptance of the target

Last but not least, the cut on the transverse momentum  $p_t$  of the hadron with respect to the virtual photon's momentum is done:

- $p_t > 1 \frac{\text{GeV}}{c}$

The  $p_t$  distribution of the final hadron sample can be seen in Fig. 5.5.

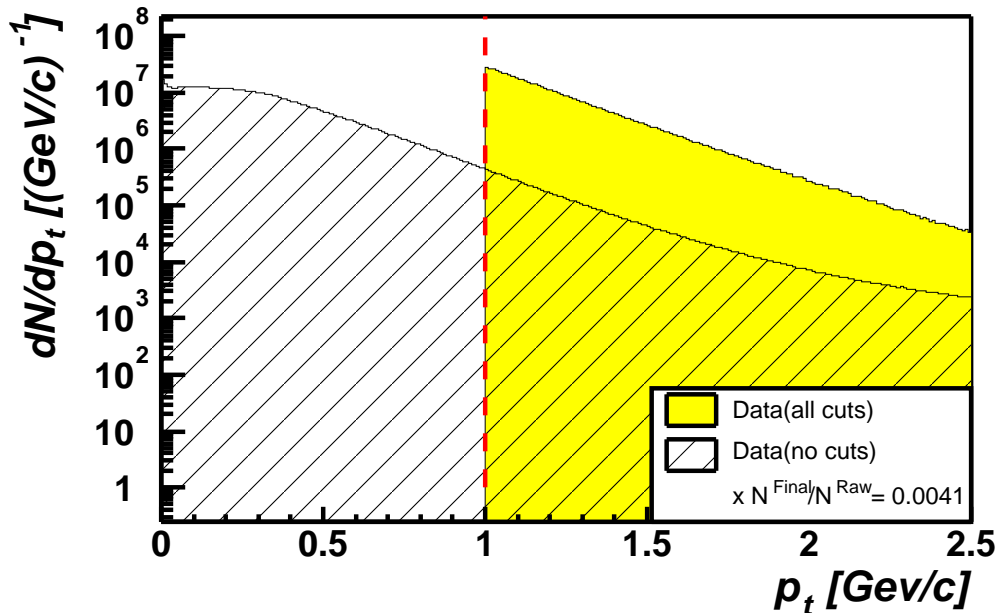


Figure 5.5:  $p_t$  distribution of final and raw data sample

From the comparison with the raw sample, it is obvious that the  $p_t$  cut alone already reduces the number of hadron candidates drastically. The number of good hadrons in the primary vertex, i.e. the multiplicity, is reduced from about 2.3 in the raw data sample to one in the final sample (see Fig. 5.6).

### 5.1.3 Hadron Identification with the RICH

In Chapter 5.1 all charged hadrons were considered. But it is also possible to identify the type of the hadron with the RICH detector (see chap. 3.4.4). In principle protons, kaons and pions can be identified, provided that their momentum is above the threshold for Čerenkov light emission. There are two methods of particle identification, namely the ‘**Log-Likelihood-Method**’ (LLH) and the ‘ $\chi^2$ -Method’. For the ‘ $\chi^2$ -Method’ the ring of Čerenkov-photons reflected to the photon detectors at the front side of the RICH detector is fitted and the emitting angle  $\Theta^{photon}$  of the photons with respect to hadrons momentum direction is calculated. One can assume the hadron to be a proton, pion or kaon and assign the mass of the particle to the track. The angle of the Čerenkov-cone  $\Theta_{id}^{cone}$  for each assumption can then

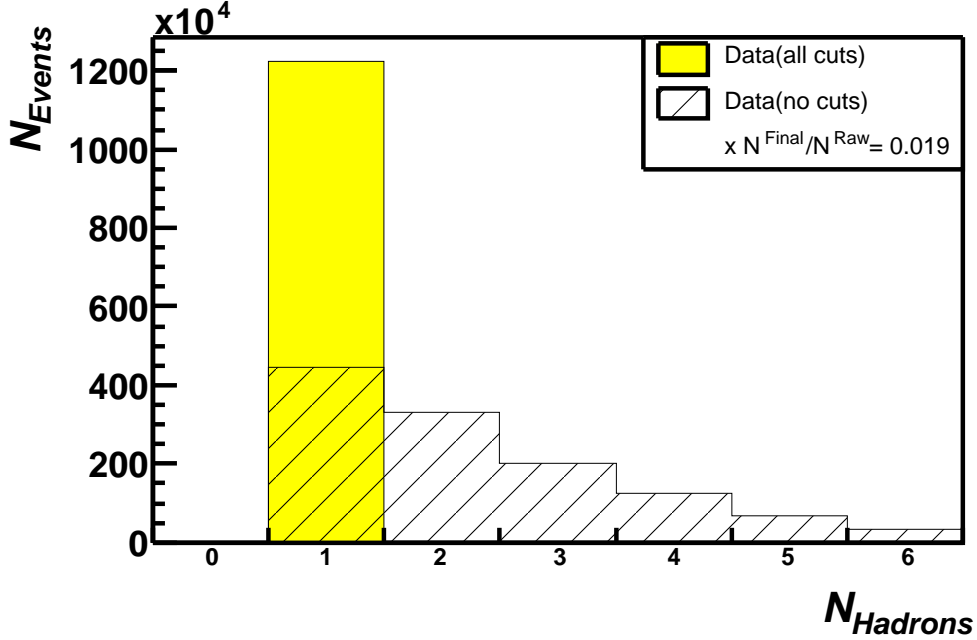


Figure 5.6: The hadron multiplicity in the primary vertex

be calculated. The  $\chi^2$  for each particle hypothesis is defined as:

$$\chi_{id}^2 = \sum^{\text{Photons}} \frac{(\Theta_{\text{rec},k}^{\text{photon}} - \Theta_{id}^{\text{ring}})^2}{(\sigma_{\Theta}^{\text{photon}})^2} \quad (5.2)$$

$\sigma_{\Theta}^{\text{photon}}$  is one standard deviation in of the resolution in the angle  $\Theta$  of the photon. For the identification of a particle, the hypothesis with the **minimal**  $\chi^2$  is chosen. Additionally the particle must have a momentum greater than the threshold.

The second possibility to identify the hadron is the ‘**Log-Likelihood-Method**’ (LLH). We assume the conditional probability  $P(\Theta^{\text{photon}}; \Theta_{id}^{\text{ring}})$  for a measured photon emission angle  $\Theta^{\text{photon}}$  to be known.  $\Theta_{id}^{\text{ring}}$  is the opening angle of the Čerenkov cone for a particle of type  $id$ . The likelihood is then defined as:

$$L = \prod^{\text{Photons}} P(\Theta^{\text{photon}} | \Theta_{id}^{\text{ring}}) \quad (5.3)$$

The hadron is declared to be the particle having the maximum likelihood. Again, the particle’s momentum has to be above the threshold. The difficulty of this method is that the probabilities  $P(\Theta^{\text{photon}}; \Theta_{id}^{\text{ring}})$  have to be known. This includes the knowledge of the background<sup>2</sup>.

<sup>2</sup>The actual value of  $P(\Theta^{\text{photon}}; \Theta_{id}^{\text{ring}})$  can be found in [37]

As the refractive index of the gas in the RICH was not always exactly known at the time the data was produced, one has to correct the values of  $\chi^2$  and LLH for the periods that are not yet reproduced. These are P2E, P2F and P2G of 2002 data and P1A, P1B, P1C, P1D, P1E and P1F of 2003 data. For the likelihood we have:

$$L^{corrected} = L + \frac{dL}{dn} \cdot (n^{true} - n^{prod}) \quad (5.4)$$

$n^{true}$  is the true value of the refractive index of the gas and  $n^{prod}$  the refractive index used at the production.

The correction of  $\chi^2$  is more complicated and is done by a function, provided by P. Schiavon.

The summary of the hadron identification procedure is

- Likelihood:
  - correct with true refractive index
  - particle's momentum is larger than the threshold:  $\frac{|\vec{p}|}{m_{\pi,K,P}} > \frac{1}{n_{true}}$
  - chose particle's type ( $\pi$ , K, P) with maximal likelihood
- $\chi^2$ :
  - correct with true refractive index
  - particle's momentum is larger than the threshold:  $\frac{|\vec{p}|}{m_{\pi,K,P}} > \frac{1}{n_{true}}$
  - chose particle's type ( $\pi$ , K, P) with minimal  $\frac{\chi^2}{NDF}$  and  $\frac{\chi^2}{NDF} < 4$

The fractions of the identified hadrons with the two different methods are shown in Fig. 5.7. All unidentified hadrons are included in 'Others'. For the final sample about 15% of the hadrons remain unidentified for the  $\chi^2$  method, whereas less than 1% of the hadrons with the likelihood method are not identified. For the final sample we have 68% (63%) pions, 20% (20%) kaons and 11% (4%) protons identified by likelihood ( $\chi^2$ ).

The  $p_t$  distributions of the hadrons identified with the RICH are shown in Fig. 5.8. The errors on the number of hadrons  $N$  are  $\delta_N = \sqrt{N}$ , thus the errors in the histograms are  $\delta_{dN/dp_t} = \frac{\sqrt{N}}{\text{binwidth}}$ , as the histograms are normalised to the width of the bins. Note that the identification rate for the kaons is very similar for the two methods, whereas the likelihood method identifies slightly more hadrons as pions as the  $\chi^2$  method. This difference is large in the case of proton identification.

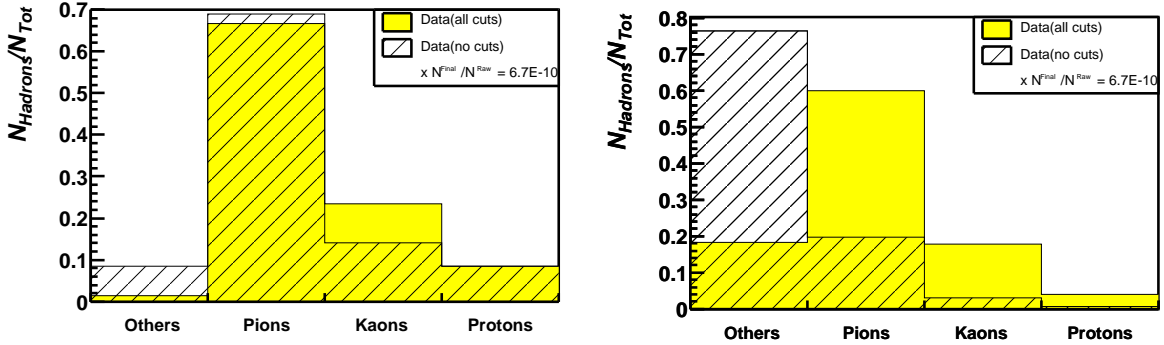


Figure 5.7: Fractions of the hadrons are identified with the RICH by LLH (left) and  $\chi^2$  (right) methods

## 5.2 Semi-Inclusive Monte Carlo

As in the inclusive analysis a Monte Carlo simulation of the data is necessary to determine the efficiencies which are needed to calculate the differential cross sections. The kinematic is now restricted to the photo-production region with  $Q^2 < 0.5 \text{ GeV}^2/c^2$ . As LEPTO is limited to  $Q^2 > 1 \text{ GeV}^2/c^2$  PYTHIA has to be used.

Again, the same cuts on the reconstructed Monte Carlo data are used as on the real data. Two different sets of Monte Carlo data are needed as we are now analysing data from 2002 and 2003. The detector setting has changed between the two years and different descriptions of the geometry of the detector for 2002 and 2003 are available. It is also important that the information provided by the RICH detector is now included in the Monte Carlo output. This is not the case for the standard Monte Carlo but needed for the determination of the efficiencies for the different hadron types. For a precise calculation of these efficiencies a very detailed study on real data would be necessary. This was not possible within the time frame of this thesis.

The Monte Carlo data is generated with the restriction  $p_t > 0.9 \text{ GeV}/c$  and then cut on  $p_t > 1.0 \text{ GeV}/c$  in the analysis to avoid smearing effects at the edges. The additional cuts introduced in chapter 5.1 are applied in the analysis.

The comparison of the inclusive variables of all 2003<sup>3</sup> data with Monte Carlo data is shown in Fig. 5.10. All kinematical distributions of the inclusive variables seem to be shifted to larger values in the Monte Carlo simulation with respect to the real data. The opposite happens for the  $x_{Feynman}$  and  $z$  distributions. They are shifted to smaller values. The momentum  $p$  and transverse momentum  $p_t$  of the hadrons are reasonably described by the Monte Carlo simulation.

<sup>3</sup>Comparisons for 2002 see B.2

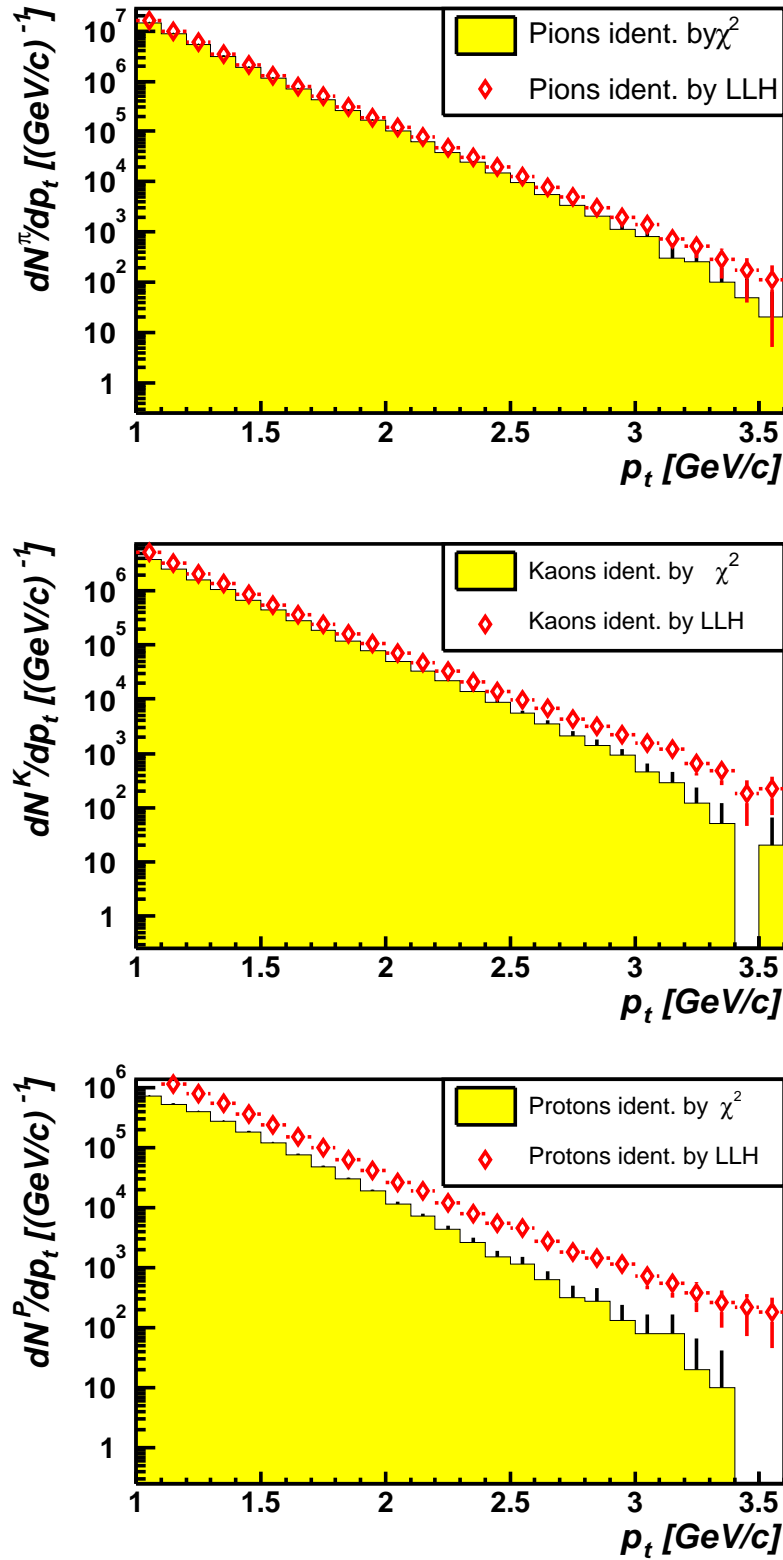


Figure 5.8: The  $p_t$  distributions of the different hadrons, identified by likelihood and  $\chi^2$  method; pions (top), kaons (middle) and protons (bottom)



Different parameter settings for the PYTHIA generator were tried but no improvement achieved. As in the inclusive case, the trigger distributions of the real data and the simulation mismatch (see Fig. 5.9). All but the Inner Trigger are underestimated. The largest overestimation is observed for the Calorimeter Trigger. A better description of the kinematical variables could be achieved by selecting one specific trigger and excluding all others. This has been done for each trigger but no improvement was observed. The comparison of the hadron identification for real data and Monte Carlo is shown in Fig. 5.12. The identification for the reconstructed Monte Carlo is done in the same way as in the real data. For the generated hadron sample the particles identified by PYTHIA are used. For the LLH method the ratio of the identified pions and protons match the data. A much larger fraction of hadrons remain unidentified in the real data ( $\approx 14\%$ ) than in the Monte Carlo ( $\approx 8\%$ ) for the  $\chi^2$  method. The number of all hadron types are therefore overestimated in the Monte Carlo.

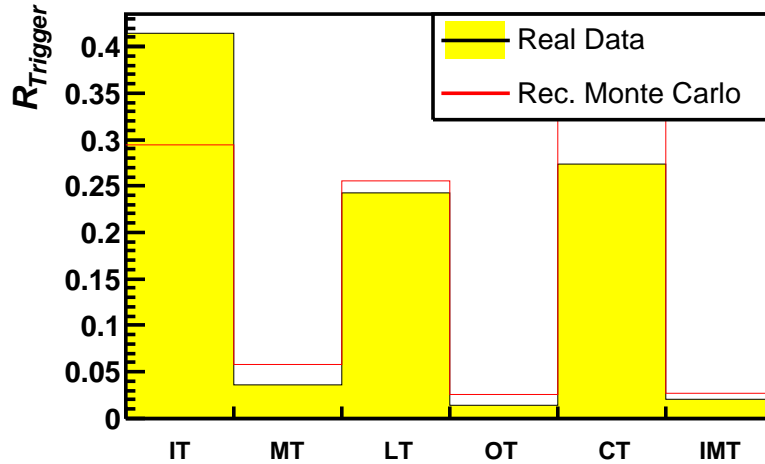


Figure 5.9: Trigger ratios in semi-inclusive events for all 2003 data and Monte Carlo data

### 5.3 Semi-Inclusive Cross Sections

The differential cross section for semi-inclusive high- $p_t$  hadron production  $\frac{d\sigma}{dp_t}$  is determined in the same way as the inclusive cross section in Chapter 4. This includes the determination of the luminosities and the efficiencies.

The luminosities are calculated in the same way as for the inclusive analysis de-

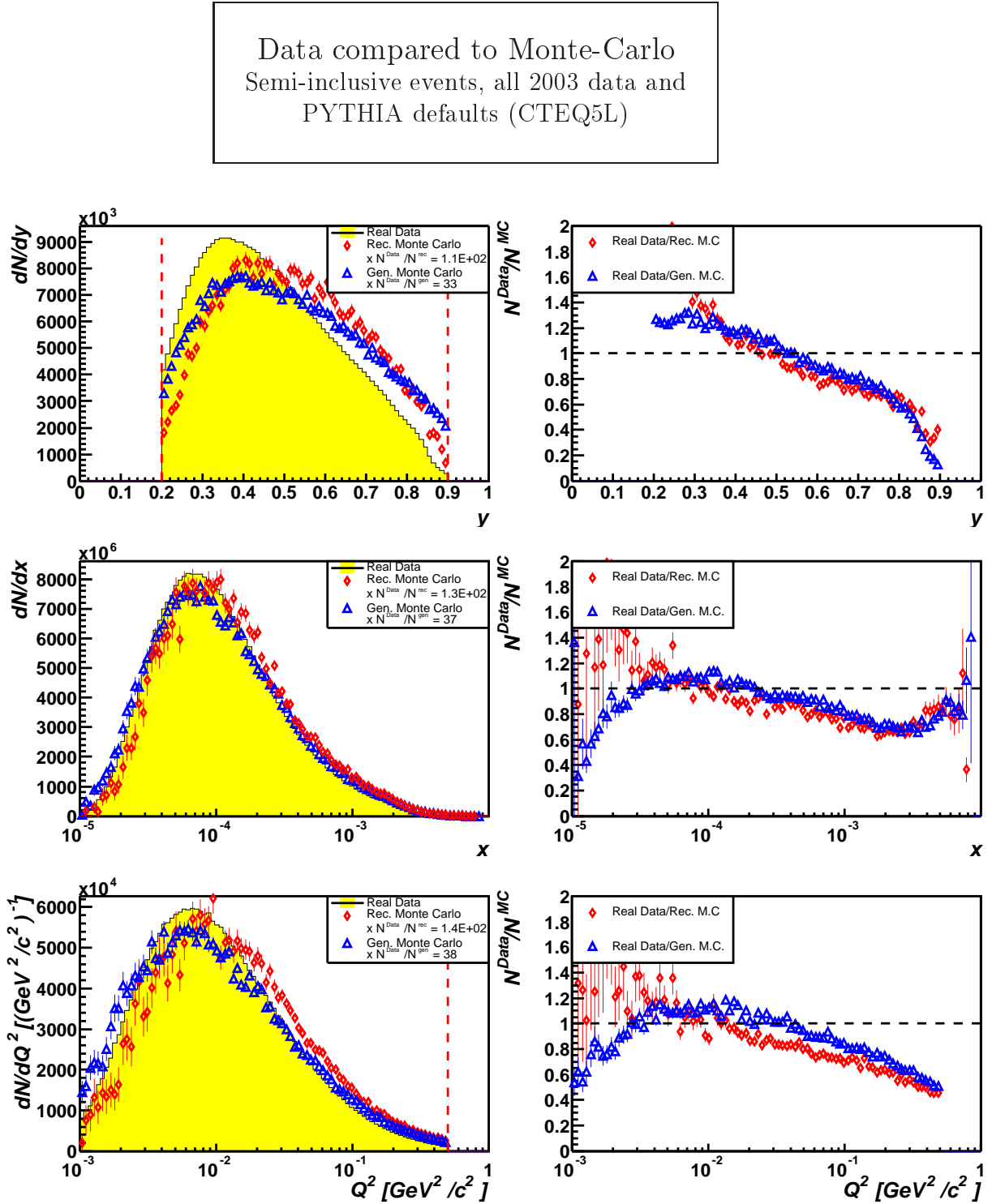


Figure 5.10: Comparison of the distributions of the inclusive variables  $y$  (top),  $x$  (middle) and  $Q^2$  (bottom) for semi-inclusive events in 2003 data with Monte Carlo; a direct comparison (left column) and the ratios of data and Monte Carlo (right column) are shown; Monte Carlo data is scaled with a factor  $f = \frac{N_{Data}}{N_{MC}}$

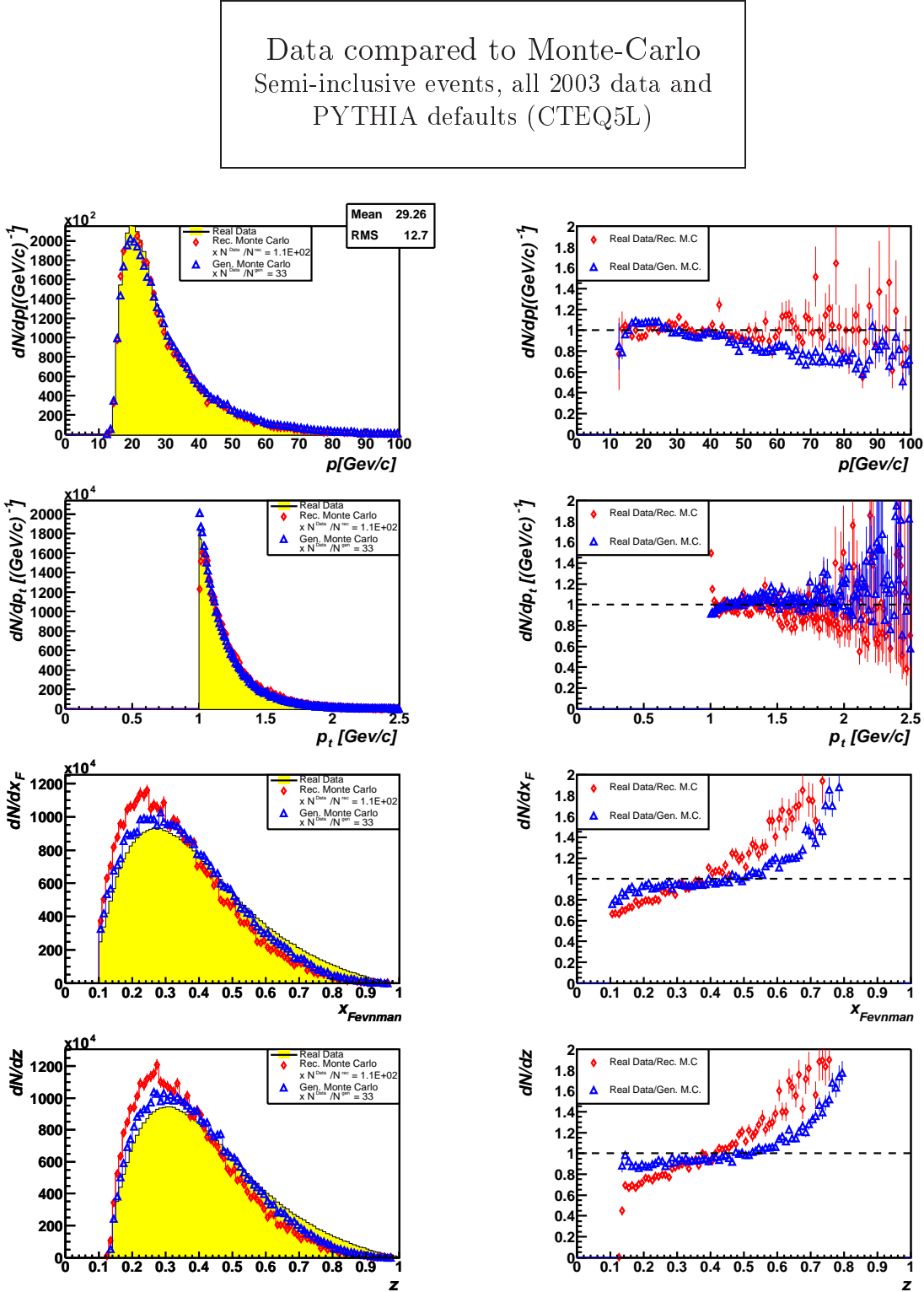


Figure 5.11: Comparison of kinematic distributions  $p$  (top),  $p_t$  (second row),  $x_{Feynman}$  (third row),  $z$  (bottom) for semi-inclusive events in real data with Monte Carlo; a direct comparison (left column) and the ratios of 2003 data and Monte Carlo (right column) are shown; Monte Carlo data is scaled with a factor  $f = \frac{N_{Data}}{N_{MC}}$

scribed in Chapter 4.4.1. The obtained results for the number of beam particles and the luminosity for each period is shown in Tab. 5.1. As we can distinguish the hadron types, it is possible to calculate the cross section not only for the production of charged hadrons in general but for  $\pi^+/\pi^-$ ,  $K^+/K^-$  and proton/antiproton production separately. The results for the two years 2002 and 2003 are shown in Fig. 5.13 and Fig. 5.14. The detector efficiencies for the different hadron types can be seen on the right. The efficiency for each hadron type  $i$  is calculated by dividing the number of generated hadrons by the number of reconstructed and identified hadrons:

$$\epsilon(p_t) = \frac{N_i^{\text{Reconstructed}}(p_t)}{N_i^{\text{Generated}}(p_t)} \quad (5.5)$$

The resulting differential cross section for single high- $p_t$  hadron production are shown in the left column. Additionally, theoretical results for leading order and next-to-leading order calculations for all charged hadrons and pions from [36] are plotted. Comparing the two identification methods, one observes a very good agreement for the pion production cross section for both years. The results for the kaons are only compatible for 2003 and not for 2002. A mismatch for the proton cross section occurs for both 2002 and 2003. Obviously the differences between the LLH and the  $\chi^2$  method in the identification efficiency for protons observed in Fig. 5.7 and Fig. 5.8 is not reflected in the Monte Carlo (see Fig. 5.12).

A comparison of the two years for the different hadron types yields a decrease in the detector efficiency for 2003. This results in an increase of the measured cross sections which are compatible with the next to leading order calculations for 2002 but not for 2003.

The decrease of the detector efficiency is in the order of 0.05. With values for the efficiency of about 0.3%-0.4% this yields a systematical error of about 10%-15%. In order to improve the accuracy of the measurement a very detailed Monte Carlo analysis is necessary. A common effort by the collaboration has started recently.

## 5.4 Asymmetries

One possible way to determine  $\frac{\Delta G}{G}$  is via the double spin asymmetry  $A_{||}$  of the photon-gluon-fusion process. A possibility to identify the PGF process is the selection of events containing high- $p_t$  hadrons. The gluon polarisation is connected to the double spin asymmetry by (see Eq. 2.33):

$$\frac{A_{||}}{D} = \langle a_{||}/D \rangle \cdot R_{\text{PGF}} \frac{\Delta G}{G} + \text{Background} \quad (5.6)$$

A first step to determine  $\frac{\Delta G}{G}$  from single high- $p_t$  hadron events will be done in this chapter by calculating the double spin asymmetry  $A_{||}/D$ .

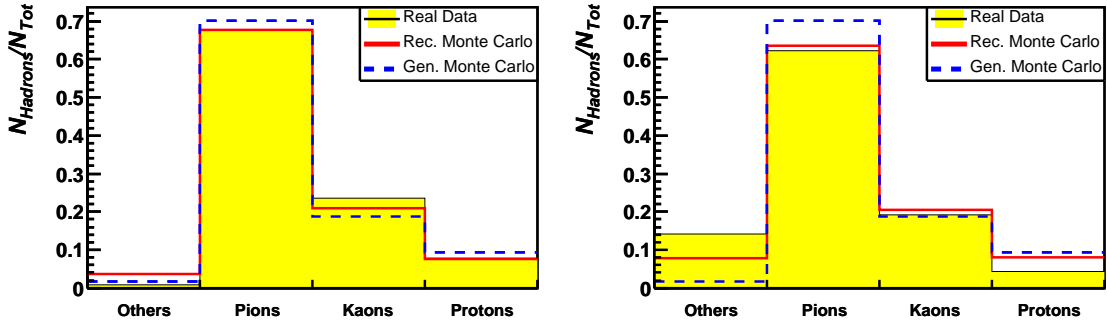


Figure 5.12: Particle identification for all 2003 data and Monte Carlo; LLH method (left) and  $\chi^2$  method (right)

Table 5.1: Number of beam particles and integrated luminosities for each period

Year	Period	Production Version	$N_{\text{Beam}}$	$\mathcal{L}$ [1/fb]
2002	P2A	2-7	$4.75108 \cdot 10^{12}$	$0.139154 \pm 0.00141994$
2002	P2D	2-6	$2.54932 \cdot 10^{12}$	$0.0746668 \pm 0.000761906$
2002	P2E	1-5	$3.30406 \cdot 10^{12}$	$0.0967723 \pm 0.000987473$
2002	P2F	1-5	$1.76413 \cdot 10^{12}$	$0.0516695 \pm 0.00052724$
2002	P2G	2-7	$2.61126 \cdot 10^{12}$	$0.0764809 \pm 0.000780417$
<b>All 2002 Periods</b>			$1.49798 \cdot 10^{12}$	$0.45307 \pm 0.00447697$
2003	P1A	1-6	$1.93144 \cdot 10^{12}$	$0.0584171 \pm 0.000577244$
2003	P1B	1-6	$1.65981 \cdot 10^{12}$	$0.0502014 \pm 0.000496061$
2003	P1C	1-6	$2.13326 \cdot 10^{12}$	$0.064521 \pm 0.000637559$
2003	P1D	1-6	$2.13177 \cdot 10^{12}$	$0.0644761 \pm 0.000637116$
2003	P1E	3-6	$3.4174 \cdot 10^{12}$	$0.10336 \pm 0.00102135$
2003	P1F	1-6	$2.67661 \cdot 10^{12}$	$0.0809548 \pm 0.000799949$
2003	P1I	3-7	$3.20445 \cdot 10^{12}$	$0.0969196 \pm 0.000957704$
2003	P1J	2-7	$5.20626 \cdot 10^{12}$	$0.157465 \pm 0.00155598$
<b>All 2003 Periods</b>			$2.2361 \cdot 10^{12}$	$0.676315 \pm 0.00668296$

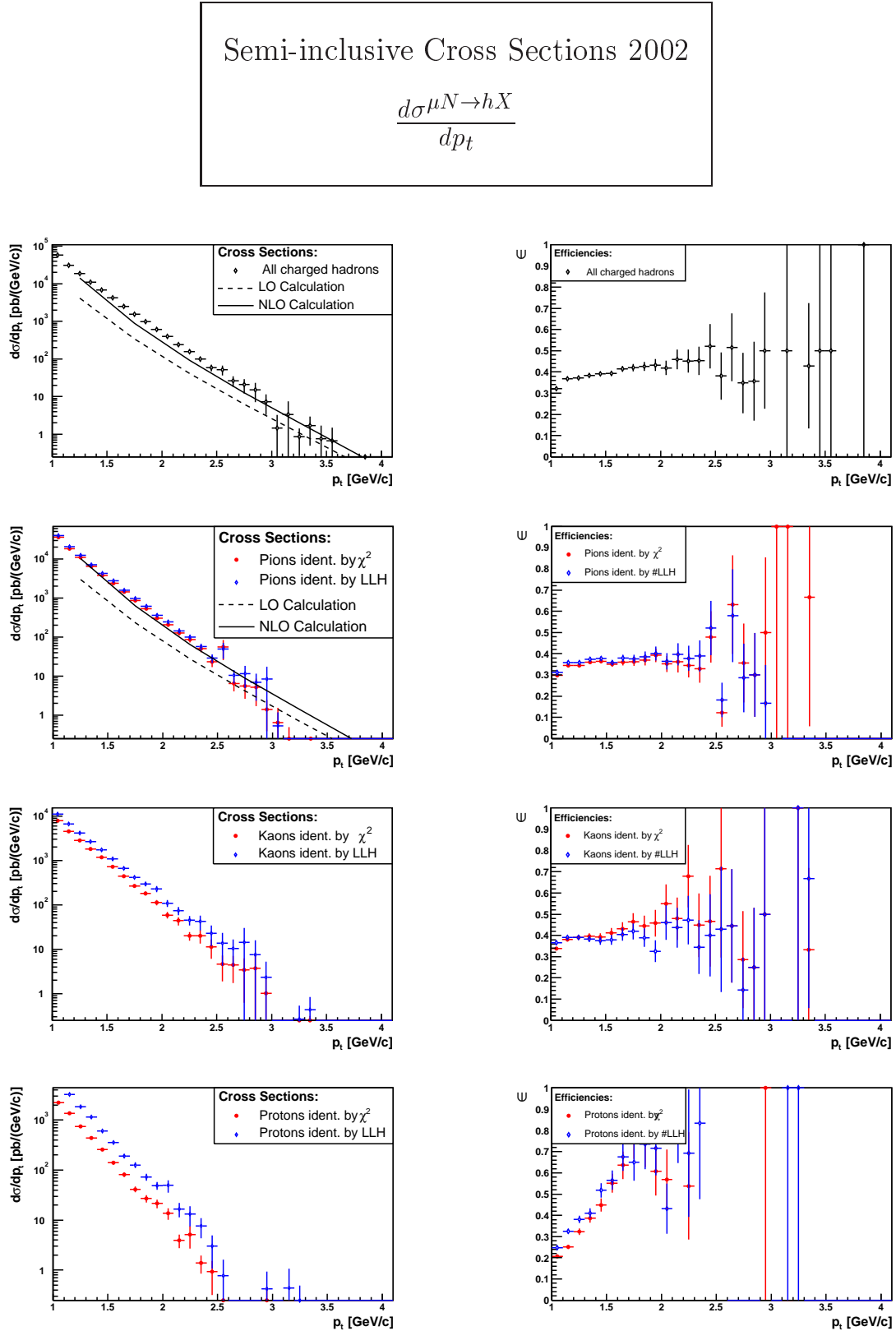


Figure 5.13: Semi-inclusive cross sections for single high- $p_t$  hadron production and efficiencies for all 2002 data; all charged hadrons (top), pions (second row), kaons (third row), protons (bottom)

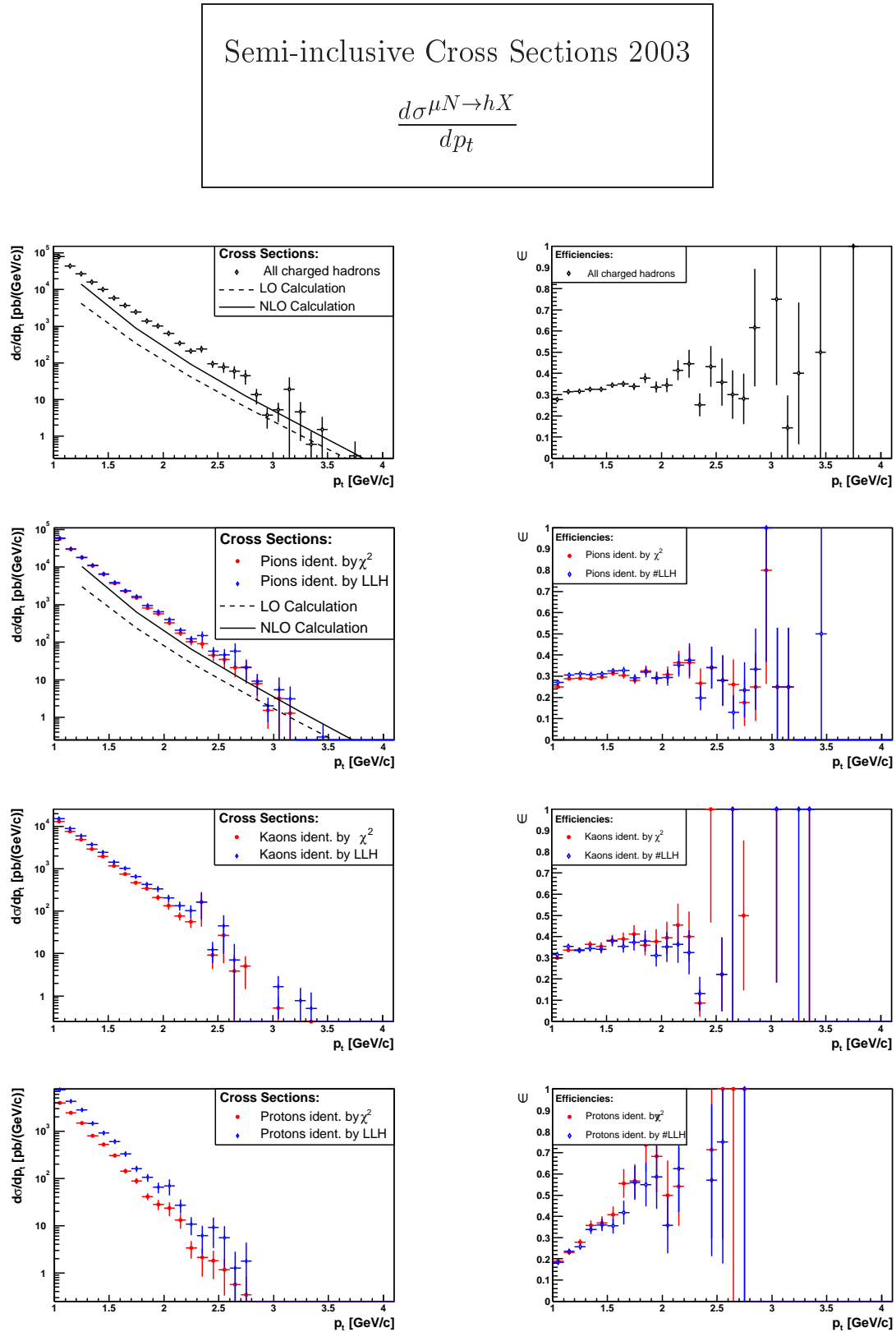


Figure 5.14: Semi-inclusive cross sections for single high- $p_t$  hadron production and efficiencies for all 2003 data; all charged hadrons (top), pions (second row), kaons (third row), protons (bottom)

Two different methods provided by [38] and [39] will be used.

### 5.4.1 Determination of the Asymmetry

The most simple way to measure the longitudinal spin Asymmetry  $A_{||}$  is to define the raw counting rate asymmetry  $A_{raw}$ :

$$A_{raw} = \frac{N^{\uparrow\downarrow} - N^{\uparrow\uparrow}}{N^{\uparrow\downarrow} + N^{\uparrow\uparrow}} \quad (5.7)$$

Here,  $N^{\uparrow\uparrow}(N^{\uparrow\downarrow})$  is the number of the hadrons that are produced in events where the muon spin is (anti-)parallel to the target spin. The fact that not all nucleons in the target are polarised is considered by the dilution factor  $f$ . The depolarisation factor  $D$  describes the partial spin transfer of the muon to the photon. The raw asymmetry is connected to the longitudinal spin asymmetry and the photon-nucleon cross section for the single high- $p_t$  hadron production  $A_{LL}^{\gamma^*N \rightarrow hX}$  via:

$$A_{||} = \frac{1}{fP_tP_b} \cdot A_{raw} \approx D \cdot A_{LL}^{\gamma^*N \rightarrow hX} \quad (5.8)$$

Here,  $P_t$  is the target polarisation and  $P_b$  the beam polarisation.

As we have two target cells with opposite polarisations, the two values  $N^{\uparrow\uparrow}$  and  $N^{\uparrow\downarrow}$  can be measured simultaneously, and can be connected to the number of hadrons produced in the upstream and downstream target cell.

$$A_{raw} = \frac{N^{\uparrow\downarrow} - N^{\uparrow\uparrow}}{N^{\uparrow\downarrow} + N^{\uparrow\uparrow}} = \pm \frac{N^u - N^d}{N^u + N^d} \quad (5.9)$$

After each solenoid field reversal the sign in the right part of Eq. 5.9 has to be changed. The positive (negative) sign has to be applied, if the spin in the downstream (upstream) cell is aligned with the muon spin.

By taking all events from both field settings into account, one obtains:

$$A_{raw} = \frac{N^u - N^d}{N^u + N^d} - \frac{N'^u - N'^d}{N'^u + N'^d} \quad (5.10)$$

$N^u$  is the number of all hadrons in the upstream (u) cell and  $N^d$  is the number of all hadrons in the downstream (d) cell. The primed and unprimed numbers count the hadrons for the two different cases of solenoid field setting.

In order to improve the statistical error in the determination of the asymmetry, different approaches have been made to calculate the longitudinal spin asymmetry



with weighting methods.

The first method uses a weighting factor  $w = fDP_b$  (see [38]).

$$A_{LL}^I = \frac{1}{2P_t(1-\alpha^2)} \left[ \frac{\sum_u w - \sum_d w}{\sum_u w^2 + \sum_d w^2} - \frac{\sum'_u w - \sum'_d w}{\sum'_u w^2 + \sum'_d w^2} \right] \quad (5.11)$$

$$\delta A_{LL}^I = \frac{1}{2P_t\sqrt{1-\alpha^2}} \sqrt{\frac{1}{\sum_u w^2 + \sum_d w^2} + \frac{1}{\sum'_u w^2 + \sum'_d w^2}} \quad (5.12)$$

Eq. 5.11 is a first order approximation for the calculation of the asymmetry, which assumes that the acceptances of the two cells are similar. The difference of the acceptance is included in the factor  $\alpha$ , which is estimated by:

$$\alpha \approx \tilde{\alpha} = \frac{1}{2} \cdot \left[ \frac{\sum_u w - \sum_d w}{\sum_u w^2 + \sum_d w^2} + \frac{\sum'_u w - \sum'_d w}{\sum'_u w^2 + \sum'_d w^2} \right] \quad (5.13)$$

In Eq. 5.13, the sums for oppositely polarised target cells are now added up and thus only the detector asymmetry should have an influence.

In a second method, also presented in [38], the unbalanced target cell acceptance is taken better into account. Here,  $\alpha$  is not only a scaling factor, but included in the sum of the weights for the different target cells.

$$A_{LL}^{II} = \frac{1}{2P_t} \left[ \frac{(1-\tilde{\alpha})\sum_u w - (1+\tilde{\alpha})\sum_d w}{(1-\tilde{\alpha})\sum_u w^2 + (1+\tilde{\alpha})\sum_d w^2} - \frac{(1-\tilde{\alpha})\sum'_u w - (1+\tilde{\alpha})\sum'_d w}{(1-\tilde{\alpha})\sum'_u w^2 + (1+\tilde{\alpha})\sum'_d w^2} \right]$$

$$A_{LL}^{II} = \frac{1}{2P_t} \left[ \frac{\sum_u w - \tilde{r}\sum_d w}{\sum_u w^2 + \tilde{r}\sum_d w^2} - \frac{\sum'_u w - \tilde{r}\sum'_d w}{\sum'_u w^2 + \tilde{r}\sum'_d w^2} \right] \quad (5.14)$$

$$\tilde{r} = \frac{(1+\tilde{\alpha})}{(1-\tilde{\alpha})}$$

$$\delta A_{LL}^{II} = \frac{1}{2P_t\sqrt{1-\tilde{\alpha}^2}} \sqrt{\frac{1}{\sum_u w^2 + \tilde{r}\sum_d w^2} + \frac{1}{\sum'_u w^2 + \tilde{r}\sum'_d w^2}} \quad (5.15)$$

In both methods the target polarisation is not included in the weights, as only non time dependent values should enter. Only then is the cancellation of the detector asymmetry given.

The average target polarisation  $P_t$  in Eq. 5.11 and Eq. 5.14 is calculated as the weighted average of the two target cells and the two field settings respectively:

$$P_t = \frac{1}{4} \cdot \left[ \frac{\sum_{runs} |P_u| N_u^h}{\sum_{runs} N_u^h} + \frac{\sum_{runs} |P_d| N_d^h}{\sum_{runs} N_d^h} + \frac{\sum'_{runs} |P_u| N_u^h}{\sum'_{runs} N_u^h} + \frac{\sum'_{runs} |P_d| N_d^h}{\sum'_{runs} N_d^h} \right]$$

The  $N^h$  are the numbers of hadrons for events in the upstream or downstream cells for each target polarisation setting.

In a third method (see [39]) the target polarisation is included in the weight and enters in the asymmetry calculation for each event. It is:

$$\begin{aligned}
A_{LL}^{III} &= \frac{\pm\sqrt{b^2 - 4ac} - b}{2a} & (5.16) \\
a &= \delta \langle \beta'_u \rangle_w \langle \beta_d \rangle_w - \langle \beta_u \rangle_w \langle \beta'_d \rangle_w \\
b &= \delta(\langle \beta'_u \rangle_w + \langle \beta_d \rangle_w) - (\langle \beta_u \rangle_w + \langle \beta'_d \rangle_w) \\
c &= \delta - 1 \\
\delta &= \frac{\sum_u w \sum'_d w}{\sum'_u w \sum_d w} \\
\langle \beta_{u,d}^{(t)} \rangle_w &= \frac{\sum_{u,d}^{(t)} w_{u,d} \beta_{u,d}}{\sum_{u,d}^{(t)} w_{u,d}}
\end{aligned}$$

For the weights  $\beta$  and  $w$  we use:

$$\begin{aligned}
\beta &= P_b f D \\
w &= P_t P_b f D
\end{aligned}$$

And the statistical error is given by:

$$\delta A_{LL}^{III} = \left( \frac{\partial A}{\partial \delta} \delta_\delta \right)^2 \quad (5.17)$$

The formulas of Eq. 5.11, 5.14 and 5.16 are used to calculate the single hadron cross section asymmetries.

One of the goals to determine the asymmetry in different ways, is to study the influence of the detector asymmetry. This can only be achieved if the data quality is stable and no major changes on the detector setup have been applied. Therefore, only the “**consecutive configuration**” is used to calculate the asymmetry. In the consecutive configuration, two or three run groups with opposite solenoid field setting are combined and for each group the asymmetry is calculated individually. In this way, the detector stability is better guaranteed for each setting than in the “**global configuration**”, where the asymmetries are calculated for a full data taking period. The grouping of the runs for the consecutive configuration can be found on the COMPASS stability web page [32]. Runs taken during the solenoid field rotation are excluded.

The average target polarisation needed for the first two methods is calculated for each group. The detector asymmetry  $\tilde{\alpha}$  is determined globally, i.e. by summing up all groups. As they are included in the weight, all other values are computed for each event respectively.

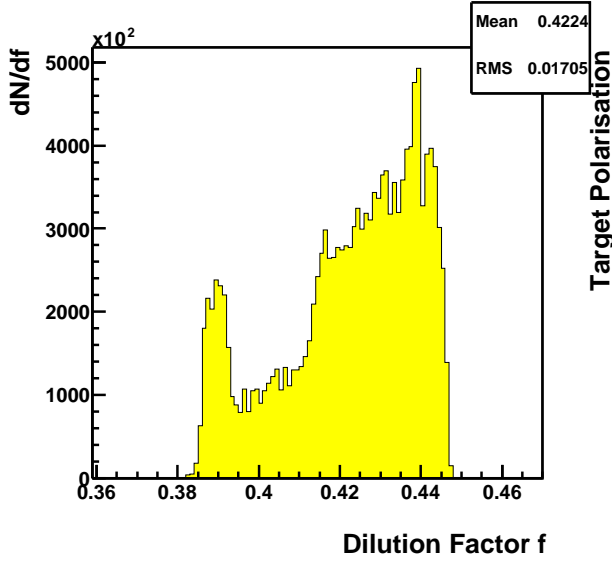


Figure 5.15: Dilution Factor  $f$  obtained from [40]

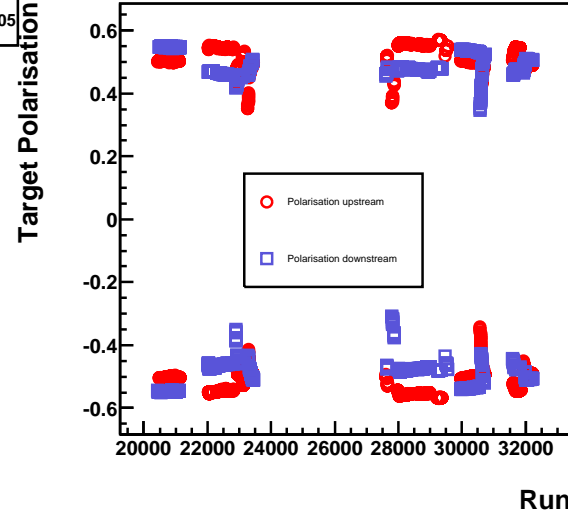


Figure 5.16: Target Polarisation obtained from the data base

### 5.4.2 Dilution factor

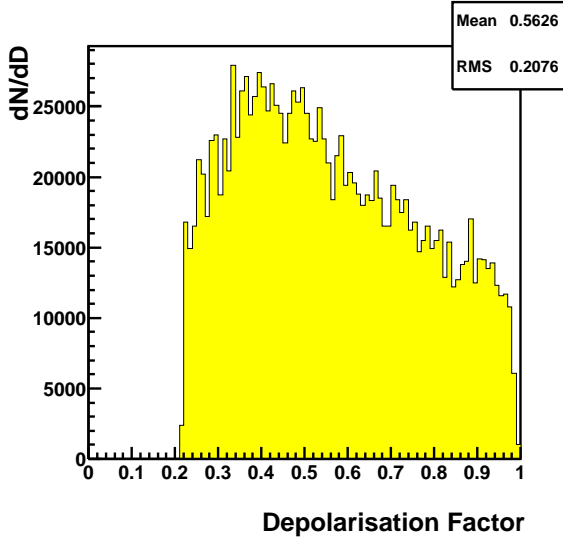
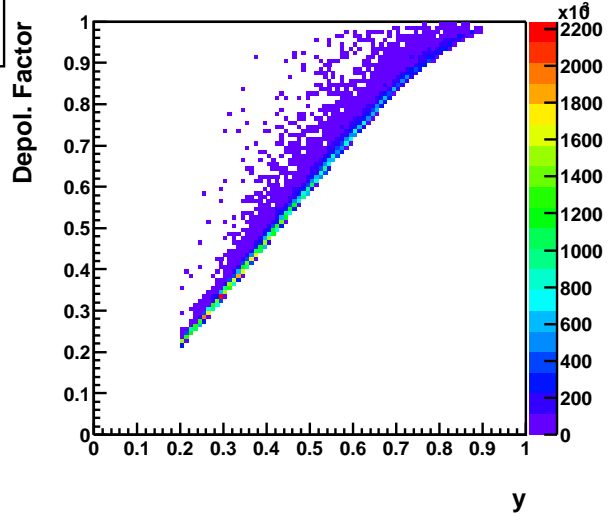
The dilution factor, which is defined as the number of polarisable nucleons in the target material divided by the number of all nucleons, is calculated with a Fortran routine, which includes a parametrisation for the dilution factor (see [40] and [17]). The routine provides two results, one for inclusive and one for semi-inclusive triggers. Here, the semi-inclusive trigger is used and the dilution calculated for each event, as it is included in the weights (see Fig. 5.15). The average of the dilution factor is  $\langle f \rangle = 0.42$ .

### 5.4.3 Depolarisation Factor

The depolarisation factor is defined by Eq. 2.17 as

$$D = \frac{y(2-y)(1 + \frac{1}{2}\gamma^2 y)}{(1 + \gamma^2)[2(1-y - \frac{\gamma^2 y^2}{4})(\frac{1+R}{1+\gamma^2}) + y^2]}$$

The factor  $R$ , which is the ratio of the longitudinal and the transversal cross section  $R = \frac{\sigma^L}{\sigma^T}$  (see Eq. 2.15), is obtained by the Fortran function given in [41]. The depolarisation factor is calculated event by event and included in the weights. The average depolarisation factor is  $\langle D \rangle = 0.57$  (see Fig. 5.17). The almost linear correlation of  $D$  and  $y$  can be seen in Fig. 5.18.

Figure 5.17: Depolarisation Factor  $D$ Figure 5.18: Depolarisation Factor vs.  $y$ 

#### 5.4.4 Target Polarisation

As the information about the target polarisation in PHAST is not reliable, it is extracted from the table `tb_offlinepolar` in the MySQL database of the run logbook. For almost all runs more than one measurement is available, and the average is taken. Some of the runs do not have a direct measurement. Then, the last value before and the first value after the run are taken. If they match in sign, the average is taken. If the signs do not match the value agreeing with the sign from the run list on the stability page is used. The values of the polarisations of the upstream and the downstream cell of the target are shown in Fig. 5.16.

For negative microwave settings, the polarisation of the upstream cell is defined to be always negative and the polarisation of the downstream cell always positive and for positive settings vice versa. The target spin direction is always given by the product of the solenoid current and the target cell polarisation. Positive values mean that the spin points upstream and is thus aligned with the muon spin. For negative values, the spin points downwards and is therefore oppositely orientated as the muon spin.

#### 5.4.5 Beam Polarisation

The polarisation of the muons originates in the parity violation of the pion and kaon decay. The polarisation  $P_\mu$  can be calculated as a function of the energy and mass

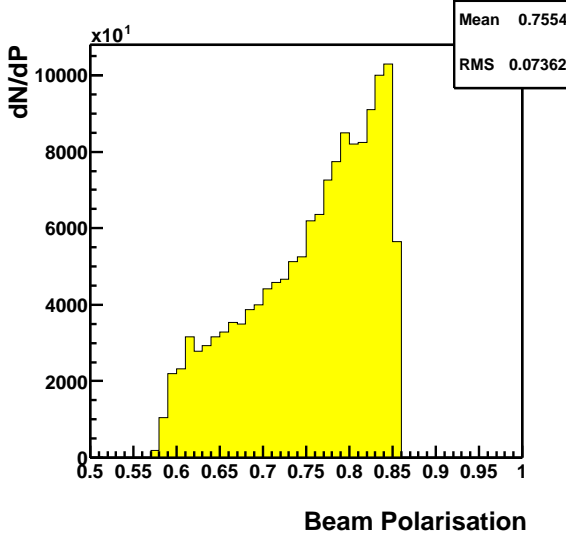
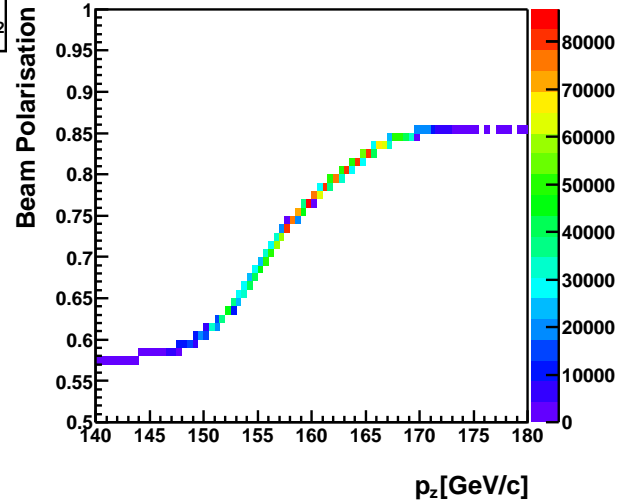


Figure 5.19: Beam Polarisation

Figure 5.20: Dependence of the beam polarisation on  $z$  component of the beam momentum  $p_z$ 

of the parent particle and the muon:

$$P_\mu = -\frac{m_{\pi,K}^2 + \left(1 - \frac{2E_{\pi,K}}{E_\mu}\right)m_\mu^2}{m_{\pi,K}^2 - m_\mu^2} \quad (5.18)$$

As the parent particle is not known, the M2 beam line has been simulated to obtain the beam polarisation. The values for the simulated points are interpolated to allow a determination of the beam polarisation for each event. The polarisation is extracted in this way and used in the analysis (see Fig. 5.19). The dependence on momentum of the incident muon is shown in Fig. 5.20. The average beam polarisation is  $\langle P_b \rangle = 0.76$ .

### 5.4.6 Results

Now we have all the necessary ingredients to determine the asymmetries with the three methods presented in chapter 5.4.1. The asymmetries are computed for each group of runs. Then, the weighted average is calculated for each period and for the

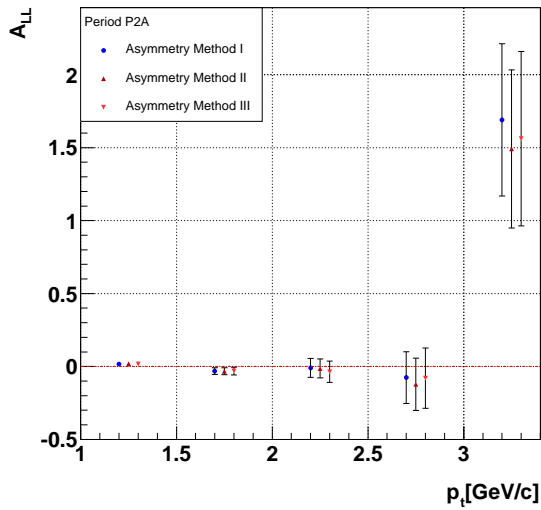


Figure 5.21: Asymmetries for the period P2A in 2002

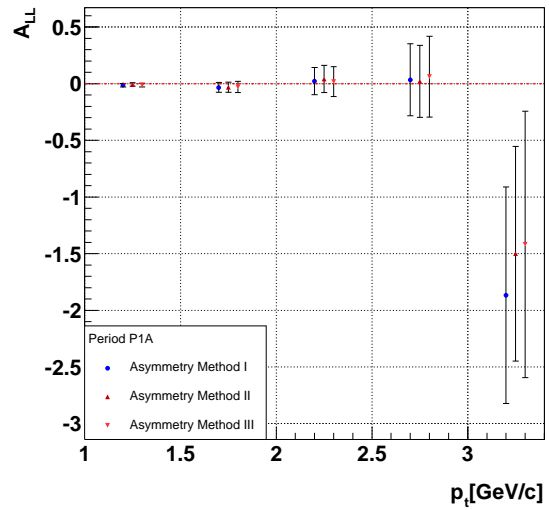


Figure 5.22: Asymmetries for the period P1A in 2003

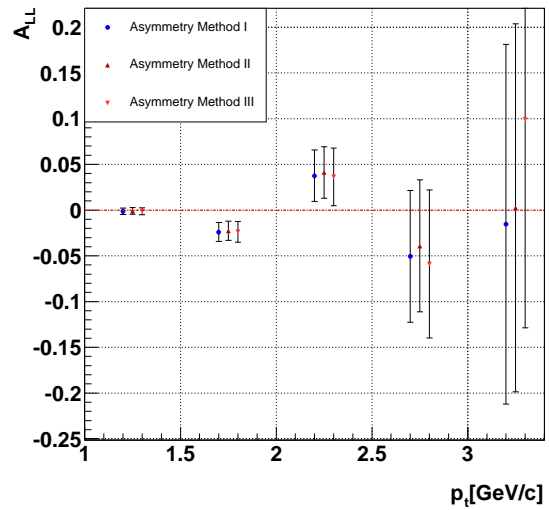
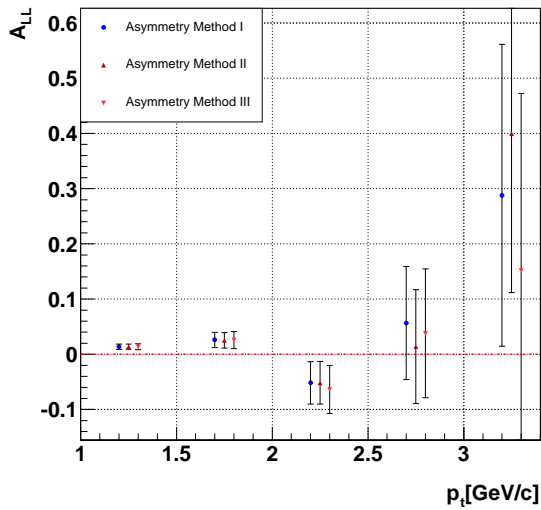


Figure 5.23: Weighted average of asymmetries of all periods in 2002 (left) and 2003 (right)

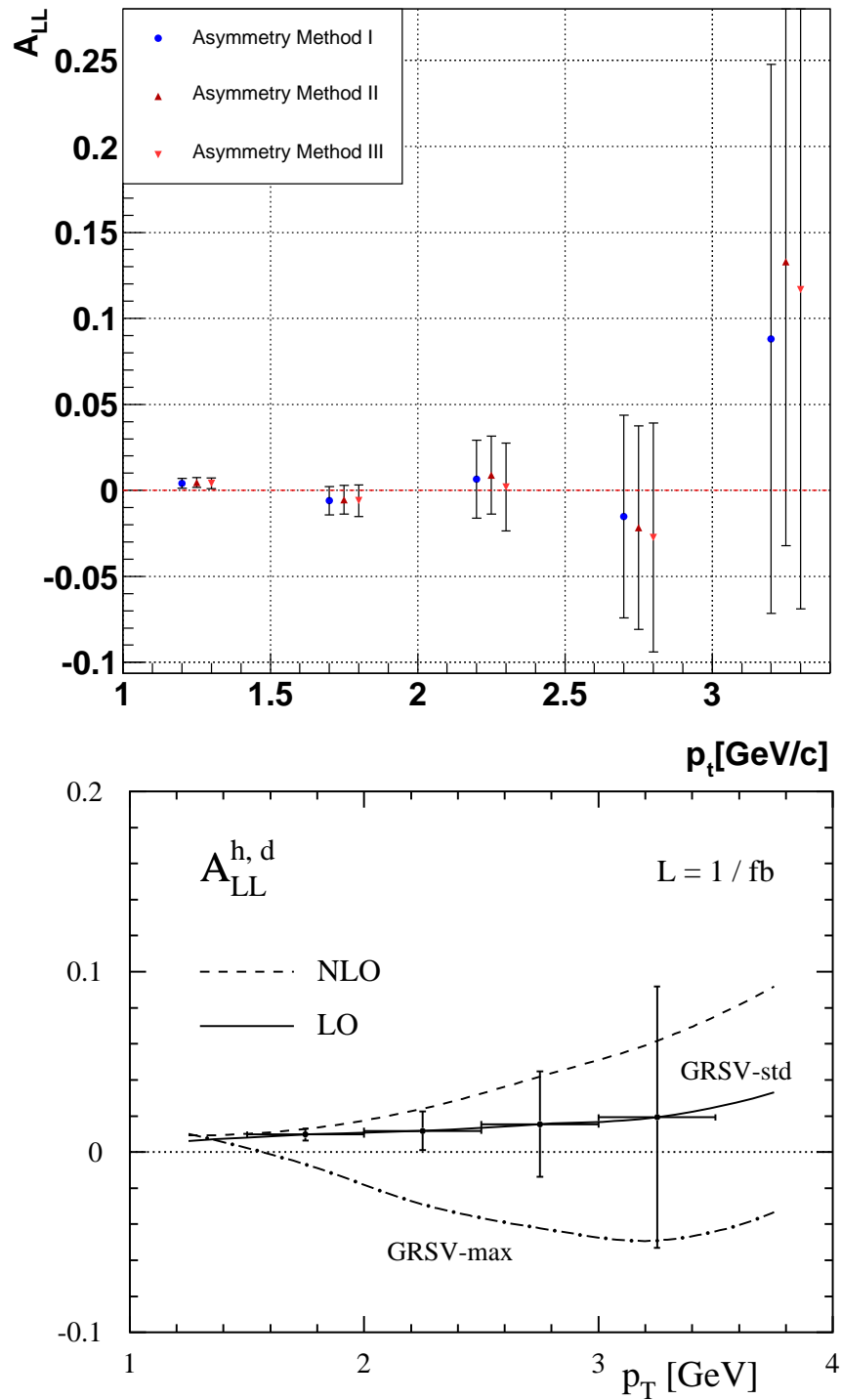


Figure 5.24: Experimental result for the weighted average of the asymmetries for all periods (top) and the calculations from [36] (bottom)

Table 5.2: Counting rules for the weights

Counting rules				
Periods 2002	P2D, P2E, P2F, P2G(first part)		P2A, P2G(second part)	
Periods 2003	P1A, P1B, P1C, P1D, P1E, P1I		P1F, P1J	
Microwave Setting	+		-	
Upstream Polarisation	+		-	
Solenoid Current	+	-	+	-
Muon Spin	$\Leftarrow$			
Target Spin	$\Leftarrow$	$\Rightarrow$	$\Rightarrow$	$\Leftarrow$
Weights	$w', \beta'$	$w, \beta$	$w, \beta$	$w', \beta'$

each year of data taking.

$$\langle A_{LL} \rangle = \frac{\sum_{groups} \frac{A_{LL}^{group}}{(\delta A_{LL}^{group})^2}}{\sum_{groups} \frac{1}{(\delta A_{LL}^{group})^2}} \quad (5.19)$$

One has to take into account that the sign of the asymmetry switches with every microwave reversal. The different microwave settings are shown in Tab. 5.2. Once, in P2G, the microwave field has been changed within the period. The first run used after the change has the run number 23267.

For positive microwave settings we count the unprimed quantities, if the solenoid current is negative and primed quantities, if the solenoid current is positive (see Tab. 5.2).

The comparison of the weighted average over all groups for the three methods for one selected period of the 2002 and the 2003 data respectively is shown in Fig. 5.21 and Fig. 5.22. For all 2002 and 2003 periods see Fig. C.1 and Fig. C.2 in the appendix. The values for the asymmetries and their errors are compatible for the different methods.

The weighted average of the asymmetries for all 2002 and 2003 periods is shown in Fig. 5.23. The results for the different methods are compatible with each other and with zero in a two  $\sigma$  range.

The weighted average of all 2002 and 2003 runs is shown in Fig. 5.24 together with the theoretical prediction for leading order and next to leading order calculations. A positive asymmetry is predicted for small transverse momentum in all three results. The numerical results for all 2002 and 2003 data for all bins in  $p_t$  and the weighted average of these bins is shown in Tab. 5.3. The result for the weighted average



Table 5.3:  $p_t$  dependent cross section asymmetries  $A_{LL}$  for high- $p_t$  hadron production obtained with the different weighting methods for all 2002 and 2003 data and the weighted average  $\langle A_{LL} \rangle_{p_t}$  of all bins

$p_t^{down}[\text{GeV}/c^2]$	$p_t^{up}[\text{GeV}/c^2]$	$A_{LL}^I$	$A_{LL}^{II}$	$A_{LL}^{III}$
1	1.5	$0.00422 \pm 0.00286$	$0.00455 \pm 0.00286$	$0.00419 \pm 0.00309$
1.5	2	$-0.00601 \pm 0.00831$	$-0.00542 \pm 0.00832$	$-0.00599 \pm 0.00915$
2	2.5	$0.00648 \pm 0.0227$	$0.00892 \pm 0.0227$	$0.00189 \pm 0.0255$
2.5	3	$-0.0152 \pm 0.0589$	$-0.0217 \pm 0.0591$	$-0.0274 \pm 0.0665$
3	3.5	$0.0882 \pm 0.16$	$0.133 \pm 0.165$	$0.117 \pm 0.186$
$\langle A_{LL} \rangle_{p_t}$		$0.00317 \pm 0.00268$	$0.00355 \pm 0.00268$	$0.0031 \pm 0.00291$

of all  $p_t$  bins of the double spin cross section asymmetry for single high- $p_t$  hadron production is  $A_{LL} = 0.003 \pm 0.003$ .

The compatibility of the asymmetry  $A_{LL}$  with zero does not imply a gluon polarisation which is equally zero as the asymmetry of the background processes contributes to the asymmetry. The gluon polarisation can only be extracted from the cross section asymmetries of the photon-gluon-fusion process. In the case that the asymmetries for the background processes have opposite sign they could cancel a possible asymmetry for the photon-gluon-fusion process. To extract the gluon polarisation from the measured asymmetry it is necessary to analyse the background processes in a detailed Monte Carlo study.



# Chapter 6

## Summary

Two analyses concerning the deep inelastic scattering have been done in this thesis. In the inclusive analysis the  $x$  and  $Q^2$  dependent scattering cross section has been determined with two Monte Carlo generators, PYTHIA and LEPTO, and compared to the experimental result of the NMC experiment. Different parametrisations for the parton distribution functions have been investigated. A good agreement between data and Monte Carlo has been found for the LEPTO generator whereas the PYTHIA cross section is only compatible with the NMC results for larger values of  $y$ .

In order to obtain first results for inclusive cross sections at COMPASS, the integrated luminosities of all periods of 2002 and 2003 have been evaluated. A comparison of the result for the inclusive cross section with the NMC cross section yields a difference of about 30%-50% using all triggers. A separate analysis for each trigger revealed discrepancies of the Monte Carlo description of the Calorimeter Trigger. A further analysis of the trigger description in the Monte Carlo software will be necessary to improve the detector description.

The  $p_t$  dependent cross section and the cross section asymmetries for single high- $p_t$  hadron production have been determined in the semi-inclusive analysis. An identification for pions, kaons and protons has been performed using the RICH detector. The cross sections have been calculated and presented for all charged hadrons, pions, kaons and protons separately. The results for all charged hadrons and pions have been compared to a theoretical prediction. They are compatible to a next to leading order calculation for the 2002 data within the statistical error. Although, the cross sections determined with the 2003 data are larger. This is due to a decreased detector efficiency for the 2003 data of about 0.05.

In the last chapter the  $p_t$  dependent cross section asymmetry for semi-inclusive single high- $p_t$  hadron production has been evaluated for all 2002 and 2003 data respectively. Different methods for the determination of the asymmetry have been presented and shown to be compatible. The measured asymmetries within the kine-

matical range of COMPASS are compatible with zero. This does not mean that the polarised gluon distribution  $\Delta G/G$  is zero as background processes may contribute and compensate the photon-gluon-fusion asymmetry.

With the determination of the cross section asymmetries an important step has been done to evaluate the polarised gluon distribution function  $\Delta G/G$  from single high- $p_t$  hadron events.

# List of Figures

2.1	The Deep Inelastic Scattering(DIS) Graph . . . . .	7
2.2	World data of $F_2^P(x, Q^2)$ . . . . .	9
2.3	Polarised Parton Distribution Functions . . . . .	13
2.4	PGF and background processes . . . . .	16
3.1	Top view of the COMPASS Spectrometer . . . . .	20
3.2	Target geometry with spin setups . . . . .	22
3.3	The COMPASS RICH 1 . . . . .	25
3.4	COMPASS Trigger System . . . . .	26
4.1	Positions of the primary vertex . . . . .	34
4.2	Momenta of incoming and scattered muon . . . . .	36
4.3	Kinematical distributions for inclusive scattering . . . . .	37
4.4	The Monte Carlo Chain . . . . .	38
4.5	Comparison of real data with PYTHIA defaults . . . . .	40
4.6	Comparison of real data with PYTHIA (GRV94) . . . . .	42
4.7	Comparison of real data with LEPTO (CTEQ2L) . . . . .	43
4.8	Comparison of real data with LEPTO (GRV98L) . . . . .	45
4.9	Differential cross section measured at NMC [34] . . . . .	46
4.10	Ratio of PYTHIA divided by NMC cross sections . . . . .	47
4.11	Ratio of LEPTO and NMC cross section . . . . .	48
4.12	All detector efficiency (PYTHIA,STD) . . . . .	50
4.13	All detector efficiency (LEPTO,STD) . . . . .	50
4.14	Beam fluxes . . . . .	53
4.15	Inclusive Cross Sections with PYTHIA efficiencies . . . . .	54
4.16	Inclusive Cross Sections with LEPTO efficiencies . . . . .	55
4.17	Fractions of the triggers in real data and MC . . . . .	56
4.18	Trigger dependent Efficiencies LEPTO (std) . . . . .	58
4.19	Cross Sections Trigger dependent for LEPTO (std) . . . . .	59
4.20	Cross Sections $\frac{d\sigma}{dx}$ and $\frac{d\sigma}{dQ^2}$ for the Inclusive Middle Trigger . . . . .	61
5.1	Inclusive Variables in semi-inclusive events . . . . .	64

5.2	$E_{HCAL}$ versus $ \vec{p}_h $ . . . . .	66
5.3	$z$ and $x_F$ distributions . . . . .	67
5.4	Target angular acceptance . . . . .	68
5.5	$p_t$ Distribution . . . . .	69
5.6	Hadron Multiplicity . . . . .	69
5.7	Fractions of RICH identified hadrons . . . . .	71
5.8	$p_t$ distributions of different hadrons . . . . .	72
5.9	Trigger ratios in semi-inclusive events for 2003 . . . . .	74
5.10	Comparison of the inclusive variables in real data with PYTHIA defaults for semi-inclusive events . . . . .	75
5.11	Comparison of semi-inclusive variables in real data with PYTHIA defaults for semi-inclusive events . . . . .	76
5.12	Particle identification for 2003 data . . . . .	77
5.13	Semi-inclusive cross sections for single high- $p_t$ hadron production and efficiencies for 2002 . . . . .	79
5.14	Semi-inclusive cross sections for single high- $p_t$ hadron production and efficiencies for 2003 . . . . .	80
5.15	Dilution Factor . . . . .	84
5.16	Target Polarisation obtained from the data base . . . . .	84
5.17	Depolarisation Factor $D$ . . . . .	84
5.18	Depolarisation Factor vs. $y$ . . . . .	84
5.19	Beam Polarisation . . . . .	86
5.20	Dependence of the beam polarisation on $z$ component of the beam momentum $p_z$ . . . . .	86
5.21	Asymmetries for the period P2A in 2002 . . . . .	86
5.22	Asymmetries for the period P1A in 2003 . . . . .	86
5.23	Asymmetries for 2002 and 2003 . . . . .	88
5.24	Comparison of the cross section asymmetries . . . . .	89
A.1	Trigger dependent analysis PYTHIA (std) . . . . .	107
A.2	Trigger dependent analysis PYTHIA (GRV94L) . . . . .	108
A.3	Trigger dependent analysis LEPTO (std.) . . . . .	109
A.4	Trigger dependent analysis LEPTO (GRV98M) . . . . .	110
A.5	Trigger dependent comparison of the cross section to NMC . . . . .	111
A.6	Cross Sections $\frac{d\sigma}{dx}$ for all triggers . . . . .	112
A.7	Cross Sections $\frac{d\sigma}{dQ^2}$ for all triggers . . . . .	113
B.1	Particle identification for 2002 data . . . . .	115
B.2	Comparison of 2002 data with PYTHIA defaults for semi-inclusive events . . . . .	116

C.1 Weighted means of the asymmetry for all periods of 2002 . . . . . 122  
C.2 Weighted means of the asymmetry for all periods of 2003 . . . . . 123





# List of Tables

2.1	Inclusive Variables in Deep Inelastic Scattering . . . . .	8
2.2	DIS Semi Inclusive Variables . . . . .	14
3.1	Inclusion of the HCAL and the Vetos in the different trigger . . . . .	27
4.1	Number of target particles per area . . . . .	31
4.2	Target Positions . . . . .	33
4.3	Positions and bits of the trigger system . . . . .	35
4.4	Event Statistics in Inclusive Scattering . . . . .	35
4.5	Total cross sections and generated Events for LEPTO and PYTHIA with different PDFs . . . . .	44
5.1	Number of beam particles and integrated luminosities for each period	78
5.2	Counting rules for the weights . . . . .	87
5.3	Numerical results for $A_{LL}$ . . . . .	88
B.1	Numerical results for the cross section for semi-inclusive high- $p_t$ hadron production from 2002 data . . . . .	118
B.2	Numerical results for the cross section for semi-inclusive high- $p_t$ hadron production from 2003 data . . . . .	119



# Appendix A

## Inclusive Cross Section Additives

### A.1 Numerical Results for the Inclusive Cross Section

Efficiencies from		LEPTO		PYTHIA	
$x$	$Q^2$ [GeV/c <sup>2</sup> ]	CTEQ2L	GRV98L	CTEQ2L	GRV94M
$d^2\sigma/dxdQ^2$ [fb/(GeV/c <sup>2</sup> )]					
0.0021	0.3	-1 ± -1	-1 ± -1	86.9 ± 0.907	86.5 ± 0.903
0.0021	0.5	-1 ± -1	-1 ± -1	19.9 ± 0.226	19.9 ± 0.228
0.0021	0.7	-1 ± -1	-1 ± -1	5.94 ± 0.0789	5.88 ± 0.0783
0.0021	0.9	-1 ± -1	-1 ± -1	1.54 ± 0.0268	1.61 ± 0.0295
0.0021	1.1	0.0753 ± 0.00912	0.11 ± 0.0239	0.0576 ± 0.000866	0.0612 ± 0.00092
0.0021	1.3	0.000104 ± 3.67e - 05	0.000104 ± 3.67e - 05	-1 ± -1	-1 ± -1
0.00609	0.3	-1 ± -1	-1 ± -1	33.4 ± 0.412	33.5 ± 0.407
0.00609	0.5	-1 ± -1	-1 ± -1	19.4 ± 0.237	19.6 ± 0.242
0.00609	0.7	-1 ± -1	-1 ± -1	10.2 ± 0.131	10.3 ± 0.134
0.00609	0.9	-1 ± -1	-1 ± -1	6.36 ± 0.0886	6.35 ± 0.0889
0.00609	1.1	7.59 ± 0.134	7.67 ± 0.132	4.25 ± 0.0658	4.21 ± 0.0655
0.00609	1.3	3.89 ± 0.0816	3.81 ± 0.0773	2.4 ± 0.0439	2.43 ± 0.0449
0.00609	1.5	2.18 ± 0.0593	2.16 ± 0.0555	1.33 ± 0.0295	1.34 ± 0.0312
0.00609	1.7	0.937 ± 0.0307	1.08 ± 0.0369	0.634 ± 0.0175	0.596 ± 0.0153
0.00609	1.9	0.364 ± 0.018	0.357 ± 0.0159	0.228 ± 0.00694	0.248 ± 0.00915
0.00609	2.1	0.000392 ± 8.05e - 06	0.000951 ± 1.95e - 05	0.0348 ± 0.000714	0.0231 ± 0.000475
0.00609	2.3	0.00162 ± 0.000146	0.00162 ± 0.000146	-1 ± -1	-1 ± -1
0.00609	2.5	2.6e - 05 ± 1.84e - 05	2.6e - 05 ± 1.84e - 05	-1 ± -1	-1 ± -1
0.0101	0.3	-1 ± -1	-1 ± -1	5.68 ± 0.109	5.91 ± 0.112
0.0101	0.5	-1 ± -1	-1 ± -1	9.93 ± 0.149	9.75 ± 0.144
0.0101	0.7	-1 ± -1	-1 ± -1	6.31 ± 0.0946	6.33 ± 0.0949
0.0101	0.9	-1 ± -1	-1 ± -1	4.09 ± 0.0665	4.11 ± 0.0671
0.0101	1.1	4.88 ± 0.0965	5.01 ± 0.0992	2.84 ± 0.0511	2.72 ± 0.0474
0.0101	1.3	3.21 ± 0.0708	3.2 ± 0.0672	2 ± 0.0383	2.02 ± 0.0399
0.0101	1.5	2.55 ± 0.0639	2.46 ± 0.0578	1.54 ± 0.0326	1.59 ± 0.0356
0.0101	1.7	1.83 ± 0.0496	1.81 ± 0.045	1.16 ± 0.0256	1.18 ± 0.0282
0.0101	1.9	1.47 ± 0.0436	1.63 ± 0.0496	0.998 ± 0.0271	0.922 ± 0.0238
0.0101	2.1	1.22 ± 0.0429	1.17 ± 0.037	0.752 ± 0.0209	0.774 ± 0.0239
0.0101	2.3	0.94 ± 0.0421	0.952 ± 0.041	0.587 ± 0.0221	0.585 ± 0.023
0.0101	2.5	0.609 ± 0.0346	0.55 ± 0.0281	0.355 ± 0.0158	0.355 ± 0.0171
0.0101	2.7	0.287 ± 0.0211	0.34 ± 0.0233	0.21 ± 0.0123	0.222 ± 0.0153
0.0101	2.9	0.101 ± 0.0106	0.119 ± 0.0112	0.125 ± 0.0118	0.118 ± 0.0125
0.0101	3.1	0.00204 ± 0.000275	0.000638 ± 6.37e - 05	0.0272 ± 0.00272	0.0304 ± 0.00409
0.0101	3.3	-1 ± -1	-1 ± -1	0.000372 ± 2.44e - 05	0.000817 ± 5.34e - 05
0.0101	3.5	7.79e - 05 ± 3.18e - 05	7.79e - 05 ± 3.18e - 05	-1 ± -1	-1 ± -1
0.0101	3.9	1.3e - 05 ± 1.3e - 05	1.3e - 05 ± 1.3e - 05	-1 ± -1	-1 ± -1
0.0141	0.3	-1 ± -1	-1 ± -1	0.287 ± 0.0287	0.224 ± 0.0183
0.0141	0.5	-1 ± -1	-1 ± -1	4.58 ± 0.0888	4.42 ± 0.0821
0.0141	0.7	-1 ± -1	-1 ± -1	4.14 ± 0.0751	4.14 ± 0.075
0.0141	0.9	-1 ± -1	-1 ± -1	3 ± 0.0585	3.02 ± 0.0591

Efficiencies from		LEPTO		PYTHIA	
		CTEQ2L	GRV98L	CTEQ2L	GRV94M
$x$	$Q^2$ [GeV/c <sup>2</sup> ]	$d^2\sigma/dxdQ^2$ [fb/(GeV/c <sup>2</sup> )]			
0.0141	1.1	3.72 ± 0.087	3.61 ± 0.0807	2.03 ± 0.0407	2.07 ± 0.043
0.0141	1.3	2.42 ± 0.0606	2.45 ± 0.0595	1.52 ± 0.0336	1.5 ± 0.0335
0.0141	1.5	1.8 ± 0.0499	1.86 ± 0.0506	1.18 ± 0.0292	1.15 ± 0.0285
0.0141	1.7	1.44 ± 0.0448	1.38 ± 0.0388	0.861 ± 0.0212	0.902 ± 0.025
0.0141	1.9	1.18 ± 0.0402	1.11 ± 0.0335	0.706 ± 0.0186	0.745 ± 0.0226
0.0141	2.1	0.952 ± 0.0361	0.925 ± 0.032	0.6 ± 0.0184	0.608 ± 0.0204
0.0141	2.3	0.759 ± 0.0308	0.726 ± 0.0267	0.471 ± 0.0151	0.478 ± 0.0169
0.0141	2.5	0.662 ± 0.0297	0.602 ± 0.0235	0.381 ± 0.0126	0.412 ± 0.0161
0.0141	2.7	0.587 ± 0.0307	0.543 ± 0.0243	0.342 ± 0.0132	0.373 ± 0.0175
0.0141	2.9	0.47 ± 0.0246	0.439 ± 0.0198	0.267 ± 0.00999	0.276 ± 0.0123
0.0141	3.1	0.433 ± 0.0274	0.443 ± 0.0253	0.262 ± 0.013	0.263 ± 0.0147
0.0141	3.3	0.412 ± 0.0341	0.412 ± 0.0315	0.217 ± 0.0141	0.203 ± 0.0144
0.0141	3.5	0.342 ± 0.0385	0.296 ± 0.0288	0.176 ± 0.015	0.169 ± 0.0166
0.0141	3.7	0.318 ± 0.059	0.205 ± 0.0284	0.111 ± 0.0134	0.131 ± 0.0217
0.0141	3.9	0.0762 ± 0.0143	0.103 ± 0.0198	0.0711 ± 0.0124	0.0566 ± 0.00981
0.0141	4.1	0.00317 ± 0.000785	0.00377 ± 0.00126	0.0402 ± 0.0134	0.0234 ± 0.00581
0.0141	4.3	-1 ± -1	-1 ± -1	0.00111 ± 7.01e - 05	0.00285 ± 0.00018
0.0141	4.5	0.000442 ± 7.58e - 05	0.000442 ± 7.58e - 05	-1 ± -1	-1 ± -1
0.0141	4.7	2.6e - 05 ± 1.84e - 05	2.6e - 05 ± 1.84e - 05	-1 ± -1	-1 ± -1
0.0181	0.5	-1 ± -1	-1 ± -1	1.03 ± 0.0385	1.01 ± 0.0363
0.0181	0.7	-1 ± -1	-1 ± -1	2.65 ± 0.0558	2.67 ± 0.0569
0.0181	0.9	-1 ± -1	-1 ± -1	2.24 ± 0.0523	2.06 ± 0.0448
0.0181	1.1	2.88 ± 0.0797	2.71 ± 0.0709	1.55 ± 0.0368	1.63 ± 0.0409
0.0181	1.3	1.87 ± 0.053	1.94 ± 0.0546	1.22 ± 0.0313	1.15 ± 0.0294
0.0181	1.5	1.44 ± 0.0445	1.44 ± 0.0426	0.894 ± 0.0237	0.888 ± 0.0244
0.0181	1.7	1.1 ± 0.0376	1.1 ± 0.0355	0.705 ± 0.0205	0.687 ± 0.0207
0.0181	1.9	0.872 ± 0.0323	0.944 ± 0.0345	0.595 ± 0.0194	0.582 ± 0.0194
0.0181	2.1	0.782 ± 0.0337	0.851 ± 0.0377	0.53 ± 0.0213	0.493 ± 0.019
0.0181	2.3	0.715 ± 0.0356	0.627 ± 0.0272	0.386 ± 0.0147	0.445 ± 0.0198
0.0181	2.5	0.534 ± 0.026	0.557 ± 0.0262	0.344 ± 0.0141	0.31 ± 0.0127
0.0181	2.7	0.49 ± 0.0287	0.507 ± 0.0282	0.309 ± 0.0152	0.283 ± 0.0146
0.0181	2.9	0.347 ± 0.0192	0.377 ± 0.0196	0.223 ± 0.00964	0.228 ± 0.0112
0.0181	3.1	0.345 ± 0.0232	0.327 ± 0.0195	0.208 ± 0.0108	0.203 ± 0.0121
0.0181	3.3	0.299 ± 0.0201	0.294 ± 0.0182	0.184 ± 0.00983	0.185 ± 0.0109
0.0181	3.5	0.207 ± 0.0124	0.276 ± 0.0201	0.169 ± 0.0109	0.129 ± 0.00652
0.0181	3.7	0.222 ± 0.0179	0.26 ± 0.0194	0.136 ± 0.00831	0.148 ± 0.0109
0.0181	3.9	0.22 ± 0.0193	0.242 ± 0.0217	0.127 ± 0.00959	0.121 ± 0.00913
0.0181	4.1	0.208 ± 0.0229	0.176 ± 0.0161	0.0862 ± 0.00635	0.103 ± 0.00993
0.0181	4.3	0.279 ± 0.0448	0.245 ± 0.0322	0.106 ± 0.0119	0.114 ± 0.016
0.0181	4.5	0.139 ± 0.0198	0.192 ± 0.0305	0.0823 ± 0.011	0.055 ± 0.00591
0.0181	4.7	0.21 ± 0.057	0.129 ± 0.0259	0.0444 ± 0.00649	0.0756 ± 0.0185
0.0221	0.5	0.00603 ± 0.000286	0.00603 ± 0.000286	-1 ± -1	-1 ± -1
0.0221	0.7	-1 ± -1	-1 ± -1	1.39 ± 0.0436	1.33 ± 0.0401
0.0221	0.9	-1 ± -1	-1 ± -1	1.58 ± 0.0414	1.6 ± 0.0421
0.0221	1.1	2.07 ± 0.0602	2.16 ± 0.0639	1.22 ± 0.0328	1.19 ± 0.0313
0.0221	1.3	1.4 ± 0.0422	1.62 ± 0.0534	0.99 ± 0.0302	0.874 ± 0.0237
0.0221	1.5	1.17 ± 0.0407	1.27 ± 0.0451	0.806 ± 0.0264	0.738 ± 0.0231
0.0221	1.7	1 ± 0.0418	0.925 ± 0.0332	0.581 ± 0.0186	0.63 ± 0.024
0.0221	1.9	0.783 ± 0.0343	0.836 ± 0.0366	0.505 ± 0.02	0.501 ± 0.02
0.0221	2.1	0.69 ± 0.0345	0.69 ± 0.0321	0.403 ± 0.0164	0.419 ± 0.0189
0.0221	2.3	0.556 ± 0.0285	0.601 ± 0.0303	0.344 ± 0.015	0.327 ± 0.0147
0.0221	2.5	0.524 ± 0.0324	0.513 ± 0.0286	0.299 ± 0.0147	0.314 ± 0.0176
0.0221	2.7	0.44 ± 0.0293	0.431 ± 0.0255	0.267 ± 0.0139	0.256 ± 0.0152
0.0221	2.9	0.385 ± 0.0288	0.386 ± 0.0264	0.215 ± 0.0129	0.223 ± 0.015
0.0221	3.1	0.294 ± 0.0199	0.362 ± 0.0266	0.201 ± 0.0128	0.175 ± 0.0104
0.0221	3.3	0.315 ± 0.0278	0.269 ± 0.0199	0.154 ± 0.00989	0.171 ± 0.0135
0.0221	3.5	0.202 ± 0.0158	0.248 ± 0.0196	0.144 ± 0.00981	0.127 ± 0.0088
0.0221	3.7	0.215 ± 0.0192	0.184 ± 0.0138	0.1 ± 0.006	0.126 ± 0.0101
0.0221	3.9	0.176 ± 0.0155	0.172 ± 0.0143	0.104 ± 0.0075	0.104 ± 0.00804
0.0221	4.1	0.143 ± 0.0119	0.152 ± 0.0139	0.0978 ± 0.00787	0.0814 ± 0.00571
0.0221	4.3	0.127 ± 0.0112	0.113 ± 0.00897	0.0714 ± 0.00469	0.0713 ± 0.00515
0.0221	4.5	0.122 ± 0.0128	0.128 ± 0.0133	0.0814 ± 0.00749	0.0662 ± 0.00589
0.0221	4.7	0.157 ± 0.0222	0.129 ± 0.0158	0.0621 ± 0.00621	0.0755 ± 0.00937
0.0261	0.7	-1 ± -1	-1 ± -1	0.212 ± 0.0162	0.192 ± 0.0132
0.0261	0.9	-1 ± -1	-1 ± -1	1.1 ± 0.0317	1.14 ± 0.0346
0.0261	1.1	1.8 ± 0.0623	1.64 ± 0.0534	0.931 ± 0.0278	0.969 ± 0.0305
0.0261	1.3	1.18 ± 0.041	1.15 ± 0.0382	0.702 ± 0.0211	0.734 ± 0.0232
0.0261	1.5	1.07 ± 0.0441	1.04 ± 0.0411	0.648 ± 0.0236	0.656 ± 0.0249
0.0261	1.7	0.728 ± 0.0287	0.858 ± 0.0369	0.516 ± 0.0201	0.448 ± 0.0157
0.0261	1.9	0.589 ± 0.026	0.627 ± 0.0275	0.382 ± 0.0149	0.362 ± 0.0142

Efficiencies from		LEPTO		PYTHIA	
		CTEQ2L	GRV98L	CTEQ2L	GRV94M
$x$	$Q^2$ [GeV/c <sup>2</sup> ]	$d^2\sigma/dxdQ^2$ [fb/(GeV/c <sup>2</sup> )]			
0.0261	2.1	0.543 ± 0.0288	0.553 ± 0.0275	0.332 ± 0.0146	0.333 ± 0.016
0.0261	2.3	0.513 ± 0.0336	0.419 ± 0.0218	0.274 ± 0.0128	0.31 ± 0.0187
0.0261	2.5	0.405 ± 0.0253	0.485 ± 0.0314	0.276 ± 0.016	0.238 ± 0.0132
0.0261	2.7	0.388 ± 0.0293	0.352 ± 0.023	0.216 ± 0.0125	0.232 ± 0.0161
0.0261	2.9	0.302 ± 0.0236	0.383 ± 0.0301	0.218 ± 0.0153	0.182 ± 0.0129
0.0261	3.1	0.29 ± 0.0233	0.254 ± 0.0181	0.156 ± 0.00979	0.163 ± 0.0116
0.0261	3.3	0.258 ± 0.0234	0.235 ± 0.0182	0.14 ± 0.00924	0.145 ± 0.0118
0.0261	3.5	0.218 ± 0.0205	0.19 ± 0.0146	0.108 ± 0.00681	0.122 ± 0.0102
0.0261	3.7	0.191 ± 0.0186	0.193 ± 0.0177	0.109 ± 0.00857	0.109 ± 0.0094
0.0261	3.9	0.152 ± 0.0157	0.193 ± 0.0192	0.109 ± 0.00948	0.0918 ± 0.00841
0.0261	4.1	0.176 ± 0.0215	0.161 ± 0.0164	0.0946 ± 0.0083	0.0892 ± 0.00954
0.0261	4.3	0.156 ± 0.0194	0.125 ± 0.0116	0.0719 ± 0.00553	0.0889 ± 0.0101
0.0261	4.5	0.0893 ± 0.0104	0.168 ± 0.02	0.0748 ± 0.00689	0.0696 ± 0.00773
0.0261	4.7	0.107 ± 0.0129	0.119 ± 0.014	0.0725 ± 0.00763	0.0624 ± 0.00659
0.0301	0.7	0.000195 ± 5.03e - 05	0.000195 ± 5.03e - 05	-1 ± -1	-1 ± -1
0.0301	0.9	-1 ± -1	-1 ± -1	0.502 ± 0.0266	0.446 ± 0.0211
0.0301	1.1	1.43 ± 0.0575	1.43 ± 0.055	0.785 ± 0.0278	0.809 ± 0.0302
0.0301	1.3	1.15 ± 0.0495	1.08 ± 0.0423	0.647 ± 0.0235	0.703 ± 0.0283
0.0301	1.5	0.797 ± 0.0328	0.763 ± 0.0295	0.48 ± 0.0168	0.498 ± 0.0187
0.0301	1.7	0.662 ± 0.0314	0.735 ± 0.0371	0.47 ± 0.0221	0.421 ± 0.0184
0.0301	1.9	0.628 ± 0.0352	0.651 ± 0.0352	0.391 ± 0.0194	0.382 ± 0.0197
0.0301	2.1	0.471 ± 0.0264	0.518 ± 0.0309	0.322 ± 0.0176	0.283 ± 0.0143
0.0301	2.3	0.431 ± 0.0294	0.391 ± 0.0222	0.23 ± 0.0114	0.255 ± 0.0159
0.0301	2.5	0.405 ± 0.0303	0.331 ± 0.0208	0.199 ± 0.011	0.223 ± 0.015
0.0301	2.7	0.328 ± 0.0279	0.337 ± 0.0251	0.187 ± 0.0123	0.206 ± 0.0163
0.0301	2.9	0.319 ± 0.0284	0.267 ± 0.0197	0.144 ± 0.00892	0.161 ± 0.0127
0.0301	3.1	0.293 ± 0.0298	0.293 ± 0.0266	0.153 ± 0.0121	0.161 ± 0.0151
0.0301	3.3	0.209 ± 0.0191	0.226 ± 0.0189	0.12 ± 0.00835	0.119 ± 0.00969
0.0301	3.5	0.218 ± 0.0226	0.247 ± 0.0242	0.12 ± 0.00987	0.114 ± 0.0105
0.0301	3.7	0.176 ± 0.0189	0.18 ± 0.018	0.101 ± 0.00876	0.101 ± 0.00983
0.0301	3.9	0.197 ± 0.0242	0.15 ± 0.0147	0.0869 ± 0.00726	0.104 ± 0.0114
0.0301	4.1	0.12 ± 0.0124	0.122 ± 0.0117	0.0668 ± 0.0052	0.0635 ± 0.00551
0.0301	4.3	0.133 ± 0.0162	0.107 ± 0.0103	0.0609 ± 0.00477	0.0731 ± 0.00781
0.0301	4.5	0.109 ± 0.0139	0.0941 ± 0.0101	0.0568 ± 0.0052	0.0658 ± 0.00754
0.0301	4.7	0.0904 ± 0.0128	0.0915 ± 0.0107	0.0532 ± 0.00536	0.0609 ± 0.0081
0.0341	0.7	1.3e - 05 ± 1.3e - 05	1.3e - 05 ± 1.3e - 05	-1 ± -1	-1 ± -1
0.0341	0.9	-1 ± -1	-1 ± -1	0.0476 ± 0.0107	0.0387 ± 0.00854
0.0341	1.1	1.06 ± 0.0539	0.992 ± 0.0485	0.57 ± 0.0262	0.587 ± 0.0279
0.0341	1.3	0.781 ± 0.0326	0.788 ± 0.0327	0.488 ± 0.0187	0.485 ± 0.0187
0.0341	1.5	0.735 ± 0.0377	0.717 ± 0.0332	0.438 ± 0.0187	0.451 ± 0.0216
0.0341	1.7	0.594 ± 0.031	0.516 ± 0.0229	0.304 ± 0.0118	0.355 ± 0.017
0.0341	1.9	0.501 ± 0.0283	0.516 ± 0.0309	0.318 ± 0.0176	0.293 ± 0.0149
0.0341	2.1	0.406 ± 0.027	0.416 ± 0.0235	0.233 ± 0.0114	0.247 ± 0.0151
0.0341	2.3	0.314 ± 0.0215	0.363 ± 0.0238	0.208 ± 0.0121	0.202 ± 0.0128
0.0341	2.5	0.326 ± 0.0235	0.415 ± 0.0346	0.211 ± 0.0157	0.177 ± 0.0112
0.0341	2.7	0.24 ± 0.019	0.32 ± 0.0268	0.163 ± 0.012	0.144 ± 0.0102
0.0341	2.9	0.26 ± 0.0251	0.265 ± 0.0229	0.149 ± 0.0115	0.15 ± 0.0132
0.0341	3.1	0.198 ± 0.0174	0.251 ± 0.0246	0.138 ± 0.0122	0.113 ± 0.00882
0.0341	3.3	0.234 ± 0.0268	0.237 ± 0.0249	0.129 ± 0.0121	0.133 ± 0.0141
0.0341	3.5	0.16 ± 0.0156	0.157 ± 0.0147	0.0913 ± 0.0073	0.0908 ± 0.00779
0.0341	3.7	0.144 ± 0.015	0.134 ± 0.0126	0.0755 ± 0.00581	0.0824 ± 0.00758
0.0341	3.9	0.133 ± 0.0154	0.117 ± 0.0109	0.0648 ± 0.00484	0.0756 ± 0.00786
0.0341	4.1	0.0875 ± 0.00825	0.129 ± 0.0154	0.088 ± 0.00974	0.0552 ± 0.00446
0.0341	4.3	0.123 ± 0.0166	0.0853 ± 0.00785	0.0508 ± 0.00367	0.0784 ± 0.00982
0.0341	4.5	0.102 ± 0.0125	0.0821 ± 0.00968	0.0582 ± 0.00622	0.052 ± 0.00522
0.0341	4.7	0.104 ± 0.0173	0.0841 ± 0.01	0.0527 ± 0.00548	0.065 ± 0.0102
0.0381	0.9	3.9e - 05 ± 2.25e - 05	3.9e - 05 ± 2.25e - 05	-1 ± -1	-1 ± -1
0.0381	1.1	0.266 ± 0.0235	0.284 ± 0.0256	0.17 ± 0.0145	0.159 ± 0.0133
0.0381	1.3	0.766 ± 0.044	0.721 ± 0.035	0.43 ± 0.0195	0.5 ± 0.0276
0.0381	1.5	0.584 ± 0.029	0.548 ± 0.0261	0.347 ± 0.0153	0.351 ± 0.0159
0.0381	1.7	0.437 ± 0.0212	0.549 ± 0.0322	0.339 ± 0.0185	0.262 ± 0.0113
0.0381	1.9	0.413 ± 0.0244	0.433 ± 0.0262	0.269 ± 0.015	0.247 ± 0.0133
0.0381	2.1	0.378 ± 0.0269	0.431 ± 0.0301	0.244 ± 0.0155	0.233 ± 0.0152
0.0381	2.3	0.305 ± 0.0203	0.301 ± 0.02	0.178 ± 0.0105	0.161 ± 0.00919
0.0381	2.5	0.282 ± 0.0227	0.273 ± 0.0198	0.159 ± 0.0102	0.157 ± 0.0113
0.0381	2.7	0.27 ± 0.0268	0.225 ± 0.0188	0.135 ± 0.0101	0.16 ± 0.0148
0.0381	2.9	0.218 ± 0.0187	0.26 ± 0.0248	0.138 ± 0.0117	0.106 ± 0.00759
0.0381	3.1	0.259 ± 0.0343	0.163 ± 0.0134	0.101 ± 0.00732	0.154 ± 0.0194
0.0381	3.3	0.247 ± 0.0322	0.16 ± 0.0153	0.0941 ± 0.00794	0.127 ± 0.0153
0.0381	3.5	0.13 ± 0.0136	0.16 ± 0.0163	0.0873 ± 0.00756	0.0819 ± 0.00772

Efficiencies from		LEPTO		PYTHIA	
		CTEQ2L	GRV98L	CTEQ2L	GRV94M
$x$	$Q^2$ [GeV/c <sup>2</sup> ]	$d^2\sigma/dxdQ^2$ [fb/(GeV/c <sup>2</sup> )]			
0.0381	3.7	0.125 ± 0.0124	0.135 ± 0.0148	0.0769 ± 0.00737	0.0659 ± 0.00537
0.0381	3.9	0.216 ± 0.0417	0.133 ± 0.0157	0.0745 ± 0.00767	0.127 ± 0.0237
0.0381	4.1	0.0822 ± 0.00832	0.133 ± 0.0177	0.0774 ± 0.00932	0.0509 ± 0.00442
0.0381	4.3	0.141 ± 0.0227	0.122 ± 0.0158	0.0605 ± 0.00665	0.069 ± 0.00996
0.0381	4.5	0.102 ± 0.0155	0.0835 ± 0.0113	0.0536 ± 0.00656	0.0679 ± 0.00975
0.0381	4.7	0.0943 ± 0.0143	0.0719 ± 0.00907	0.0483 ± 0.00539	0.0453 ± 0.00591
0.0421	1.3	0.392 ± 0.0257	0.443 ± 0.0296	0.254 ± 0.0159	0.244 ± 0.015
0.0421	1.5	0.536 ± 0.0341	0.549 ± 0.0338	0.333 ± 0.0193	0.338 ± 0.0205
0.0421	1.7	0.514 ± 0.0374	0.442 ± 0.0259	0.266 ± 0.0143	0.321 ± 0.0222
0.0421	1.9	0.325 ± 0.0192	0.386 ± 0.025	0.232 ± 0.0138	0.206 ± 0.0112
0.0421	2.1	0.371 ± 0.031	0.331 ± 0.0237	0.205 ± 0.0134	0.219 ± 0.0171
0.0421	2.3	0.336 ± 0.032	0.318 ± 0.0251	0.179 ± 0.0128	0.199 ± 0.0179
0.0421	2.5	0.22 ± 0.0179	0.271 ± 0.0244	0.153 ± 0.0125	0.126 ± 0.00917
0.0421	2.7	0.214 ± 0.0206	0.21 ± 0.0182	0.124 ± 0.00972	0.118 ± 0.0102
0.0421	2.9	0.223 ± 0.027	0.209 ± 0.0194	0.118 ± 0.00963	0.126 ± 0.0143
0.0421	3.1	0.158 ± 0.0154	0.158 ± 0.0148	0.0775 ± 0.00599	0.0804 ± 0.00679
0.0421	3.3	0.105 ± 0.00915	0.206 ± 0.0251	0.104 ± 0.0113	0.0638 ± 0.00465
0.0421	3.5	0.17 ± 0.0227	0.14 ± 0.0169	0.0839 ± 0.00924	0.0858 ± 0.0105
0.0421	3.7	0.122 ± 0.0153	0.142 ± 0.0174	0.0765 ± 0.00822	0.0732 ± 0.00838
0.0421	3.9	0.0793 ± 0.00775	0.12 ± 0.0137	0.0672 ± 0.00665	0.0474 ± 0.00382
0.0421	4.1	0.104 ± 0.0163	0.091 ± 0.0101	0.0507 ± 0.0045	0.069 ± 0.0103
0.0421	4.3	0.105 ± 0.0164	0.0816 ± 0.00937	0.0449 ± 0.0041	0.0591 ± 0.00851
0.0421	4.5	0.0731 ± 0.0101	0.0759 ± 0.011	0.0542 ± 0.00727	0.0522 ± 0.00674
0.0421	4.7	0.062 ± 0.0073	0.0685 ± 0.00967	0.0472 ± 0.00613	0.0373 ± 0.00364
0.0461	1.3	0.171 ± 0.0484	0.0571 ± 0.00452	0.0348 ± 0.00213	0.106 ± 0.0294
0.0461	1.5	0.474 ± 0.0376	0.442 ± 0.0322	0.283 ± 0.0197	0.294 ± 0.0223
0.0461	1.7	0.341 ± 0.0212	0.379 ± 0.0249	0.235 ± 0.0144	0.208 ± 0.0119
0.0461	1.9	0.328 ± 0.0249	0.375 ± 0.0319	0.216 ± 0.0173	0.198 ± 0.0141
0.0461	2.1	0.304 ± 0.0249	0.248 ± 0.0167	0.149 ± 0.00897	0.173 ± 0.013
0.0461	2.3	0.246 ± 0.0212	0.265 ± 0.0222	0.153 ± 0.0116	0.146 ± 0.0117
0.0461	2.5	0.252 ± 0.0239	0.291 ± 0.0299	0.168 ± 0.0159	0.142 ± 0.0124
0.0461	2.7	0.187 ± 0.0183	0.206 ± 0.0194	0.114 ± 0.00949	0.109 ± 0.0097
0.0461	2.9	0.199 ± 0.0249	0.227 ± 0.0258	0.123 ± 0.0128	0.117 ± 0.0138
0.0461	3.1	0.131 ± 0.0145	0.163 ± 0.0174	0.0924 ± 0.0088	0.0785 ± 0.00796
0.0461	3.3	0.161 ± 0.0229	0.137 ± 0.0148	0.0706 ± 0.00644	0.0869 ± 0.0114
0.0461	3.5	0.119 ± 0.0145	0.152 ± 0.019	0.0786 ± 0.00867	0.0632 ± 0.00672
0.0461	3.7	0.0982 ± 0.0103	0.126 ± 0.015	0.0659 ± 0.00654	0.0526 ± 0.0045
0.0461	3.9	0.12 ± 0.0187	0.097 ± 0.0104	0.0472 ± 0.0037	0.0694 ± 0.0101
0.0461	4.1	0.093 ± 0.0151	0.0761 ± 0.00916	0.0509 ± 0.00559	0.052 ± 0.0077
0.0461	4.3	0.0755 ± 0.01	0.127 ± 0.021	0.0615 ± 0.00895	0.0459 ± 0.00544
0.0461	4.5	0.0849 ± 0.0144	0.0782 ± 0.0112	0.0471 ± 0.00602	0.0541 ± 0.00854
0.0461	4.7	0.0627 ± 0.0113	0.0434 ± 0.00419	0.0299 ± 0.0023	0.0395 ± 0.00668
0.0501	1.5	0.165 ± 0.0175	0.205 ± 0.0209	0.12 ± 0.0114	0.114 ± 0.0116
0.0501	1.7	0.341 ± 0.0282	0.315 ± 0.0224	0.197 ± 0.0132	0.217 ± 0.0172
0.0501	1.9	0.25 ± 0.0174	0.264 ± 0.0195	0.174 ± 0.012	0.145 ± 0.00917
0.0501	2.1	0.212 ± 0.0165	0.251 ± 0.0207	0.15 ± 0.0114	0.131 ± 0.00949
0.0501	2.3	0.263 ± 0.0263	0.283 ± 0.0285	0.162 ± 0.0152	0.148 ± 0.0138
0.0501	2.5	0.24 ± 0.027	0.207 ± 0.0194	0.116 ± 0.00974	0.128 ± 0.0134
0.0501	2.7	0.207 ± 0.0252	0.175 ± 0.0161	0.0955 ± 0.00756	0.111 ± 0.0125
0.0501	2.9	0.153 ± 0.0171	0.192 ± 0.0212	0.0904 ± 0.00849	0.0824 ± 0.00832
0.0501	3.1	0.155 ± 0.0195	0.176 ± 0.0228	0.088 ± 0.0102	0.079 ± 0.00895
0.0501	3.3	0.173 ± 0.0289	0.109 ± 0.0121	0.0646 ± 0.00644	0.0953 ± 0.0151
0.0501	3.5	0.0697 ± 0.00675	0.117 ± 0.0152	0.0688 ± 0.00806	0.0472 ± 0.00403
0.0501	3.7	0.151 ± 0.0284	0.134 ± 0.0206	0.0689 ± 0.00957	0.0809 ± 0.0144
0.0501	3.9	0.0918 ± 0.0126	0.103 ± 0.0138	0.0472 ± 0.00509	0.0466 ± 0.00547
0.0501	4.1	0.0643 ± 0.00982	0.0813 ± 0.0107	0.046 ± 0.00518	0.0486 ± 0.00708
0.0501	4.3	0.0931 ± 0.0168	0.0926 ± 0.0157	0.0594 ± 0.00928	0.0598 ± 0.0102
0.0501	4.5	0.0705 ± 0.0107	0.0757 ± 0.0112	0.0444 ± 0.00572	0.0379 ± 0.00502
0.0501	4.7	0.0762 ± 0.0155	0.0867 ± 0.0138	0.0354 ± 0.00413	0.0491 ± 0.00956
0.054	1.3	1.3e - 05 ± 1.3e - 05	1.3e - 05 ± 1.3e - 05	-1 ± -1	-1 ± -1
0.054	1.5	-1 ± -1	0.00718 ± 0.000513	0.0056 ± 0.000199	-1 ± -1
0.054	1.7	0.315 ± 0.0382	0.226 ± 0.0182	0.137 ± 0.0102	0.191 ± 0.0224
0.054	1.9	0.295 ± 0.0296	0.262 ± 0.0224	0.154 ± 0.0123	0.17 ± 0.0162
0.054	2.1	0.275 ± 0.0303	0.254 ± 0.0235	0.152 ± 0.0131	0.166 ± 0.0175
0.054	2.3	0.184 ± 0.0154	0.167 ± 0.0139	0.11 ± 0.00845	0.105 ± 0.00791
0.054	2.5	0.138 ± 0.0113	0.2 ± 0.021	0.111 ± 0.0107	0.0802 ± 0.00579
0.054	2.7	0.172 ± 0.0201	0.219 ± 0.0287	0.126 ± 0.0155	0.0882 ± 0.00937
0.054	2.9	0.117 ± 0.0109	0.15 ± 0.0175	0.0818 ± 0.00844	0.059 ± 0.00454
0.054	3.1	0.152 ± 0.0228	0.0929 ± 0.00787	0.0526 ± 0.00341	0.0862 ± 0.0122
0.054	3.3	0.107 ± 0.0136	0.141 ± 0.0214	0.0794 ± 0.0112	0.062 ± 0.00713

Efficiencies from		LEPTO		PYTHIA	
		CTEQ2L	GRV98L	CTEQ2L	GRV94M
$x$	$Q^2$ [GeV/c <sup>2</sup> ]	$d^2\sigma/dxdQ^2$ [fb/(GeV/c <sup>2</sup> )]			
0.054	3.5	0.114 ± 0.0183	0.147 ± 0.0236	0.0744 ± 0.0108	0.0643 ± 0.00969
0.054	3.7	0.123 ± 0.0206	0.086 ± 0.0102	0.0516 ± 0.00538	0.0665 ± 0.0103
0.054	3.9	0.0988 ± 0.0172	0.076 ± 0.00921	0.0427 ± 0.00438	0.0549 ± 0.00878
0.054	4.1	0.0605 ± 0.00815	0.0954 ± 0.0159	0.0538 ± 0.00816	0.0335 ± 0.0039
0.054	4.3	0.0906 ± 0.0196	0.0711 ± 0.0101	0.0402 ± 0.00492	0.0617 ± 0.0129
0.054	4.5	0.0554 ± 0.00811	0.0581 ± 0.00758	0.0368 ± 0.00414	0.0317 ± 0.00402
0.054	4.7	0.0601 ± 0.01	0.0598 ± 0.0085	0.0413 ± 0.00524	0.0338 ± 0.00499
0.058	1.7	0.0778 ± 0.013	0.0858 ± 0.0137	0.0521 ± 0.00788	0.0439 ± 0.00691
0.058	1.9	0.202 ± 0.0199	0.267 ± 0.0261	0.147 ± 0.0135	0.122 ± 0.0114
0.058	2.1	0.279 ± 0.0385	0.224 ± 0.0227	0.132 ± 0.0125	0.163 ± 0.0218
0.058	2.3	0.161 ± 0.0159	0.201 ± 0.0222	0.122 ± 0.0126	0.098 ± 0.009
0.058	2.5	0.128 ± 0.0128	0.177 ± 0.0187	0.0963 ± 0.00927	0.0838 ± 0.0078
0.058	2.7	0.196 ± 0.0288	0.132 ± 0.0144	0.0826 ± 0.00831	0.106 ± 0.0148
0.058	2.9	0.178 ± 0.0305	0.18 ± 0.0271	0.0989 ± 0.0139	0.101 ± 0.0165
0.058	3.1	0.103 ± 0.0143	0.183 ± 0.027	0.0917 ± 0.0123	0.0616 ± 0.00795
0.058	3.3	0.135 ± 0.0238	0.0862 ± 0.00987	0.0511 ± 0.00511	0.0707 ± 0.0118
0.058	3.5	0.107 ± 0.0147	0.16 ± 0.0285	0.078 ± 0.0125	0.0525 ± 0.00619
0.058	3.7	0.0909 ± 0.0157	0.112 ± 0.0167	0.0549 ± 0.00715	0.0526 ± 0.00852
0.058	3.9	0.0716 ± 0.0109	0.0874 ± 0.0154	0.0507 ± 0.00811	0.041 ± 0.00563
0.058	4.1	0.0779 ± 0.0144	0.066 ± 0.00797	0.0303 ± 0.00232	0.0483 ± 0.00836
0.058	4.3	0.063 ± 0.0103	0.0773 ± 0.0131	0.0474 ± 0.00727	0.0322 ± 0.00447
0.058	4.5	0.0881 ± 0.0187	0.0567 ± 0.00863	0.035 ± 0.00461	0.0434 ± 0.00843
0.058	4.7	0.064 ± 0.012	0.036 ± 0.00379	0.0221 ± 0.00162	0.0355 ± 0.00603
0.062	1.9	0.153 ± 0.0225	0.237 ± 0.0389	0.13 ± 0.0204	0.0932 ± 0.0132
0.062	2.1	0.226 ± 0.0338	0.199 ± 0.0217	0.121 ± 0.0124	0.133 ± 0.0193
0.062	2.3	0.176 ± 0.0234	0.166 ± 0.0189	0.101 ± 0.0108	0.104 ± 0.0131
0.062	2.5	0.158 ± 0.0206	0.147 ± 0.0134	0.0718 ± 0.00534	0.091 ± 0.0112
0.062	2.7	0.117 ± 0.0128	0.115 ± 0.0118	0.0647 ± 0.00585	0.0646 ± 0.00643
0.062	2.9	0.172 ± 0.0299	0.116 ± 0.014	0.0614 ± 0.00648	0.0855 ± 0.0141
0.062	3.1	0.173 ± 0.0371	0.0943 ± 0.0115	0.0524 ± 0.00563	0.0887 ± 0.0182
0.062	3.3	0.0766 ± 0.0101	0.0902 ± 0.0112	0.0453 ± 0.00474	0.0496 ± 0.00598
0.062	3.5	0.122 ± 0.0252	0.121 ± 0.0222	0.0621 ± 0.0105	0.0725 ± 0.0144
0.062	3.7	0.118 ± 0.0219	0.072 ± 0.00989	0.0413 ± 0.00491	0.0579 ± 0.00975
0.062	3.9	0.0891 ± 0.0199	0.0651 ± 0.00898	0.0362 ± 0.0042	0.0562 ± 0.0121
0.062	4.1	0.0853 ± 0.0163	0.0843 ± 0.0146	0.039 ± 0.00569	0.0445 ± 0.00782
0.062	4.3	0.0545 ± 0.0101	0.0541 ± 0.00748	0.0298 ± 0.00336	0.0358 ± 0.00624
0.062	4.5	0.0624 ± 0.0126	0.0626 ± 0.0117	0.035 ± 0.00589	0.0329 ± 0.00608
0.062	4.7	0.0353 ± 0.00524	0.0351 ± 0.00421	0.022 ± 0.00195	0.0223 ± 0.00288
0.066	1.9	0.0424 ± 0.0127	0.0426 ± 0.0141	0.0271 ± 0.0086	0.0271 ± 0.00786
0.066	2.1	0.147 ± 0.0167	0.159 ± 0.0179	0.0843 ± 0.00859	0.0842 ± 0.00891
0.066	2.3	0.187 ± 0.0274	0.177 ± 0.0224	0.099 ± 0.0117	0.109 ± 0.0154
0.066	2.5	0.123 ± 0.0151	0.152 ± 0.0176	0.078 ± 0.00806	0.0721 ± 0.00834
0.066	2.7	0.158 ± 0.023	0.141 ± 0.0169	0.0672 ± 0.00692	0.0725 ± 0.00964
0.066	2.9	0.131 ± 0.0216	0.131 ± 0.0198	0.074 ± 0.0104	0.0714 ± 0.0111
0.066	3.1	0.193 ± 0.0468	0.119 ± 0.0185	0.0662 ± 0.00954	0.113 ± 0.0268
0.066	3.3	0.135 ± 0.0262	0.1 ± 0.0147	0.0512 ± 0.00662	0.0627 ± 0.0113
0.066	3.5	0.0373 ± 0.00225	0.0902 ± 0.0161	0.0616 ± 0.0105	0.0238 ± 0.000593
0.066	3.7	0.105 ± 0.0199	0.0824 ± 0.0141	0.0399 ± 0.00605	0.0431 ± 0.00736
0.066	3.9	0.0987 ± 0.0206	0.0576 ± 0.00909	0.0381 ± 0.00546	0.0414 ± 0.00776
0.066	4.1	0.0833 ± 0.0171	0.0662 ± 0.0121	0.0395 ± 0.00658	0.0445 ± 0.00847
0.066	4.3	0.0752 ± 0.0181	0.0561 ± 0.0103	0.0375 ± 0.00643	0.0415 ± 0.00944
0.066	4.5	0.0422 ± 0.0061	0.0361 ± 0.00468	0.0246 ± 0.00264	0.0223 ± 0.00259
0.066	4.7	0.0699 ± 0.0189	0.0511 ± 0.00893	0.0297 ± 0.0046	0.0405 ± 0.0104
0.07	2.1	0.0896 ± 0.0199	0.0447 ± 0.00322	0.0236 ± 0.00058	0.0514 ± 0.011
0.07	2.3	0.205 ± 0.0354	0.155 ± 0.0225	0.0907 ± 0.0126	0.111 ± 0.0185
0.07	2.5	0.179 ± 0.032	0.162 ± 0.0239	0.0852 ± 0.0118	0.1 ± 0.0173
0.07	2.7	0.11 ± 0.0162	0.0935 ± 0.0104	0.0572 ± 0.00574	0.0668 ± 0.00933
0.07	2.9	0.108 ± 0.0145	0.158 ± 0.0244	0.0695 ± 0.00947	0.0496 ± 0.00572
0.07	3.1	0.122 ± 0.0263	0.134 ± 0.0262	0.0782 ± 0.0145	0.0683 ± 0.0142
0.07	3.3	0.0749 ± 0.011	0.0952 ± 0.0163	0.0562 ± 0.00901	0.0342 ± 0.00431
0.07	3.5	0.114 ± 0.0282	0.0984 ± 0.0174	0.0459 ± 0.00716	0.0637 ± 0.0152
0.07	3.7	0.0527 ± 0.00849	0.0921 ± 0.018	0.0542 ± 0.00991	0.0327 ± 0.00491
0.07	3.9	0.0416 ± 0.00663	0.105 ± 0.0234	0.0496 ± 0.0101	0.0287 ± 0.00425
0.07	4.1	0.0393 ± 0.0062	0.0634 ± 0.0111	0.0356 ± 0.00534	0.028 ± 0.00412
0.07	4.3	0.0453 ± 0.00701	0.106 ± 0.0262	0.0441 ± 0.00993	0.0255 ± 0.00341
0.07	4.5	0.0626 ± 0.0155	0.038 ± 0.00546	0.0223 ± 0.00262	0.0363 ± 0.00856
0.07	4.7	0.0424 ± 0.00896	0.0246 ± 0.00257	0.0176 ± 0.00136	0.0286 ± 0.00564
0.074	2.1	-1 ± -1	0.0309 ± 0.027	0.0217 ± 0.0188	-1 ± -1
0.074	2.3	0.104 ± 0.0212	0.137 ± 0.0241	0.078 ± 0.0131	0.0655 ± 0.0129
0.074	2.5	0.094 ± 0.0108	0.117 ± 0.0148	0.0617 ± 0.00708	0.0519 ± 0.0054



Efficiencies from		LEPTO		PYTHIA	
		CTEQ2L	GRV98L	CTEQ2L	GRV94M
$x$	$Q^2$ [GeV/c <sup>2</sup> ]	$d^2\sigma/dx dQ^2$ [fb/(GeV/c <sup>2</sup> )]			
0.074	2.7	0.105 ± 0.0137	0.11 ± 0.0171	0.0687 ± 0.0101	0.0534 ± 0.00635
0.074	2.9	0.0593 ± 0.00656	0.103 ± 0.0178	0.0709 ± 0.0118	0.0368 ± 0.00362
0.074	3.1	0.106 ± 0.0257	0.112 ± 0.0173	0.0466 ± 0.00595	0.0589 ± 0.0138
0.074	3.3	0.0738 ± 0.0125	0.0929 ± 0.0165	0.0511 ± 0.00837	0.0396 ± 0.00621
0.074	3.5	0.0569 ± 0.00867	0.115 ± 0.0248	0.0652 ± 0.0133	0.0333 ± 0.00466
0.074	3.7	0.0776 ± 0.0177	0.0473 ± 0.00553	0.0232 ± 0.00183	0.0449 ± 0.00974
0.074	3.9	0.0613 ± 0.0133	0.0847 ± 0.0183	0.0402 ± 0.00774	0.0365 ± 0.00753
0.074	4.1	0.0705 ± 0.0171	0.0426 ± 0.00691	0.0259 ± 0.00357	0.034 ± 0.00766
0.074	4.3	0.0587 ± 0.0117	0.0439 ± 0.00683	0.0243 ± 0.0031	0.0271 ± 0.0046
0.074	4.5	0.0491 ± 0.00976	0.0289 ± 0.00355	0.0184 ± 0.00173	0.0292 ± 0.00538
0.074	4.7	0.0463 ± 0.0101	0.0601 ± 0.015	0.0383 ± 0.00908	0.026 ± 0.00515
0.078	2.3	0.192 ± 0.179	0.0558 ± 0.0181	0.032 ± 0.00993	0.096 ± 0.0889
0.078	2.5	0.208 ± 0.0572	0.0874 ± 0.0114	0.052 ± 0.00627	0.0879 ± 0.232
0.078	2.7	0.0786 ± 0.0108	0.116 ± 0.0186	0.0556 ± 0.00807	0.0448 ± 0.00569
0.078	2.9	0.0806 ± 0.0119	0.111 ± 0.0194	0.0549 ± 0.00888	0.0398 ± 0.0053
0.078	3.1	0.0971 ± 0.0227	0.0778 ± 0.0124	0.0453 ± 0.00659	0.0584 ± 0.0132
0.078	3.3	0.0769 ± 0.0144	0.0666 ± 0.0102	0.0369 ± 0.00492	0.0432 ± 0.0076
0.078	3.5	0.0656 ± 0.0108	0.0667 ± 0.0107	0.0338 ± 0.00471	0.0287 ± 0.004
0.078	3.7	0.0625 ± 0.0119	0.0502 ± 0.00853	0.0305 ± 0.00472	0.0285 ± 0.00475
0.078	3.9	0.0733 ± 0.0156	0.0439 ± 0.00627	0.0236 ± 0.0027	0.0364 ± 0.00718
0.078	4.1	0.0353 ± 0.0043	0.0304 ± 0.00422	0.0201 ± 0.00233	0.0173 ± 0.00139
0.078	4.3	0.0482 ± 0.0129	0.065 ± 0.0157	0.0366 ± 0.00827	0.0311 ± 0.00807
0.078	4.5	0.078 ± 0.0255	0.046 ± 0.00899	0.0232 ± 0.00387	0.0438 ± 0.0138
0.078	4.7	0.0392 ± 0.0071	0.0968 ± 0.0288	0.0464 ± 0.0129	0.0173 ± 0.0023
0.082	2.5	0.0898 ± 0.0271	0.0581 ± 0.00825	0.0291 ± 0.00342	0.0421 ± 0.0122
0.082	2.7	0.151 ± 0.0376	0.15 ± 0.0335	0.0823 ± 0.0177	0.0805 ± 0.0194
0.082	2.9	0.0977 ± 0.0205	0.105 ± 0.0197	0.0557 ± 0.00963	0.0548 ± 0.011
0.082	3.1	0.118 ± 0.0368	0.103 ± 0.0178	0.0432 ± 0.00653	0.0686 ± 0.021
0.082	3.3	0.0584 ± 0.00898	0.0627 ± 0.00979	0.03 ± 0.00395	0.0288 ± 0.00385
0.082	3.5	0.0758 ± 0.0161	0.0567 ± 0.0109	0.033 ± 0.00593	0.0409 ± 0.00819
0.082	3.7	0.0956 ± 0.0317	0.0592 ± 0.0112	0.0335 ± 0.00573	0.0665 ± 0.0217
0.082	3.9	0.0775 ± 0.0207	0.0438 ± 0.00763	0.0261 ± 0.00412	0.0375 ± 0.0095
0.082	4.1	0.0679 ± 0.0194	0.0757 ± 0.018	0.0362 ± 0.00764	0.0373 ± 0.0101
0.082	4.3	0.0488 ± 0.0122	0.0343 ± 0.00452	0.0162 ± 0.00116	0.0259 ± 0.00604
0.082	4.5	0.0524 ± 0.0132	0.0448 ± 0.00911	0.0222 ± 0.00386	0.0259 ± 0.00599
0.082	4.7	0.0208 ± 0.002	0.0343 ± 0.00758	0.0234 ± 0.00479	0.0129 ± 0.000428
0.086	2.5	0.0323 ± 0.0182	0.0265 ± 0.00887	0.0113 ± 0.00331	0.0189 ± 0.0104
0.086	2.7	0.0635 ± 0.00956	0.0826 ± 0.0151	0.0408 ± 0.00676	0.0311 ± 0.00409
0.086	2.9	0.0953 ± 0.0196	0.122 ± 0.0254	0.0732 ± 0.0145	0.0533 ± 0.0105
0.086	3.1	0.058 ± 0.0105	0.0624 ± 0.0099	0.0319 ± 0.00446	0.0326 ± 0.0055
0.086	3.3	0.0915 ± 0.0286	0.119 ± 0.0285	0.0496 ± 0.011	0.0587 ± 0.0179
0.086	3.5	0.0551 ± 0.0133	0.122 ± 0.0342	0.0603 ± 0.016	0.0287 ± 0.00659
0.086	3.7	0.0959 ± 0.0289	0.113 ± 0.0314	0.0496 ± 0.0129	0.0496 ± 0.0144
0.086	3.9	0.0418 ± 0.00708	0.107 ± 0.0477	0.067 ± 0.0296	0.0202 ± 0.00284
0.086	4.1	0.0421 ± 0.0104	0.0677 ± 0.0163	0.0317 ± 0.00679	0.023 ± 0.00529
0.086	4.3	0.0354 ± 0.00741	0.0523 ± 0.0143	0.0329 ± 0.00851	0.0185 ± 0.00347
0.086	4.5	0.0492 ± 0.0164	0.0209 ± 0.00195	0.0132 ± 0.000755	0.0251 ± 0.00799
0.086	4.7	0.0302 ± 0.00592	0.0697 ± 0.0206	0.0363 ± 0.00995	0.0151 ± 0.00244
0.09	2.7	0.0563 ± 0.023	0.0401 ± 0.0121	0.0252 ± 0.00733	0.0347 ± 0.0139
0.09	2.9	0.141 ± 0.0402	0.0591 ± 0.00979	0.0322 ± 0.00479	0.0701 ± 0.0193
0.09	3.1	0.0392 ± 0.00573	0.0637 ± 0.0112	0.0377 ± 0.00611	0.028 ± 0.00384
0.09	3.3	0.0956 ± 0.0272	0.058 ± 0.011	0.0401 ± 0.00727	0.0486 ± 0.0134
0.09	3.5	0.0458 ± 0.00844	0.0448 ± 0.00775	0.0263 ± 0.00408	0.0214 ± 0.00345
0.09	3.7	0.0449 ± 0.00946	0.0482 ± 0.00746	0.0197 ± 0.00215	0.0249 ± 0.00489
0.09	3.9	0.0628 ± 0.0175	0.0767 ± 0.0226	0.0355 ± 0.0098	0.0302 ± 0.00783
0.09	4.1	0.0311 ± 0.0043	0.0441 ± 0.00888	0.0255 ± 0.00459	0.0157 ± 0.00158
0.09	4.3	0.0571 ± 0.0238	0.0211 ± 0.0026	0.0149 ± 0.0014	0.0377 ± 0.0154
0.09	4.5	0.081 ± 0.042	0.0335 ± 0.00698	0.0197 ± 0.00367	0.0553 ± 0.0283
0.09	4.7	0.073 ± 0.0372	0.0301 ± 0.00451	0.0115 ± 0.000402	0.0459 ± 0.023
0.094	2.5	3.9e - 05 ± 2.25e - 05	3.9e - 05 ± 2.25e - 05	-1 ± -1	-1 ± -1
0.094	2.9	0.097 ± 0.0373	0.108 ± 0.0361	0.0581 ± 0.0187	0.0553 ± 0.0209
0.094	3.1	0.053 ± 0.0109	0.0462 ± 0.00802	0.0264 ± 0.00418	0.031 ± 0.00606
0.094	3.3	0.0698 ± 0.018	0.0498 ± 0.011	0.0326 ± 0.00685	0.032 ± 0.0078
0.094	3.5	0.031 ± 0.00501	0.0327 ± 0.00407	0.0184 ± 0.00185	0.0186 ± 0.0027
0.094	3.7	0.0291 ± 0.00563	0.0416 ± 0.00823	0.0229 ± 0.00407	0.0186 ± 0.00336
0.094	3.9	0.0546 ± 0.0156	0.0418 ± 0.00799	0.0237 ± 0.00405	0.0273 ± 0.00736
0.094	4.1	0.034 ± 0.00749	0.0385 ± 0.00857	0.0222 ± 0.00455	0.019 ± 0.00383
0.094	4.3	0.0551 ± 0.0177	0.0315 ± 0.00482	0.0127 ± 0.000927	0.0237 ± 0.0069
0.094	4.5	0.0419 ± 0.0134	0.0249 ± 0.00339	0.0107 ± 0.000375	0.0265 ± 0.00824
0.094	4.7	0.0292 ± 0.00602	0.126 ± 0.0843	0.0821 ± 0.0541	0.0146 ± 0.00249

## A.2 Trigger Dependent Analysis

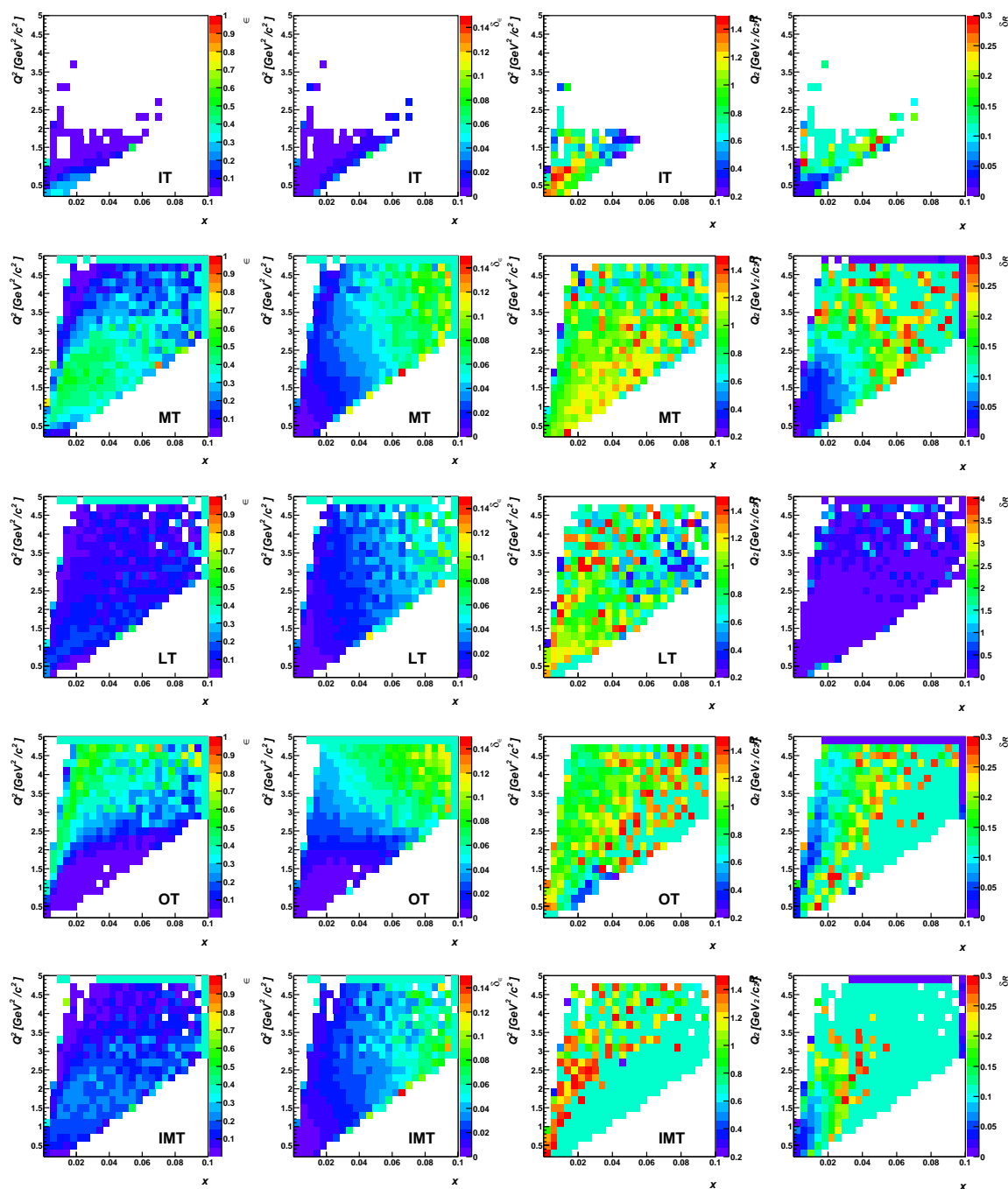


Figure A.1: Trigger dependent analysis for PYTHIA (std); from left to right: efficiency, error of the efficiency, ratio of the cross section with the generator cross section, error on the ratio; from top to bottom: Inner Trigger, Middle Trigger, Ladder Trigger, Outer Trigger, Inclusive Middle Trigger

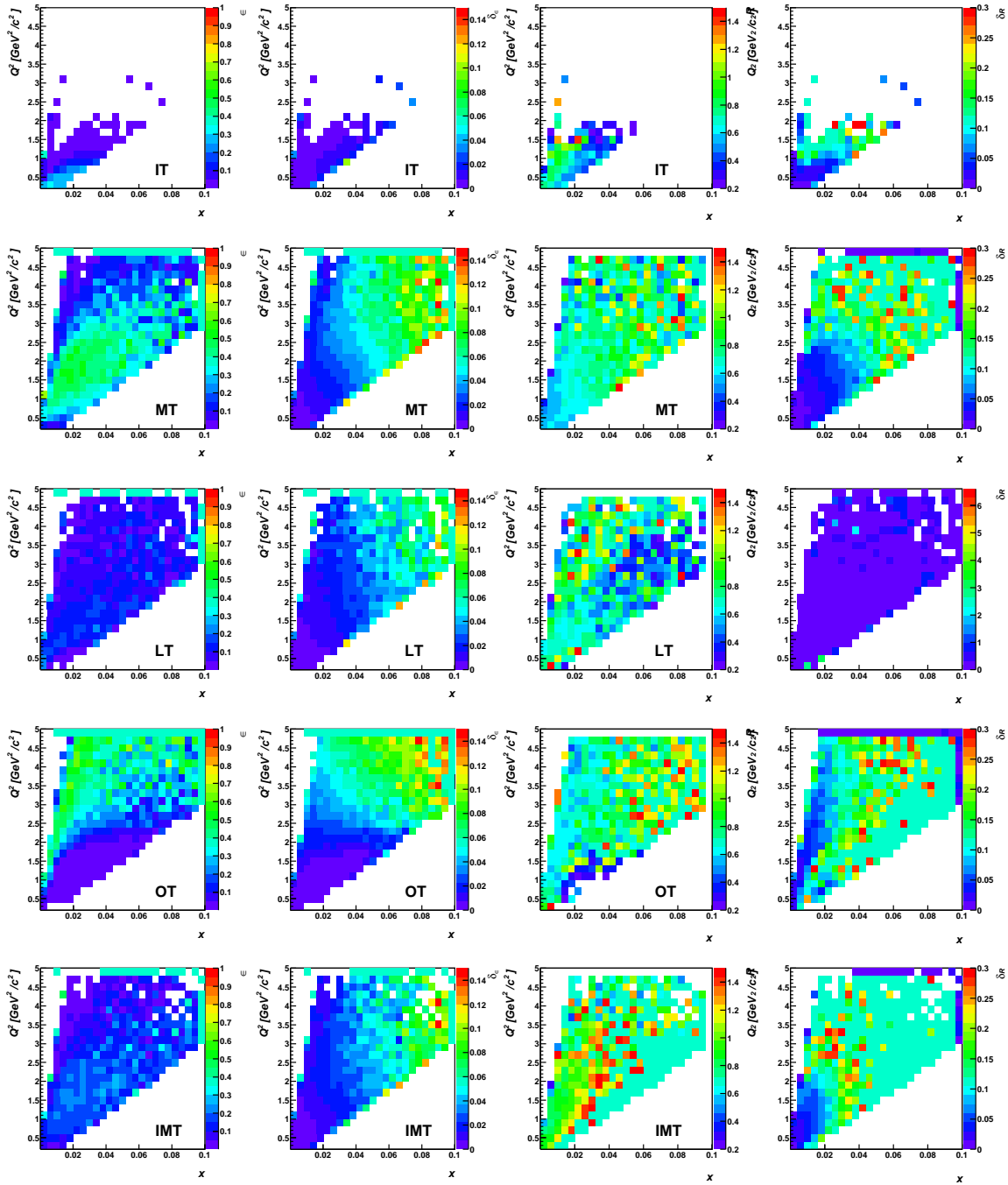


Figure A.2: Trigger dependent analysis for PYTHIA (GRV94L); from left to right: efficiency, error of the efficiency, ratio of the cross section with the generator cross section, error on the ratio; from top to bottom: Inner Trigger, Middle Trigger, Ladder Trigger, Outer Trigger, Inclusive Middle Trigger

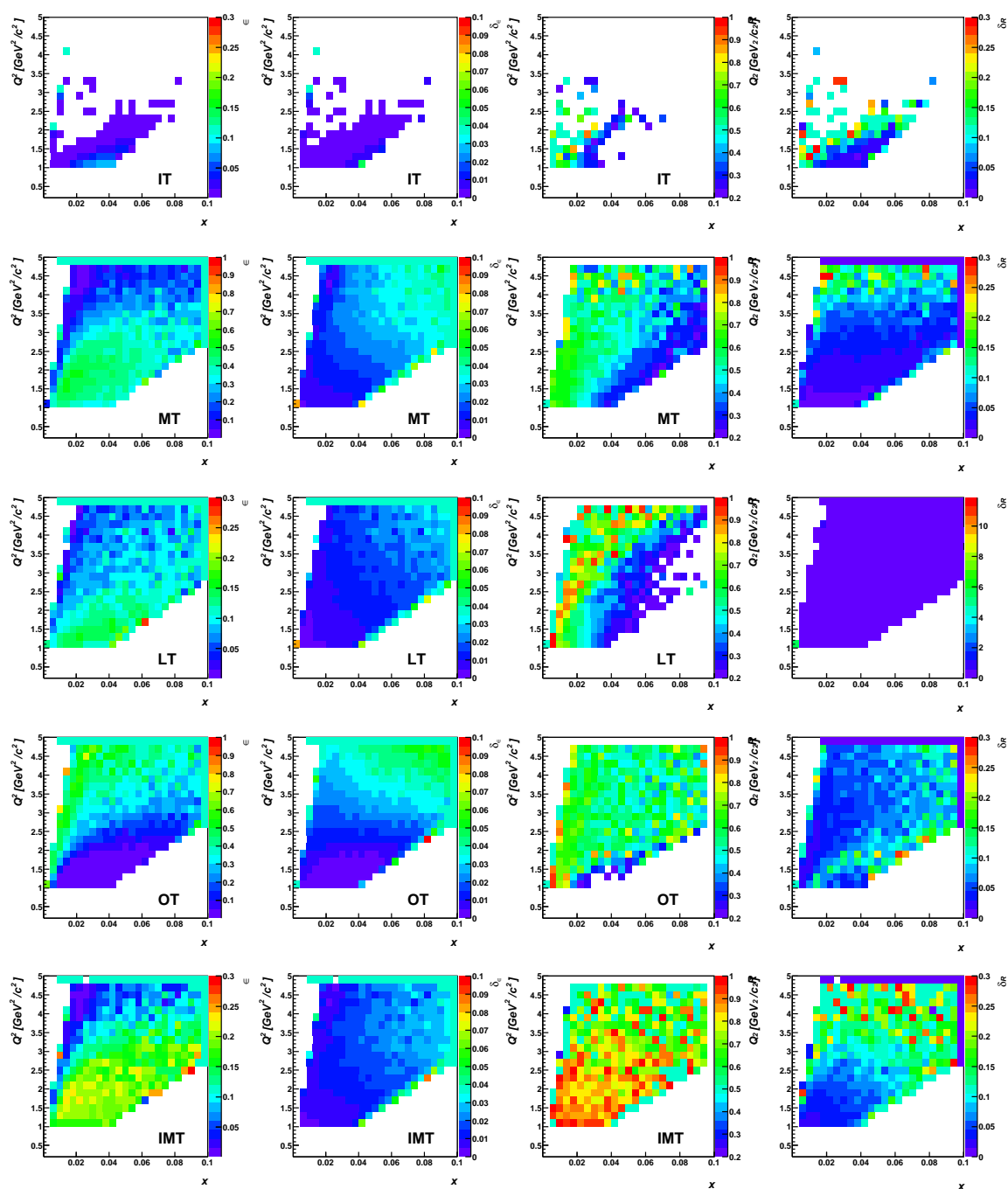


Figure A.3: Trigger dependent analysis for LEPTO (std.); from left to right: efficiency, error of the efficiency, ratio of the cross section with the generator cross section, error on the ratio; from top to bottom: Inner Trigger, Middle Trigger, Ladder Trigger, Outer Trigger, Inclusive Middle Trigger

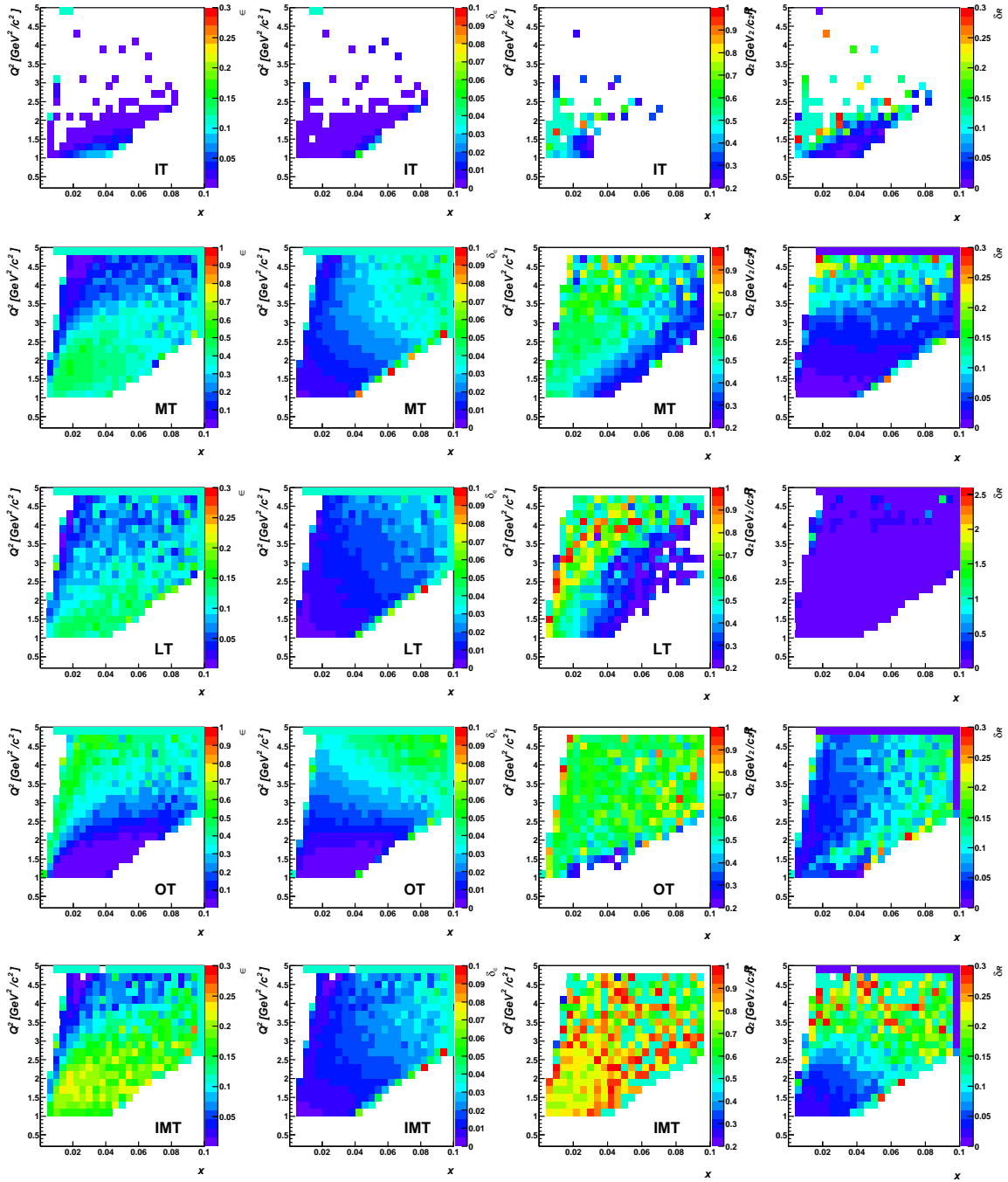


Figure A.4: Trigger dependent analysis for LEPTO (GRV98M); from left to right: efficiency, error of the efficiency, ratio of the cross section with the generator cross section, error on the ratio; from top to bottom: Inner Trigger, Middle Trigger, Ladder Trigger, Outer Trigger, Inclusive Middle Trigger

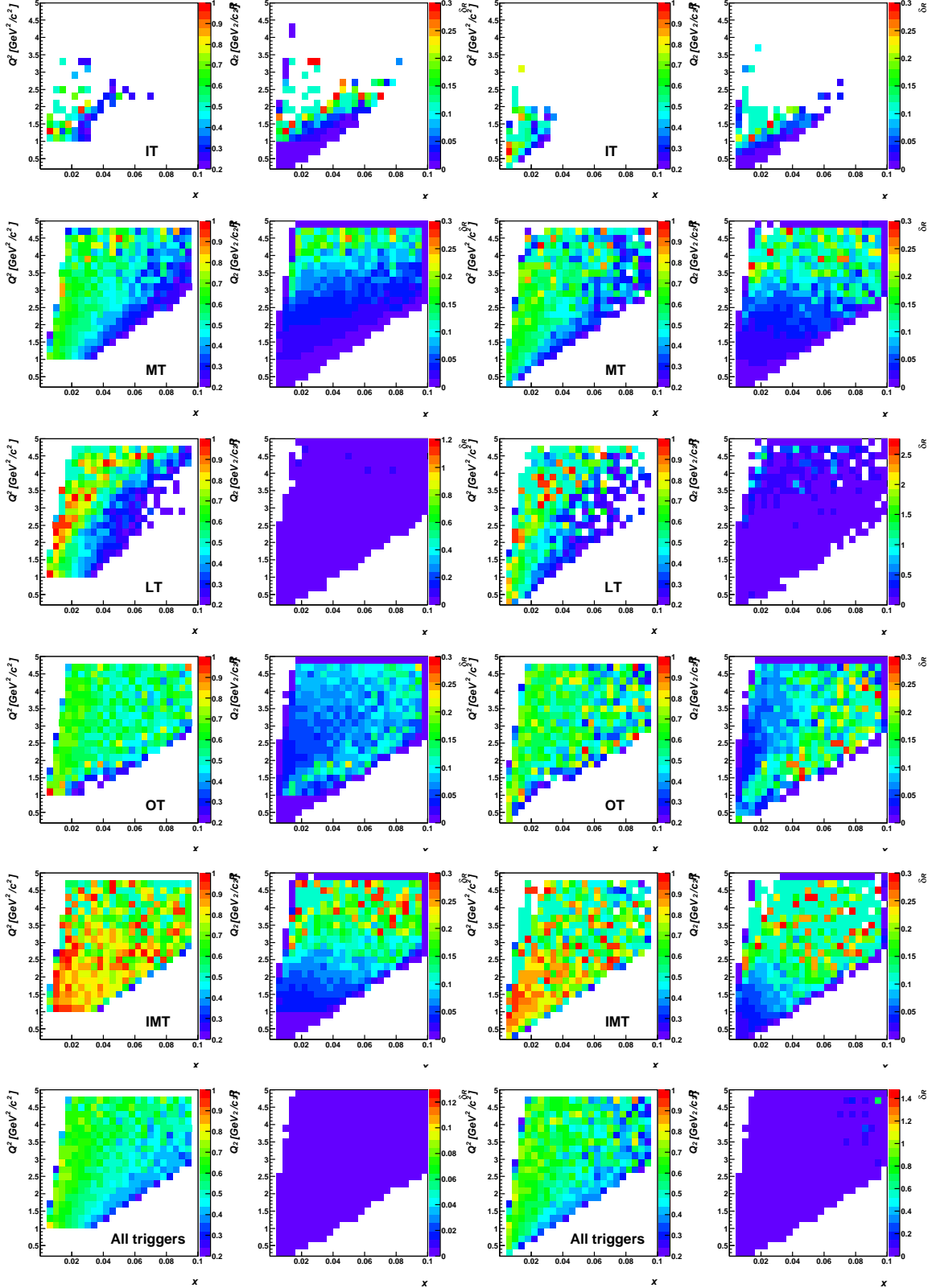


Figure A.5: Trigger dependent comparison of the cross section to NMC using the efficiencies from LEPTO and PYTHIA with default parameters; left to right: ratio of the cross section with LEPTO efficiency divided by NMC and statistical error, ratio of the cross section with PYTHIA efficiency divided by NMC and statistical error; from top to bottom: Inner Trigger, Middle Trigger, Ladder Trigger, Outer Trigger, Inclusive Middle Trigger

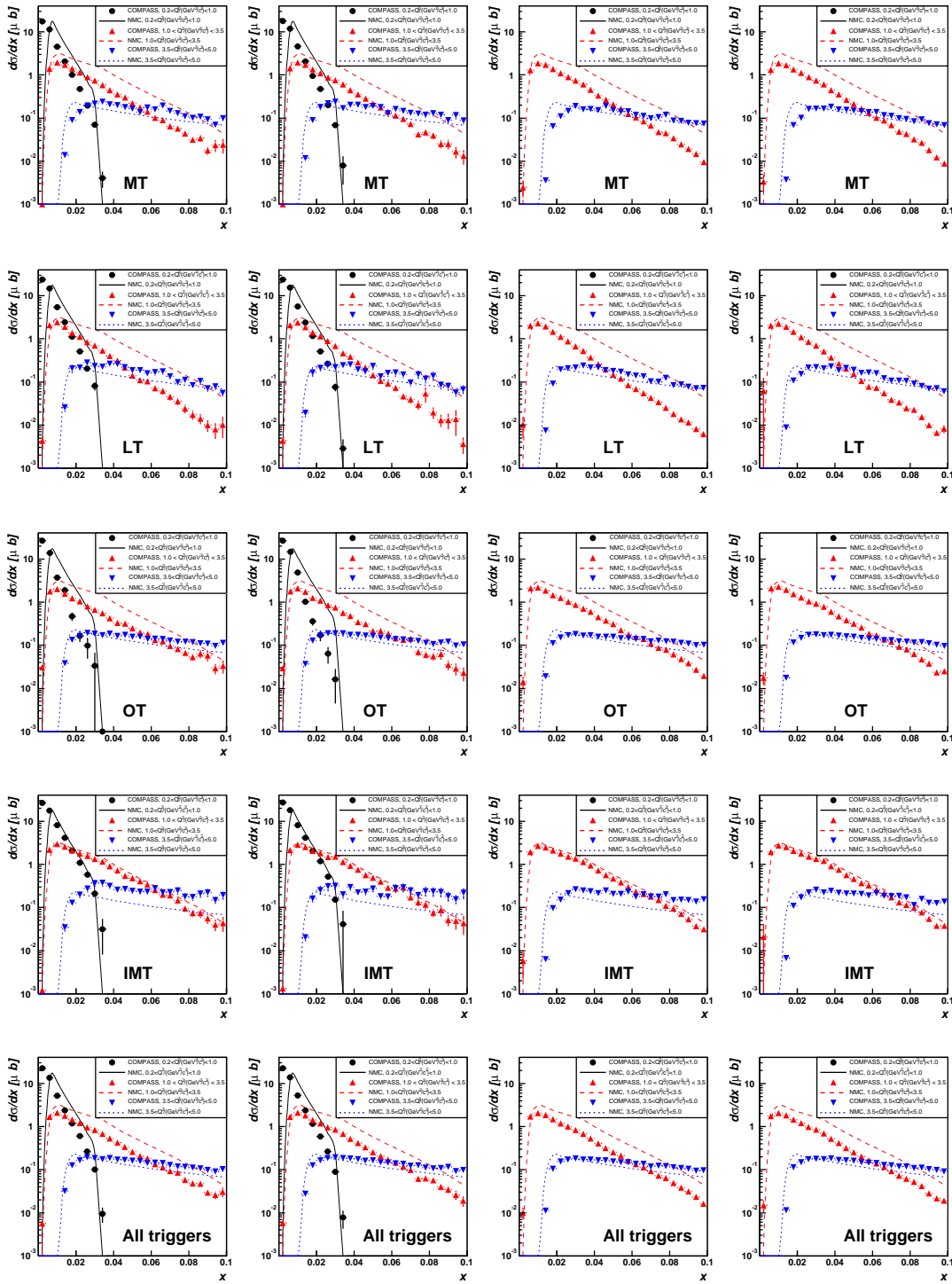


Figure A.6:  $\frac{d\sigma}{dx}$  from COMPASS data in comparison to the NMC results; from left to right: efficiencies from PYTHIA CTEQ5L, PYTHIA GRV94M, LEPTO CTEQ2L, LEPTO CTEQ2L; from top to bottom: Middle Trigger, Ladder Trigger, Outer Trigger, Inclusive Middle Trigger, all triggers;



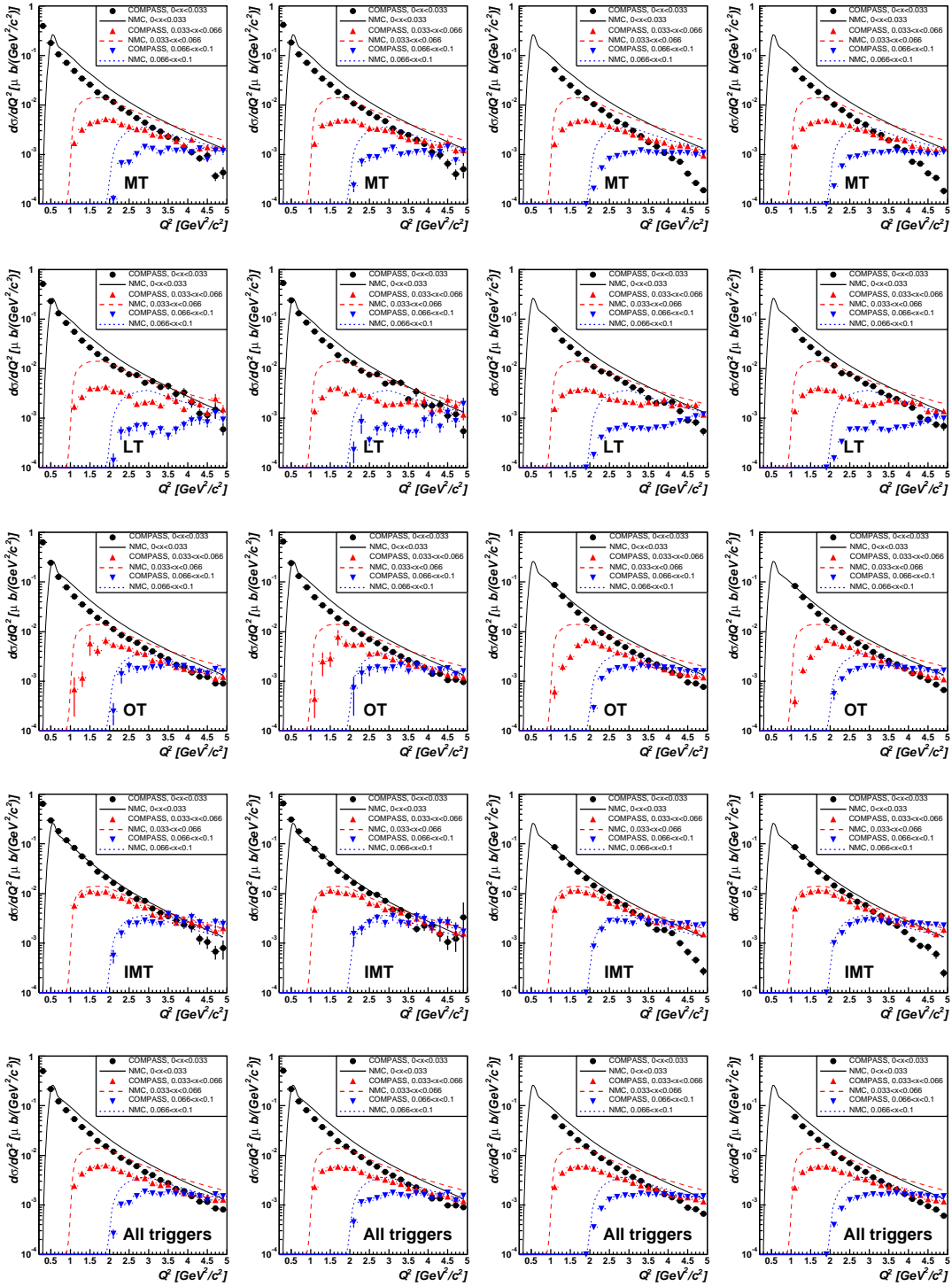


Figure A.7:  $\frac{d\sigma}{dQ^2}$  from COMPASS data in comparison to the NMC results; from left to right: efficiencies from PYTHIA CTEQ5L, PYTHIA GRV94M, LEPTO CTEQ2L, LEPTO CTEQ2L; from top to bottom: Middle Trigger, Ladder Trigger, Outer Trigger, Inclusive Middle Trigger, all triggers;



# Appendix B

## Semi-inclusive Cross Section Additives

### B.1 Data Monte Carlo Comparison for 2002

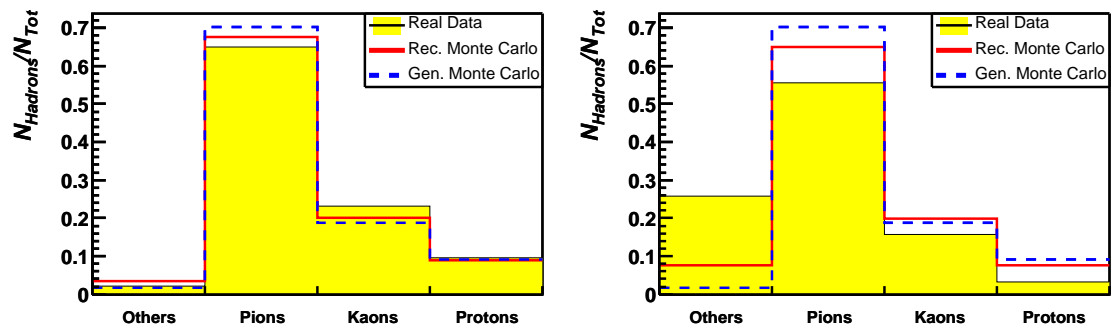


Figure B.1: Particle identification for all 2002 data and Monte Carlo; LLH method (left) and  $\chi^2$  method (right)

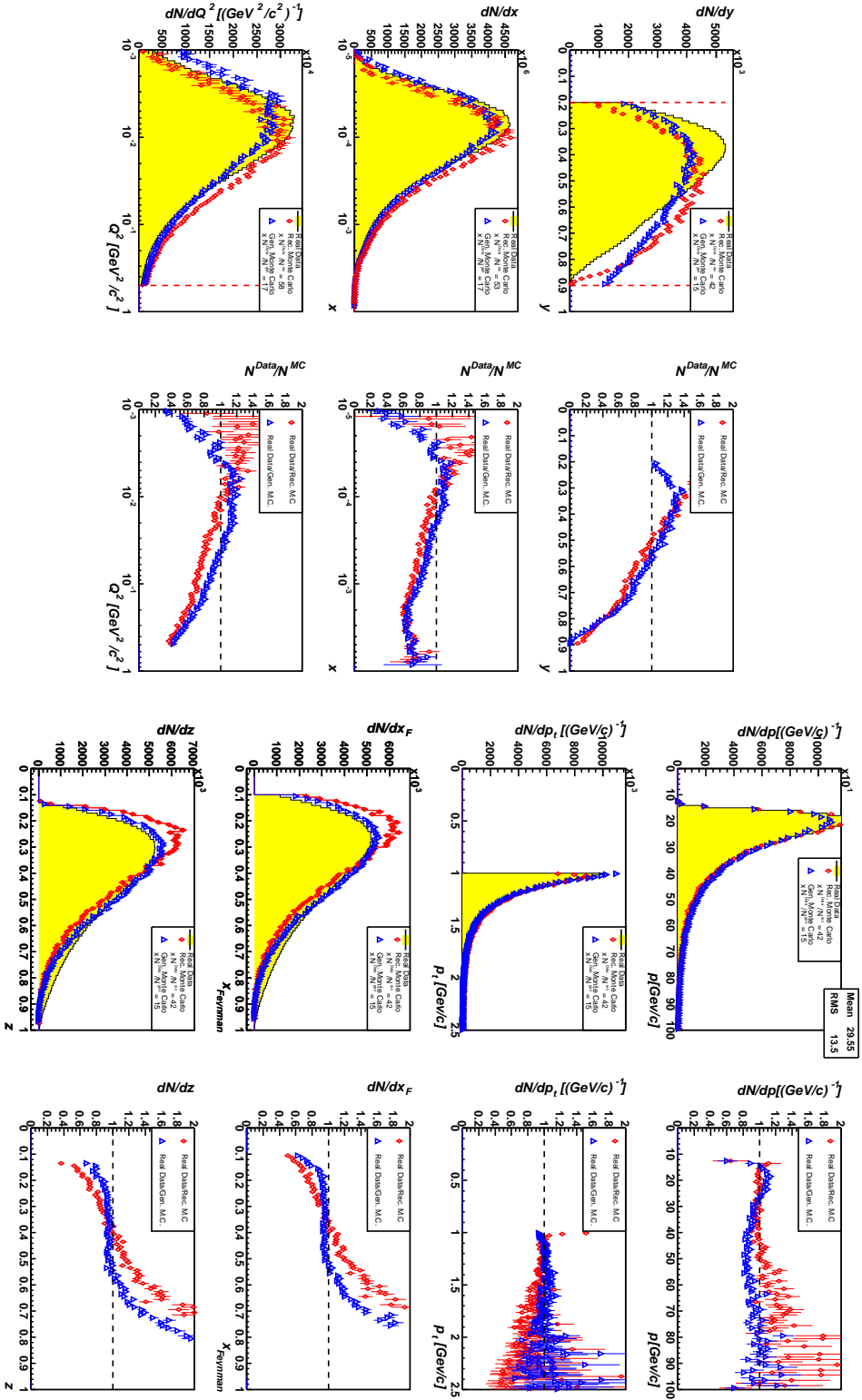


Figure B.2: Comparison of kinematic distributions  $p$  (top),  $p_t$  (second row),  $x_{Feynman}$  (third row),  $z$  (bottom) for semi-inclusive events in real data with Monte Carlo; a direct comparison (left column) and Monte Carlo data is scaled with a factor  $f = \frac{N_{Data}}{N_{MC}}$  (right column) are shown; Monte Carlo data is scaled with a factor  $f = \frac{N_{Data}}{N_{MC}}$

## **B.2 Numerical Results for the Semi-Inclusive Cross Section**

$p_T^{\text{down}} [\text{GeV}/c^2]$	$p_T^{\text{up}} [\text{GeV}/c^2]$	All hadrons	$\chi^2$	$\pi^+$ , $\pi^-$	DLH	$\chi^2$	$K^+$ , $K^-$	DLH	$\chi^2$	$p, \bar{p}$	DLH
1	1.1	$5.73e+04 \pm 489$	$3.56e+04 \pm 369$	$3.99e+04 \pm 407$	$7.81e+03 \pm 155$	$1.11e+04 \pm 214$	$2.23e+03 \pm 75.1$	$6.23e+03 \pm 192$			
1.1	1.2	$3.08e+04 \pm 329$	$1.84e+04 \pm 241$	$2.08e+04 \pm 267$	$4.54e+03 \pm 111$	$6.62e+03 \pm 160$	$1.35e+03 \pm 55.3$	$3.23e+03 \pm 118$			
1.2	1.3	$1.86e+04 \pm 253$	$1.1e+04 \pm 186$	$1.24e+04 \pm 205$	$2.82e+03 \pm 86.6$	$4.11e+03 \pm 126$	$740 \pm 35.7$	$1.83e+03 \pm 82.1$			
1.3	1.4	$1.11e+04 \pm 192$	$6.37e+03 \pm 137$	$7.1e+03 \pm 150$	$1.82e+03 \pm 69.7$	$2.67e+03 \pm 103$	$442 \pm 25.4$	$1.15e+03 \pm 64$			
1.4	1.5	$6.75e+03 \pm 148$	$3.81e+03 \pm 105$	$4.3e+03 \pm 117$	$1.18e+03 \pm 56.6$	$1.74e+03 \pm 84.8$	$257 \pm 18.1$	$600 \pm 39.9$			
1.5	1.6	$4.18e+03 \pm 115$	$2.41e+03 \pm 83.6$	$2.75e+03 \pm 94.5$	$718 \pm 42.6$	$1.09e+03 \pm 66.5$	$140 \pm 11.7$	$358 \pm 29.3$			
1.6	1.7	$2.48e+03 \pm 84.4$	$1.42e+03 \pm 62.7$	$1.59e+03 \pm 68.7$	$444 \pm 32.2$	$662 \pm 48.9$	$80.8 \pm 8.37$	$192 \pm 19.3$			
1.7	1.8	$1.54e+03 \pm 65.1$	$861 \pm 46.6$	$984 \pm 52.5$	$265 \pm 23.7$	$417 \pm 38.6$	$41.2 \pm 5.4$	$127 \pm 17.2$			
1.8	1.9	$976 \pm 50.2$	$529 \pm 35.1$	$608 \pm 39.6$	$181 \pm 19.6$	$297 \pm 33.5$	$26.9 \pm 4.4$	$72.6 \pm 11.8$			
1.9	2	$604 \pm 39.3$	$302 \pm 25.2$	$356 \pm 29.5$	$113 \pm 15.8$	$230 \pm 36.3$	$21.6 \pm 4.17$	$49 \pm 8.91$			
2	2.1	$393 \pm 32.7$	$205 \pm 22.1$	$242 \pm 25.7$	$58.9 \pm 9.92$	$108 \pm 19.2$	$13.7 \pm 3.51$	$49.3 \pm 13.6$			
2.1	2.2	$238 \pm 24.5$	$128 \pm 17.8$	$144 \pm 19.4$	$43.7 \pm 9.23$	$73.8 \pm 16$	$3.97 \pm 1.2$	$16.7 \pm 5.38$			
2.2	2.3	$157 \pm 19$	$86.1 \pm 14.2$	$99.1 \pm 15.7$	$20 \pm 4.4$	$45 \pm 11$	$5.12 \pm 2.45$	$13.2 \pm 5.76$			
2.3	2.4	$99.4 \pm 14.8$	$50.6 \pm 10.3$	$56.7 \pm 10.9$	$20.1 \pm 6.78$	$42.1 \pm 15.5$	$1.4 \pm 0.549$	$7.57 \pm 3.27$			
2.4	2.5	$58.4 \pm 11.8$	$23.1 \pm 5.95$	$28.7 \pm 7.17$	$11.3 \pm 5.23$	$22.8 \pm 11.1$	$0.927 \pm 0.61$	$3.02 \pm 1.96$			
2.5	2.6	$51.3 \pm 15.2$	$55.2 \pm 29.4$	$49.3 \pm 22$	$4.57 \pm 2.7$	$13.8 \pm 9.53$	$0.12 \pm 0.13$	$0.773 \pm 0.848$			
2.6	2.7	$26.3 \pm 8.16$	$6.5 \pm 2.44$	$10.4 \pm 3.99$	$4.42 \pm 2.77$	$10.3 \pm 6.22$	$0 \pm 0$	$0 \pm 0$			
2.7	2.8	$20.7 \pm 8.57$	$5.56 \pm 2.96$	$11.5 \pm 6.59$	$3.4 \pm 2.77$	$14.4 \pm 15.4$	$0 \pm 0$	$0 \pm 0$			
2.8	2.9	$15 \pm 7.88$	$5.15 \pm 3.45$	$6.92 \pm 4.61$	$3.71 \pm 4.19$	$7.5 \pm 8.43$	$0 \pm 0$	$0 \pm 0$			
2.9	3	$7.28 \pm 4.03$	$1.41 \pm 1.03$	$8.34 \pm 9.07$	$1.02 \pm 1.26$	$2.34 \pm 2.88$	$0.177 \pm 0.257$	$0.419 \pm 0.518$			
3	3.1	$1.47 \pm 1.8$	$0.64 \pm 0.913$	$0.53 \pm 0.653$	$0 \pm 0$	$0 \pm 0$	$0 \pm 0$	$0 \pm 0$			
3.1	3.2	$3.35 \pm 4.13$	$0.199 \pm 0.289$	$0 \pm 0$	$0 \pm 0$	$0 \pm 0$	$0 \pm 0$	$0.441 \pm 0.632$			
3.2	3.3	$0.848 \pm 0.582$	$0 \pm 0$	$0 \pm 0$	$0.0441 \pm 0.0541$	$0.265 \pm 0.276$	$0 \pm 0$	$0.199 \pm 0.289$			
3.3	3.4	$1.7 \pm 1.21$	$0.132 \pm 0.138$	$0 \pm 0$	$0.132 \pm 0.179$	$0.43 \pm 0.411$	$0 \pm 0$	$0 \pm 0$			
3.4	3.5	$0.75 \pm 0.937$	$0 \pm 0$	$0 \pm 0$	$0 \pm 0$	$0 \pm 0$	$0 \pm 0$	$0 \pm 0$			
3.5	3.6	$0.662 \pm 0.829$	$0 \pm 0$	$0 \pm 0$	$0 \pm 0$	$0 \pm 0$	$0 \pm 0$	$0 \pm 0$			
3.8	3.9	$0.11 \pm 0.164$	$0 \pm 0$	$0 \pm 0$	$0 \pm 0$	$0 \pm 0$	$0 \pm 0$	$0 \pm 0$			

Table B.1: Numerical results for the cross section for semi-inclusive high- $p_T$  hadron production from 2002 data

$p_t^{\text{down}} [\text{GeV}/c^2]$	$p_t^{\text{up}} [\text{GeV}/c^2]$	All hadrons	$\chi^2$	$\pi^+, \pi^-, \pi^0$	LLH	$\chi^2$	$K^+, K^-, K^0$	LLH	$\chi^2$	$p, \bar{p}$	LLH
1	1.1	$8e \pm 04 \pm 790$	$5.79e \pm 04 \pm 702$	$5.8e \pm 04 \pm 682$	$1.3e \pm 04 \pm 294$	$1.54e \pm 04 \pm 340$	$3.96e \pm 03 \pm 150$	$7.54e \pm 03 \pm 287$			
1.1	1.2	$4.36e \pm 04 \pm 537$	$3e \pm 04 \pm 455$	$3.08e \pm 04 \pm 456$	$7.62e \pm 03 \pm 211$	$8.87e \pm 03 \pm 241$	$2.44e \pm 03 \pm 111$	$4.33e \pm 03 \pm 194$			
1.2	1.3	$2.69e \pm 04 \pm 425$	$1.81e \pm 04 \pm 355$	$1.82e \pm 04 \pm 347$	$4.9e \pm 03 \pm 173$	$5.98e \pm 03 \pm 212$	$1.49e \pm 03 \pm 79.7$	$2.83e \pm 03 \pm 156$			
1.3	1.4	$1.61e \pm 04 \pm 325$	$1.09e \pm 04 \pm 275$	$1.11e \pm 04 \pm 273$	$2.95e \pm 03 \pm 130$	$3.75e \pm 03 \pm 168$	$804 \pm 51.3$	$1.47e \pm 03 \pm 95.6$			
1.4	1.5	$1e \pm 04 \pm 258$	$6.39e \pm 03 \pm 208$	$6.59e \pm 03 \pm 210$	$1.96e \pm 03 \pm 107$	$2.46e \pm 03 \pm 136$	$521 \pm 43.3$	$911 \pm 76.3$			
1.5	1.6	$5.94e \pm 03 \pm 185$	$3.68e \pm 03 \pm 144$	$3.89e \pm 03 \pm 150$	$1.16e \pm 03 \pm 78$	$1.43e \pm 03 \pm 96.6$	$305 \pm 29.7$	$601 \pm 61.3$			
1.6	1.7	$3.67e \pm 03 \pm 143$	$2.29e \pm 03 \pm 115$	$2.34e \pm 03 \pm 114$	$744 \pm 59.6$	$1.02e \pm 03 \pm 84.8$	$143 \pm 17.5$	$329 \pm 44.2$			
1.7	1.8	$2.44e \pm 03 \pm 121$	$1.62e \pm 03 \pm 98.4$	$1.64e \pm 03 \pm 105$	$465 \pm 47.1$	$650 \pm 68$	$88.7 \pm 12.7$	$161 \pm 23.2$			
1.8	1.9	$1.4e \pm 03 \pm 86.6$	$813 \pm 64.2$	$933 \pm 74.2$	$345 \pm 46.8$	$425 \pm 56.7$	$41.2 \pm 7.14$	$105 \pm 19.8$			
1.9	2	$1e \pm 03 \pm 78.1$	$563 \pm 56.8$	$640 \pm 64.3$	$211 \pm 33$	$338 \pm 56.5$	$28 \pm 6.92$	$65.3 \pm 16.8$			
2	2.1	$633 \pm 61.6$	$325 \pm 40.5$	$396 \pm 50.3$	$134 \pm 26.1$	$204 \pm 41.3$	$23.3 \pm 7.68$	$69.4 \pm 25.6$			
2.1	2.2	$346 \pm 40$	$172 \pm 26.4$	$210 \pm 32.5$	$77.7 \pm 17.2$	$135 \pm 32.4$	$13.2 \pm 4.58$	$27 \pm 8.94$			
2.2	2.3	$211 \pm 31.6$	$104 \pm 21.9$	$122 \pm 25.4$	$56.7 \pm 16.8$	$104 \pm 33.2$	$3.36 \pm 1.35$	$10.8 \pm 4.51$			
2.3	2.4	$240 \pm 51.9$	$90.9 \pm 23.6$	$150 \pm 43.9$	$165 \pm 122$	$166 \pm 102$	$2.11 \pm 1.29$	$6.17 \pm 3.75$			
2.4	2.5	$93.5 \pm 20.9$	$45 \pm 13.1$	$57.7 \pm 16.8$	$9.3 \pm 4.99$	$12.3 \pm 6.38$	$1.82 \pm 1.08$	$9.08 \pm 5.71$			
2.5	2.6	$77.8 \pm 24.3$	$34.7 \pm 14.9$	$45.6 \pm 19.5$	$27 \pm 21.2$	$45.4 \pm 35.5$	$1.17 \pm 0.836$	$5.5 \pm 4.21$			
2.6	2.7	$59.1 \pm 22.5$	$21.3 \pm 9.81$	$57.1 \pm 35.2$	$3.9 \pm 5.53$	$7.02 \pm 9.94$	$0.562 \pm 0.8$	$1.26 \pm 1.55$			
2.7	2.8	$44.9 \pm 19.3$	$21.2 \pm 13.3$	$21.4 \pm 12$	$5.06 \pm 3.6$	$0 \pm 0$	$0.34 \pm 0.486$	$1.79 \pm 2.54$			
2.8	2.9	$13.5 \pm 6.09$	$7.81 \pm 5.09$	$9.14 \pm 5.31$	$0 \pm 0$	$0 \pm 0$	$0 \pm 0$	$0 \pm 0$			
2.9	3	$3.75 \pm 2.15$	$1.53 \pm 1.04$	$2.04 \pm 1.3$	$0 \pm 0$	$0 \pm 0$	$0 \pm 0$	$0 \pm 0$			
3	3.1	$5.24 \pm 2.85$	$3.19 \pm 3.6$	$5.44 \pm 6.11$	$0.518 \pm 0.432$	$1.64 \pm 1.35$	$0 \pm 0$	$0 \pm 0$			
3.1	3.2	$19.3 \pm 20.6$	$1.3 \pm 1.48$	$3.08 \pm 3.46$	$0 \pm 0$	$0 \pm 0$	$0 \pm 0$	$0 \pm 0$			
3.2	3.3	$4.62 \pm 3.89$	$0 \pm 0$	$0 \pm 0$	$0 \pm 0$	$0.769 \pm 0.776$	$0 \pm 0$	$0 \pm 0$			
3.3	3.4	$0.606 \pm 0.745$	$0 \pm 0$	$0 \pm 0$	$0.0444 \pm 0.0678$	$0.503 \pm 0.716$	$0 \pm 0$	$0 \pm 0$			
3.4	3.5	$1.51 \pm 1.86$	$0 \pm 0$	$0.296 \pm 0.374$	$0 \pm 0$	$0 \pm 0$	$0 \pm 0$	$0 \pm 0$			
3.7	3.8	$0.296 \pm 0.423$	$0 \pm 0$	$0 \pm 0$	$0 \pm 0$	$0 \pm 0$	$0 \pm 0$	$0 \pm 0$			

 Table B.2: Numerical results for the cross section for semi-inclusive high- $p_t$  hadron production from 2003 data





# Appendix C

## Asymmetry Additives

### C.1 Asymmetries for the different Periods

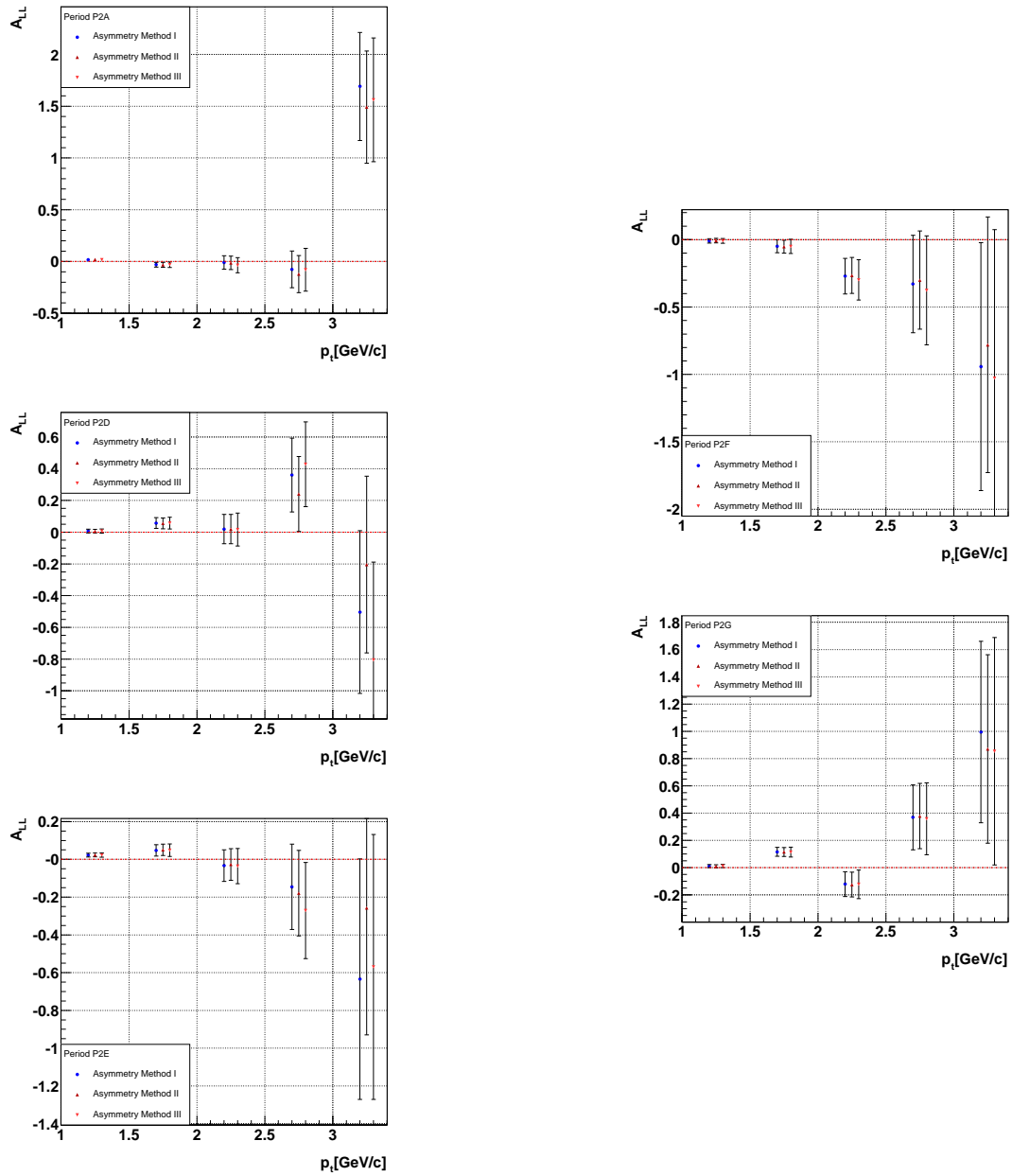


Figure C.1: Weighted means of the asymmetry for all periods of 2002

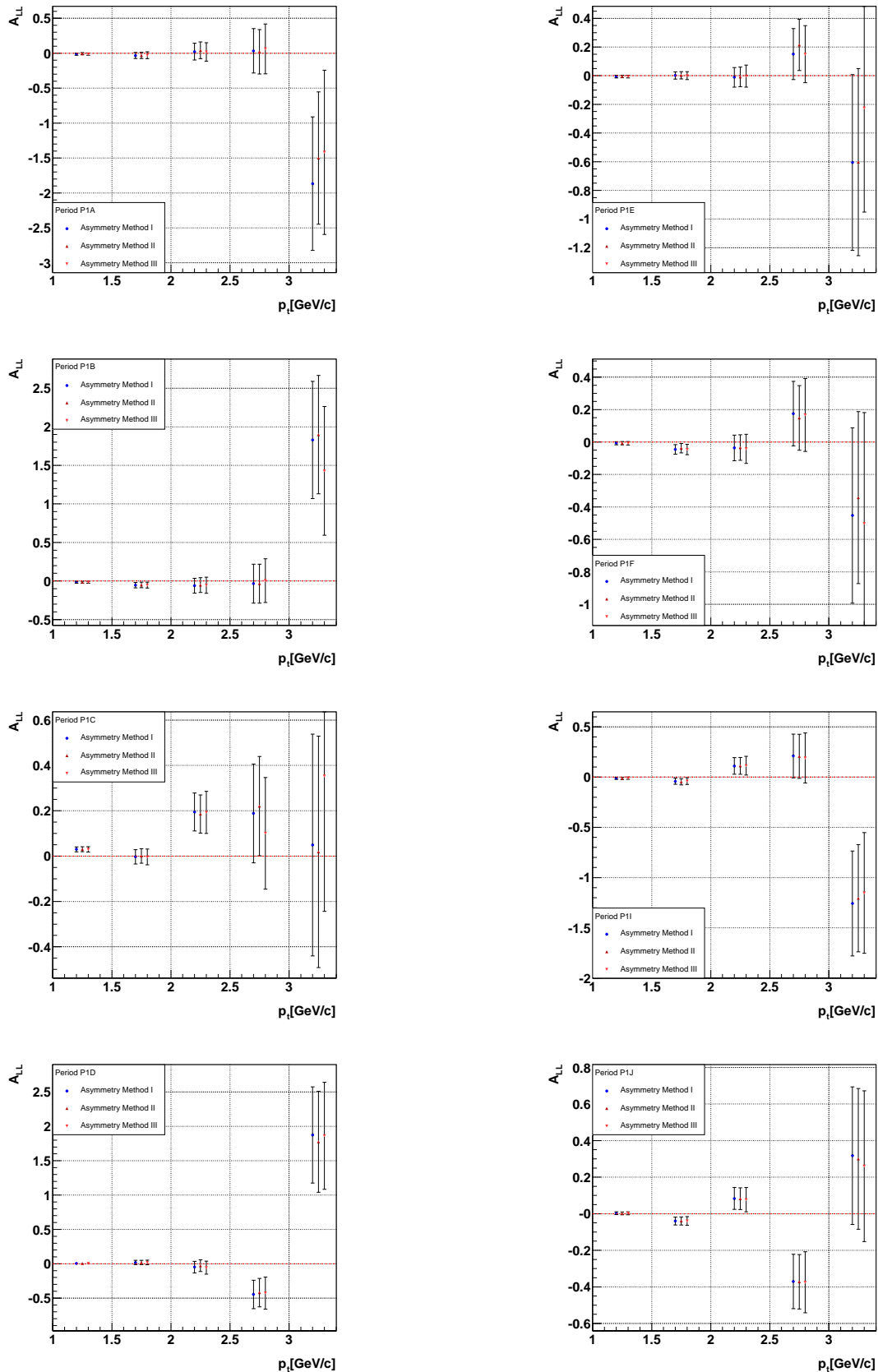


Figure C.2: Weighted means of the asymmetry for all periods of 2003



# Bibliography

- [1] A.V. Manohar, *An Introduction to Spin Dependent Deep Inelastic Scattering*, Lectures at the Lake Louise Winter Institute, February 1992, hep-ph/9204208.
- [2] M. Frhr. von Hodenberg, *A First Reconstruction of COMPASS Data*, Diploma Thesis, Univ. Freiburg, June 2002.
- [3] D. Griffith, *Introduction to Elementary Particles*, Wiley, 1987, New York.
- [4] F. Halzen and A.D. Martin, *Quarks and Leptons*, Wiley, 1984, New York, ISBN 0-471-88741-2.
- [5] The COMPASS Collaboration, *Common Muon and Proton Apparatus for Structure and Spectroscopy*, CERN, **SPSLC 96-14**, March 1996.
- [6] S. Eidelman et al., Phys. Lett. **B592**, 1 (2004).
- [7] R.P. Feynman, *Photon Hadron Interactions* (Benjamin, New York, 1972).
- [8] J.D. Bjorken and E.A. Paschos, Phys. Rev. **185**, 1975(1969).
- [9] T. Pussieux and R. Windmolders, DAPNIA-SPHN-95-10 *Presented at Conf. on Spin Structure of the Nucleon, New Haven, Ct., Jan 6-8, 1994*.
- [10] C. G. . Callan and D. J. Gross, Phys. Rev. Lett. **22** (1969) 156.
- [11] K. Ackerstaff *et al.* [HERMES Collaboration], Phys. Lett. B **464** (1999) 123 [arXiv:hep-ex/9906035].
- [12] E. Albrecht *et al.*, Nucl. Instrum. Meth. A **504** (2003) 354.
- [13] <http://gatignon.home.cern.ch/gatignon/m2commissioning.html>.
- [14] <http://gatignon.home.cern.ch/gatignon/M2manual.html>.
- [15] K. Kondo *et al.*, *Polarization measurement in the COMPASS polarized target*, Nucl. Instr. and Meth. A **526**(2004), 70.

- [16] N. Doshita *et al.*, *Performance of the COMPASS polarized target dilution refrigerator*, Nucl. Instr. and Meth. A **526**(2004), 138.
- [17] K. Gustafsson, COMPASS Note 2003-3, Genf (2003).
- [18] J. Hannappel *et al.*, *The COMPASS Trigger System for Muon Scattering*, December 2004.
- [19] H. Fischer *et al.*, Nucl. Instrum. Meth. A **461** (2001) 507.
- [20] L. Schmitt *et al.*, *The DAQ of the COMPASS Experiment*, IEEE Trans. Nucl. Sci., **51**(2004), 439.
- [21] H. Angerer *et al.*, Nucl. Instrum. Meth. **512** (2003) 229.
- [22] J. Bisplinghoff *et al.*, Nucl. Instrum. Meth. A **490** (2002) 101.
- [23] B. Ketzer *et al.*, Nucl. Instrum. Meth. A **535** (2004) 314.
- [24] C. Bernet *et al.*, Nucl. Instrum. Meth. A **536** (2005) 61.
- [25] D. Dalla Torre, *The COMPASS Spectrometer: Status and Performance*, Workshop on Future Physics @ COMPASS, (2004) 1.
- [26] V. N. Bychkov *et al.*, Part. Nucl. Lett. **111** (2002) 64.
- [27] G. K. Mallot [COMPASS Collaboration], Nucl. Instrum. Meth. A **518** (2004) 121.
- [28] N. Doshita *et al.*, COMPASS Note 2003-5, Genf (2003).  
N. Doshita *et al.*, COMPASS Note 2003-8, Genf (2004).
- [29] T. Sjostrand, L. Lonnblad, S. Mrenna and P. Skands, arXiv:hep-ph/0308153.
- [30] G. Ingelman, A. Edin and J. Rathsman, Comput. Phys. Commun. **101**, 108 (1997).
- [31] W. R. Leo, *Techniques For Nuclear And Particle Physics Experiments: A How To Approach*, Springer, 1992, ISBN 0-387-57280-5.
- [32] COMPASS stability page:  
<http://wwwcompass.cern.ch/compass/software/offline/input/stab/index.html>.
- [33] Bad spills lists:  
<http://wwwcompass.cern.ch/compass/software/offline/input/stab/index.html>.  
[/afs/cern.ch/user/k/korzenev/public/badspill/2002](http://afs.cern.ch/user/k/korzenev/public/badspill/2002).  
[/afs/cern.ch/user/k/korzenev/public/badspill/2003](http://afs.cern.ch/user/k/korzenev/public/badspill/2003).

- [34] M. Arneodo *et al.* [New Muon Collaboration.], Phys. Lett. B **364** (1995) 107.
- [35] S. Trippel, *Aufbau einer Messeinrichtung zur Bestimmung des Myonenflusses bei COMPASS*, Diploma Thesis, Univ. Freiburg, March 2005.
- [36] B. Jäger, *Studies of Hadronic Spin Structure in Hard Scattering Processes at the Next-to-Leading Order of QCD*, PhD thesis, Univ. Regensburg, April 2004.
- [37] P. Schiavon, COMPASS Note 2000-12, Genf (2000).  
P. Schiavon, COMPASS Note 2001-15, Genf (2001).
- [38] J.M Le Goff, COMPASS Note 2004-3, Genf (2004).
- [39] Jörg Pretz, COMPASS Note 2004-11, Genf (2004).
- [40] B. Badelek, <http://pccosrv1.cern.ch/compass/software/offline/input/dilfac/>.
- [41] B. Badelek, COMPASS Note 2004-6, Genf (2004).  
<http://pccosrv1.cern.ch/compass/software/offline/input/F2R/R/>.





# Danksagungen

Für die Unterstützung, die ich beim Verfassen dieser Arbeit erfahren habe, möchte ich mich an dieser Stelle ganz herzlich bedanken.

Bei meinem Betreuer Dr. Horst Fischer und Prof. Kay Königsmann möchte ich mich bedanken, daß sie diese Arbeit und eine aktive Teilnahme am COMPASS Experiment ermöglicht und mich unterstützt haben. Bei Dr. Fritz-Herbert Heinsius, Sonja Hedicke und Martin Freiherr von Hodenberg bedanke ich mich für die Korrektur meiner Arbeit und für viele Diskussionen und Hilfe bei Verständnis- und Computerproblemen. Ebenso möchte ich mich bei Dr. Christian Schill und Johan Matthei für das Korrigieren meiner Arbeit bedanken. Gisela Mössner möchte ich danken für die Hilfe bei allen Verwaltungsfragen und der gesamten Abteilung für ein nettes und entspanntes Arbeitsumfeld. Dominik Setter danke ich für seine Freundschaft während des gesamten Studiums.

Ganz besonderer Dank gebührt meinen Eltern, Thyra und Hartmut Matthiä, und meinen Geschwistern Barbara und Christian, die mich während meines gesamten Studiums unterstützt und ermutigt haben und meiner Freundin Anna Catharina Carstens, die immer für mich da war. Bei allen meinen Freunden möchte ich mich bedanken, daß sie mir geholfen haben den Kopf auch mal frei zu bekommen und an andere Dinge zu denken.



# Erklärung

Diese Arbeit ist von mir selbstständig verfasst worden, und ich habe keine anderen als die angegebenen Quellen und Hilfsmittel verwendet.

Daniel Matthiä, Freiburg, Mai 2005